ALMA MATER STUDIORUM
UNIVERSITÀ DEGLI STUDI DI BOLOGNA

DIPARTIMENTO DI FISICA E ASTRONOMIA
Dottorato di Ricerca in Astrofisica
CICLO XXX

Obscured and Compton-thick AGN in NuSTAR hard X-ray surveys

Candidato:
Alberto MASINI

Supervisore:
Dr. Andrea COMASTRI

Coordinatore:
Prof. Francesco FERRARO

Esame finale anno 2018

Settore Concorsuale 02/C1 – Astronomia, Astrofisica, Fisica della Terra e dei Pianeti
Settore Scientifico-Disciplinare: FIS/05 – Astronomia e Astrofisica

"As soon as man seeks to penetrate the secrets of nature - in which nothing is secret and it is but a question of seeing - he realizes that the simple produces the supernatural."

Honore de Balzac

Abstract

Questa Tesi di dottorato sviluppa un progetto di ricerca selezionato e finanziato da INAF (Istituto Nazionale di Astrofisica) all'interno dell'accordo formale tra INAF e Università di Bologna per il programma di Dottorato in Astrofisica.

Il progetto riguarda survey di nuclei galattici attivi (AGN) nei raggi X duri (fino a qualche decina di keV) con il telescopio NuSTAR. Uno dei principali obbiettivi della missione NuSTAR è quello di studiare con incredibile dettaglio la popolazione di AGN oscurati e molto oscurati (chiamati Compton-thick, CT), che contribuiscono in modo significativo all'emissione diffusa del fondo cosmico a raggi X (CXB), e importanti attori nel ciclo evolutivo delle galassie.

La Tesi si struttura quindi con un approccio locale-distante: nella prima parte, si presenta uno studio di un piccolo campione (circa una dozzina) di AGN locali ($z < 0.03$), molto oscurati, selezionati a causa della loro emissione da megamaser d'acqua a ~ 22.23 GHz. Tale selezione è motivata dalla nota correlazione tra la presenza di emissione da megamaser con geometria a disco, e oscuramento nei raggi X, già nota in letteratura. Grazie alla banda larga di NuSTAR nei raggi X duri (che si estende tra $\sim 3-80$ keV), si ottiene una misura robusta della frazione di sorgenti CT. Partendo da questo risultato e combinando misure nei raggi X e nella banda radio, viene proposto e sviluppato un semplice modello analitico della connessione tra il disco megamaser e il toro; tale modello viene usato per predire la colonna di materiale che assorbe i raggi X dalle mappe radio ottenute con l'interferometro VLBI. Anche se semplicistico, il modello collega in maniera naturale l'emissione da megamaser da disco con l'assorbimento CT in AGN locali.

Un seguito del progetto sui megamaser è legato ad uno studio di variabilità, focalizzato su un ben noto AGN locale oscurato (Mrk1210, noto anche come la Galassia Fenice), e votato allo studio della sua variabilità X a lungo termine (~ 17 anni) usando NuSTAR, grazie al quale si possono ottenere alcune indicazioni sull'ambiente vicino all'AGN basandosi sull'intensità della componente di riflessione presente nello spettro X della sorgente. La discussione viene poi conclusa presentando alcuni esempi su come l'oscuramento CT sia variegato e variabile, e non sempre legato alla presenza di righe del ferro con grande larghezza equivalente. La complessità dell'oscuramento CT complica ulteriormente la ricerca di AGN CT nell'universo più distante, dove si trova il picco dell'accrescimento oscurato cosmico ($1 < z < 2$).

La ricerca e caratterizzazione di AGN CT con NuSTAR viene quindi spinta a redshift maggiori, sfruttando appieno le potenzialità di NuSTAR in termini di sensibilità e risposta nei raggi X duri. La ricerca di AGN oscurati deboli e lontani viene compiuta sfruttando la copertura combinata nei raggi X di NuSTAR, XMM-*Newton* e *Chandra* nel campo UKIDSS-UDS. Si presenta la strategia della survey profonda, insieme alla modellizzazione del background di NuSTAR, per ottimizzare la detezione di sorgenti deboli. Dopo aver accuratamente valutato ogni caso di blending tra sorgenti vicine, la frazione di detezioni spurie, e le controparti ottiche alle sorgenti X rivelate, viene

eseguita un'analisi spettrale X a larga banda di tutto il campione, combinandola con la diagnostica standard da Hardness Ratio (HR), per includere ogni potenziale candidato CT. Questi candidati CT vengono poi ri-analizzati con modelli spettrali appropriati, specificatamente sviluppati per studiare sorgenti CT.
L'ultimo capitolo presenta le conclusioni e le prospettive future del progetto di Tesi.

This Thesis has been devoted to a research project selected and funded by INAF (the Italian National Institute for Astrophysics) within the framework of the formal agreement between INAF and the Bologna University for the PhD program in Astrophysics.

It focuses on NuSTAR hard (up to several tens of keV) X-ray surveys of Active Galactic Nuclei (AGN). One of the major goals of the NuSTAR mission is to study with unprecedented detail the obscured and heavily obscured (Compton-thick, CT) populations of AGN, significantly contributing to the diffuse cosmic X-ray background (CXB), and major actors within the evolutionary cycle of galaxies.

This Thesis is then structured with a local-to-distant approach: in the first part, a survey of a small sample (~ a dozen) of local ($z < 0.03$) heavily obscured AGN, selected by their water megamaser emission at ~ 22.23 GHz, is presented. The selection follows from a known correlation between the megamaser emission with a disk geometry and X-ray obscuration already explored in the literature. Thanks to the NuSTAR hard X-ray spectral coverage (extending between $\sim 3-80$ keV), a robust estimate of the CT fraction is obtained. Building up on this result and combining X-ray and radio measurements, a toy model of the dusty megamaser disk within the classical dusty torus is proposed, and developed in order to predict the X-ray absorbing column density from radio VLBI maps. Despite simplistic, the model connects in a natural way the megamaser emission with the CT absorption in local AGN.

A spin-off of the megamaser project is related to variability, focusing on a well-known local obscured AGN (Mrk1210, a.k.a. the Phoenix Galaxy) and devoted to studying its long-term (~ 17 yrs) X-ray variability with NuSTAR, from which some constraints on the AGN environment can be drawn based on the strength of the reflection component in the X-ray spectrum of the source. The discussion is then concluded presenting few examples on how CT obscuration can be variegate and variable, and not always related to the presence of high equivalent width ($\gtrsim 1$ keV) iron lines. The complexity of CT obscuration challenges the search for CT AGN in the more distant Universe, where the peak of obscured accretion lies ($1 < z < 2$).

The search for, and the characterization of, CT AGN is then pushed to higher redshifts, fully exploiting the NuSTAR X-ray capabilities in terms of sensitivity and hard X-ray response. The hunt for faint and distant heavily obscured AGN is performed exploiting the combined NuSTAR, XMM-*Newton* and *Chandra* coverages of the UKIDSS-UDS field. The deep NuSTAR survey strategy is presented, along with the modeling

of the NuSTAR background in order to optimize the detection of faint sources. Carefully evaluating the blending of sources, spurious fraction, and optical counterparts, a broadband X-ray spectroscopic analysis of all the detected sources is performed, and combined with the standard hardness ratio (HR) diagnostic, in order to select all the possible CT candidates. Such CT candidates are then analyzed again with appropriate X-ray spectral models specifically developed to deal with CT absorbers.
The last Chapter presents the conclusions and future prospects for the project.

Related publications

First author publications

- Masini A., Comastri A., Baloković M., et al. 2016, "NuSTAR observations of water megamaser AGN", *Astronomy&Astrophysics*, 589, 59
- Masini A., Comastri A., Puccetti S., et al. 2017, "The Phoenix galaxy as seen by NuSTAR", *Astronomy&Astrophysics*, 597, 100
- Masini A., Civano F., Comastri A., et al. 2017, "The NuSTAR Extragalactic Surveys: source catalog and the Compton-thick fraction in the UDS field", submitted to *The Astrophysical Journal*

Second author publications

- Brightman M., Masini A., Ballantyne D. R., et al. 2016, "A growth-rate indicator for Compton-thick Active Galactic Nuclei", *The Astrophysical Journal*, 826, 93

Other publications

- Lanzuisi G., Perna M., Comastri A., et al. 2016, "NuSTAR reveals the extreme properties of the super-Eddington accreting supermassive black hole in PG 1247+267", *Astronomy&Astrophysics*, 590, 77
- Koss M., Glidden A., Baloković M., et al. 2016, "NuSTAR Resolves the First Dual AGN above 10 keV in SWIFT J2028.5+2543", *The Astrophysical Journal Letters*, 824, 4
- Boorman P. G., Gandhi P., Alexander D., et al. 2016, "IC 3639 – a new bona fide Compton-thick AGN unveiled by NuSTAR", *The Astrophysical Journal*, 833, 245
- Gandhi P., Annuar A., Lansbury G. B., et al. 2017, "The weak neutral Fe fluorescence line and long-term X-ray evolution of the Compton-thick AGN in NGC 7674", *Monthly Notices of the Royal Astronomical Society*, 467, 4606
- Brightman M., Baloković M., Ballantyne D. R., et al. 2017, "X-ray bolometric corrections for Compton-thick Active Galactic Nuclei", *The Astrophysical Journal*, 844, 10
- Lansbury G. B., Alexander D. M., Aird J., et al. 2017, "The NuSTAR Serendipitous Survey: Hunting for the Most Extreme Obscured AGN at > 10 keV", *The Astrophysical Journal*, 846, 20
- Kosec P., Brightman M., Stern D., et al. 2017, "Investigating the evolution of the dual AGN system ESO 509−IG066", *The Astrophysical Journal*, in press
- Zappacosta L., Comastri A., Civano F., et al. 2017, "The NuSTAR Extragalactic Surveys: X-ray spectroscopic analysis of the bright hard-band selected sample", submitted to *The Astrophysical Journal*

Related activities

Invited talks

- Young Astronomers on Galactic Nuclei 2017 (YAGN17), 23-26 Oct 2017, Teruel, Spain, *"Obscured and Compton-thick AGN in NuSTAR hard X-ray surveys"*

Contributed talks

- The X-ray view of Black Hole activity in the local Universe, 17-19 Feb 2016, Zurich, Switzerland, *"NuSTAR observations of water maser AGN"*
- Demographics and Environment of AGN from Multi-Wavelength Surveys, 21-24 Sep 2015, Chania, Greece, *"NuSTAR observations of water maser AGN"*
- Torus AGN meeting 2015, 14-17 Sep 2015, Winchester, UK, *"The physics of mega-maser AGN"*

Posters

- IAU Symposium 336 Astrophysical masers: unlocking the mysteries of the Universe, 4-8 Sep 2017, Cagliari, Italy, *"Exploring why the detection efficiency of disk megamasers in local Seyfert 2 AGN is so low"*
- NuSTAR meeting 2016, 15-17 Nov 2016, Pasadena CA, USA, *"The Phoenix Galaxy as seen by NuSTAR"*
- AGN: what's in a name?, 27-1 Jun-Jul 2016, Garching, Germany, *"The NuSTAR view of the Phoenix Galaxy and its long-term behavior in the hard X-ray band"*

International Schools, Courses and Conferences attended

- PhD internal course "Everything you always wanted to know about Python but were afraid to ask" in Bologna, Italy, 6-17 Nov 2017
- YAGN17 meeting in Teruel, Spain, 23-26 Oct 2017
- IAU Symposium 336 "Astrophysical masers: unlocking the mysteries of the Universe" in Cagliari, Italy, 4-8 Sep 2017
- PhD internal course "What can we learn from SKA" in Bologna, Italy, Mar 2017
- "AGN: what's in a name?" conference in Garching, Germany, 27-1 Jun-Jul 2016
- PhD internal course "What can we learn from the GAIA mission?" in Bologna, Italy, 6-10 Jun 2016
- "The X-ray view of Black Hole activity in the local Universe" in Zurich, Switzerland, 17-19 Feb 2016

- PhD internal course “The high-redshift Universe and the role of galaxies and AGN to cosmic reionization” in Bologna, Italy, 26-30 Oct 2015
- “Demographics and Environment of AGN from Multi-Wavelength Surveys” in Chania, Greece, 21-24 Sep 2015
- TORUS2015 meeting in Winchester, UK, 14-17 Sep 2015
- “Towards the Cherenkov Telescope Array and Future Gamma–ray Experiments” in Sesto, Italy, 27-31 Jul 2015
- PhD internal course “Bayesian methods in Astrophysics” in Bologna, Italy, 15-17 Apr 2015
- International School of Astrophysics “F. Lucchin” in Teramo (Italy), 9-13 Dec 2014
- PhD internal course “Stellar populations in the local group” in Bologna, Italy, 27-31 Oct 2014

Periods Abroad

- Four months at the Harvard-Smithsonian Astrophysical Observatory in Cambridge MA (USA) within the Marco Polo program, 16-16 Aug-Dec 2016
- Visiting Student for one month at the Harvard-Smithsonian Astrophysical Observatory in Cambridge MA (USA), 30-30 Mar-Apr 2016

Contents

Abstract **v**

Related publications **ix**

Related activities **xi**

1 Introduction **1**
1.1 Preamble 1
1.2 X-ray AGN 3
1.2.1 AGN X-ray spectra 3
1.2.2 The Cosmic X-ray Background 6
1.3 The *Nuclear Spectroscopic Telescope Array* 8

2 Obscured AGN with NuSTAR –
The local Universe **13**
2.1 A discussion on X-ray spectroscopy 13
2.1.1 Phenomenological models for X-ray spectroscopy 14
2.1.2 Toroidal models for X-ray spectroscopy 15
2.2 The NuSTAR survey of bright *Swift*-BAT AGN 18
2.3 Megamasers 18
2.3.1 Disk megamasers 19
2.4 Disk Megamasers and SMBHs demographics 20
2.5 Disk Megamasers and obscured AGN 21
2.6 Data and spectral analysis 23
2.6.1 The sample 23
2.6.2 Data reduction 23
NGC 1194 23
NGC 1386 27
NGC 2273 27
NGC 2960 28
NGC 3079 28
NGC 3393 28

NGC 4388 29
IC 2560 29
2.6.3 Summary of spectral analysis results 30
2.7 The connection between the maser disk and the torus 30
2.7.1 A toy model 33
2.7.2 The torus size 37
2.8 Discussion 39
2.8.1 Comparison with mid-infrared interferometry 39
2.8.2 Trend with bolometric luminosity 39
2.8.3 The possible role of warps 41
2.9 Megamaser disks as probes of AGN accretion 41
2.9.1 The $\Gamma - \lambda_{\rm Edd}$ relation 41
2.9.2 The $k_{\rm Bol}$ of CT AGN 45
2.10 Summary of this Chapter 45

3 Variability and Compton-thickness: the NuSTAR perspective 49
3.1 Variability and "Changing look" AGN 49
3.2 Mrk1210: a case study 50
3.2.1 Data reduction 51
3.2.2 Spectral analysis 51
Phenomenological models 52
Toroidal models 53
A physical picture 54
Intrinsic luminosity 58
3.2.3 Long-term behavior and discussion 58
Change in intrinsic luminosity 60
Eclipsing event 62
3.3 Variability and iron lines in other nearby Seyferts 63
3.3.1 IC3639 63
3.3.2 NGC7674 63
3.4 Summary of this Chapter 64

4 Obscured AGN in deep surveys: the NuSTAR UKIDSS - UDS survey 67
4.1 Hard X-ray surveys with NuSTAR, and the UDS field 67
4.2 Data reduction 70
4.2.1 Flaring episodes 72
4.2.2 Data, exposure, and background mosaics 72
4.3 Simulations 73
4.3.1 Initial setup 74
4.3.2 Reliability, completeness, and sensitivity 74
4.3.3 Catalog creation 79

4.4 Match with XMM-*Newton* and *Chandra* catalogs 80
4.4.1 XMM-*Newton* 80
The case of uds59 82
4.4.2 *Chandra* 83
4.4.3 Optical counterparts 84
4.5 Extraction of X-ray spectra, obscured and CT fraction 86
4.5.1 Combining HR and broadband spectral analysis diagnostic: a refined analysis 89
4.6 Discussion on the CT fraction 91
4.6.1 Iron Kα 97
4.7 Summary of this Chapter 97

5 Conclusions and future perspectives **99**
5.1 Final summary 99
5.2 Future perspectives 100
5.2.1 Megamasers 100
5.2.2 X-ray surveys with current and future missions 100

A Mrk1210: analysis of the 2004 *Chandra* observation **103**
A.1 Analysis of the *Chandra* 2004 (C0) observation 103

B The NuSTAR UKIDSS-UDS survey; further details **105**
B.1 Details of the refined spectral analysis 105
B.1.1 uds47 105
B.1.2 uds48 105
B.1.3 uds63 107
B.1.4 uds66 107
B.2 Catalog description 107

Bibliography **113**

Acknowledgements **127**

List of Figures

1.1 AGN SED 2
1.2 AGN X-ray SED 4
1.3 Effects of $N_{\rm H}$ on AGN X-ray spectrum 5
1.4 CXB 7
1.5 Cartoon of galaxy evolution 8
1.6 NuSTAR sketch 9
1.7 NuSTAR effective area 10
1.8 NuSTAR background 11

2.1 Models for X-ray spectra of AGN; phenomenological model 14
2.2 Toroidal models 15
2.2a MYTorus 15
2.2b BNTorus 15
2.3 Models for X-ray spectra of AGN; the MYTorus model 16
2.4 Models for X-ray spectra of AGN; the MYTorus decoupled model 17
2.5 NGC5765b, maser spectrum 20
2.6 NGC5765b 21
2.6a VLBI map 21
2.6b P-V plane 21
2.7 NuSTAR megamasers spectra 25
2.7a NGC1194: MYT decoupled + `zpow` + `zgauss` 25
2.7b NGC1386: Torus + `zgauss` 25
2.7c NGC2273: Torus 25
2.7d NGC2960: MYTorus 25
2.7e NGC3079: MYTorus + `zpow` 25
2.7f NGC3393: Torus 25
2.7g NGC4388: MYT decoupled + `zpow` 25
2.7h IC2560: Torus + `zgauss` 25
2.8 Torus + Maser disk geometries 32
2.8a Maser disk as torus midplane 32
2.8b Maser disk as torus inner part 32

2.9 The $N_{\rm H}$ distribution as predicted from the toy model 34
2.10 Smooth density profile vs clumpy clouds distribution 36
2.11 Distribution of the parameter $\rho_{\rm out}$ 37
2.12 Distribution of torus outer radius 38
2.13 Circinus torus 40
2.13a MIR interferometric image 40
2.13b Model 40
2.14 Size-luminosity relations 42
2.15 Obscuring warps in disks 43
2.16 $\Gamma - \lambda_{\rm Edd}$ for CT AGN 44
2.17 $k_{\rm bol}$ of CT AGN 46

3.1 SDSS image of Mrk1210 51
3.2 Mrk1210 52
3.2a NuSTAR spectrum 52
3.2b NuSTAR light curve 52
3.3 Mrk1210: baseline model 54
3.3a Fit with the baseline model 54
3.3b Confidence contour plot for the line energy 54
3.4 Toroidal models fits to Mrk1210 spectrum 55
3.4a Fit with the baseline model 55
3.4b Confidence contour plot for the line energy 55
3.5 Decoupled `MYTorus` model fit to Mrk1210 spectrum 56
3.6 Long-term behavior of Mrk1210 59
3.7 Hard and Fe line fluxes 61
3.8 Two local CT AGN. 63
3.8a IC3639 63
3.8b NGC7674 63

4.1 X-ray surveys discovery space 68
4.2 Introduction on NuSTAR surveys 69
4.2a Luminosity - redshift plane 69
4.2b Fraction of resolved CXB intensity. 69
4.3 NuSTAR UDS. 70
4.3a The field in the X-ray band. 70
4.3b Area vs exposure coverage. 70
4.4 Real vs simulation. 73
4.5 Reliability and completeness 76
4.5a Reliability. 76
4.5b Completeness at the 97% reliability threshold. 76
4.6 Sky coverage of the survey. 78
4.7 Aperture photometry on simulations. 79
4.8 UDS99 and UDS97. 80

4.9 Detection on simulations. 81
4.10 Net counts and fluxes of the detected sources in UDS97. 82
4.10a Counts distribution. 82
4.10b Fluxes distribution. 82
4.11 NIR image of uds59 field 83
4.12 Match with XMM-*Newton* and *Chandra* catalogs. 84
4.12a Primary counterpart separation. 84
4.12b NuSTAR vs XMM-*Newton* and *Chandra* fluxes. 84
4.13 Optical counterparts for our sample. 85
4.13a Redshift distribution. 85
4.13b $L_{\rm x} - z$ plane. 85
4.14 UDS97: $N_{\rm H}$ distribution. 87
4.15 UDS97: HR$-z$ plane 88
4.16 Hardness ratio diagnostic 90
4.16a HR$-$Net counts plane. 90
4.16b HR$-N_{\rm H}$ plane 90
4.17 $\nu F\nu$ spectra of the 10 CT candidates in the UDS field 93
4.18 $N_{\rm H}$ for our CT candidates 94
4.19 Measured CT fraction compared with models. 95

A.1 *Chandra* spectrum of Mrk1210 103

B.1 CSTAT as function of $N_{\rm H}$, for uds48 106

List of Tables

2.1 Megamaser sample, global properties, and references. 22
2.2 NuSTAR observation details for the eight sources analyzed. 24
2.3 NuSTAR X-ray best fit spectral results for the eight sources analyzed. . . 26
2.4 $\rho_{\rm out}$ values as computed by the toy model 38
2.5 $R_{\rm X} - L_{\rm bol}$ relations: best fit parameters 41
2.6 Warps depths 43

3.1 History of X-ray observations of Mrk 1210. 50
3.2 Mrk1210: summary of spectral analysis 57
3.3 ASCA and NuSTAR parameters 60

4.1 Details of the individual UDS observations. 71
4.2 Observed vs simulated counts. 74
4.3 Completeness as a function of flux, 97% reliability catalog. 76
4.4 Summary of detection, UDS97 sample. 77
4.5 Detection on simulations and data mosaics. 92
4.6 Summary of properties of the 10 CT candidates. 96

A.1 C0 observation; best fitting parameters. 104

B.1 Results of the refined broadband spectral analysis for the 10 CT candidates. 106
B.2 UDS catalog, I. 111
B.3 UDS catalog, II. 112

Chapter 1

Introduction

This first Chapter is a brief introduction to the main topic of this Thesis, which aims to study obscured Active Galactic Nuclei (AGN), both in the local and more distant Universe, with NuSTAR. A quick review of AGN main properties is presented, focusing mainly on X-ray AGN. In this context, a deeper view of general X-ray AGN spectra and the integrated Cosmic X-ray Background are needed. The Chapter is then concluded presenting the NuSTAR telescope and its early and recent scientific results in the obscured AGN topic.

1.1 Preamble

Active Galactic Nuclei (AGN) represent an exciting and hot topic in modern astrophysics. Since the first optical spectrum of a quasar was obtained in the sixties (Schmidt, 1963), the field has undergone a great expansion and lot of work has been done in order to detect, characterize, and study in detail a wide variety of samples, ranging from single-object case studies to large surveys with almost millions of sources.
The multi-wavelength approach to astronomy has greatly enriched the amount of knowledge in each field. Also AGN, thanks to their unique spectral signature across all the electromagnetic spectrum, can be observed and studied at almost every energy, from radio to γ-rays, as shown in Figure 1.1.
According to the so-called AGN unified model (Antonucci, 1993; Urry and Padovani, 1995), any AGN in the Universe is empowered by an accreting supermassive black hole (SMBH; $M_{\rm BH} \geq 10^6 M_{\odot}$). Accretion phenomena are ubiquitous in the Universe, since accretion disks are predicted (and effectively observed, in most cases) around protoplanets, protostars, white dwarfs, neutron stars, stellar-mass black holes, and SMBHs. As clearly seen in Figure 1.1, different wavelengths probe different parts of the AGN structure. The accretion disk of AGN emits in the optical-UV band, while the X-ray emission is thought to be generated by an hot electron plasma which upscatters the optical-UV photons of the accretion disk in the close vicinity of the central BH (few gravitational radii, where the gravitational radius is defined as $r_g = 2GM_{\rm BH}c^{-2}$), called corona. Part of the energy output of the system is absorbed by matter outside

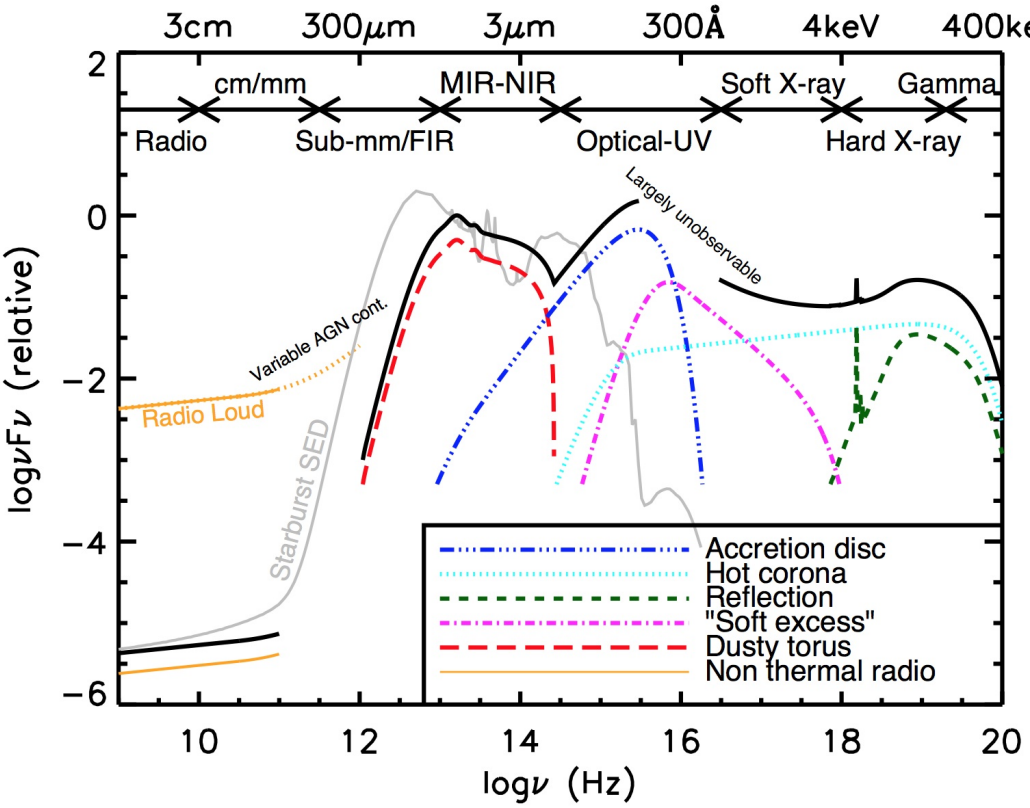

FIGURE 1.1: AGN spectral energy distribution (SED), where the flux emitted by a prototypical AGN is shown as a black solid line. Components invoked to explain the emission in the various energy bands are labeled with different colors and styles. It is clear from the figure that different wavelength regimes probe different parts of the AGN structure and paradigm. Also shown is the template of a starburst galaxy in light gray. Figure adapted from Harrison (2014).

the accretion disk (at the ~ pc scale); if dust is present in the gas, radiation is absorbed and re-emitted in the IR band, and such a structure is called dusty torus. The torus, being axisymmetric, has a crucial role in the simplest version of the unified model of AGN. The line of sight with respect to the torus, and its geometry, are considered to be responsible for the difference between the unobscured and obscured AGN, at least in the local Universe ($z < 1$). When considering large redshift intervals, evolutionary effects become more and more important, challenging the standard version of the unified model, where the geometry of the system is the only parameter. This picture has indeed evolved in recent years, and more parameters are now considered as driving the general evolution of AGN, like the luminosity, the accretion rate, and the timescale associated to the obscured and unobscured phases (Hopkins et al., 2006; Hickox et al., 2014). The radio band, together with the γ-ray band, probes non thermal emission coming from free electrons or jets arising from the central rotating BH. The latter is employed to select and study a particular class of AGN, called blazars, where the highly variable emission is dominated by the jet, pointing directly toward the observer. Blazars and strong radio sources have a different spectral energy distribution (SED),

together with different physical properties, with respect to "normal" (i.e. radio quiet) AGN, and will not be discussed in this Thesis.

1.2 X-ray AGN

Common ways to efficiently detect AGN include radio, mid-infrared (MIR), optical and X-ray selections. Each of them has its strengths and weaknesses (for a recent discussion, see, e.g., Brandt and Alexander, 2015). The X-ray selection method is probably the most efficient one to date, thanks to the penetrating power of X-rays, mainly in the hard X-ray band ($E > 5-10$ keV), which makes them less prone to obscuration biases or contamination from other processes, which afflict, for example, the optical and MIR bands. Moreover, X-ray emission is thought to be a universal feature in the AGN phenomenon, and X-ray luminosities larger than $L_{\rm x} \gtrsim 10^{42}$ erg s^{-1}, which are not explained by other stellar or accretion processes, provide a strong tracer for the presence of an AGN, while the radio band selects preferentially the so-called "radio-loud" (RL) AGN[1]. On the other hand, AGN X-ray selection requires a substantial amount of observing time, due to the difficulty of focusing X-rays (especially hard X-rays) and to the intrinsic faintness of the majority of distant AGN, which can reach fluxes as faint as $F_{\rm x} \sim 10^{-17}$ erg cm^{-2} s^{-1}.

1.2.1 AGN X-ray spectra

The X-ray spectrum of an AGN is composed by a mixture of different components, contributing at different levels depending on geometry, accretion rate, and obscuration. The majority of the X-ray emission can be mainly ascribed to the primary continuum arising from the corona (dashed line in Figure 1.2). The primary continuum has the functional form of a power law, $N(E) \propto E^{-\Gamma}$, with a photon index Γ usually between 1.8 and 2, over almost three decades in energy, between ~0.1 and ~ 400 keV. At low energies (below few keV) the power law suffers absorption from the Galaxy and, for obscured AGN, from the dusty torus, while at high energies (hundreds of keV) the continuum gets exponentially cutoff, due to the limit set by the hot electron plasma temperature. On top of the primary power law, there is also the reflection component (dot-dashed line in Figure 1.2), coming from photons which are reflected (i.e. scattered back, or absorbed and re-emitted) on the accretion disk or the torus inner walls. The characteristic shape of a reflection component includes a bump at $20-30$ keV and an ubiquitous and prominent fluorescent iron Kα line at 6.4 keV, which can be broad or narrow, depending on the location where they both arise. Broad iron lines are usually observed in unobscured AGN, where the line of sight to the accretion disk is free of absorption, the reflection is due to photons emitted from the corona and reflected from the accretion disk, and the broadening of the line is due to special and general relativity

[1] Recently, Padovani (2017) proposed to rename RL and RQ AGN as "jetted" and "non-jetted" AGN, respectively, in order to reflect the presence (or not) of a prominent radio jet dominating the radio emission of the AGN itself.

effects, since the material emitting the fluorescence photons is located very close to the black hole (e.g., Fabian, 2008). On the other hand, in obscured AGN the line of sight to the inner accretion disk is likely to be blocked by intervening matter, and most of the reflection and the line (which is usually narrow) are though to originate on much larger scales (perhaps the inner torus walls, see Gandhi, Hönig, and Kishimoto, 2015, while recent work also suggests a ~ kpc scale origin, at least for the iron line; see Bauer et al., 2015), and the line increasing equivalent width with increasing obscuration is due to the suppression of the underlying continuum. Long term monitoring of sources showing reverberating reflection and iron lines can shed light on the origin of such features (see the case of Mrk1210 presented in Chapter 3). Finally, at even lower energies ($E < 2-3$ keV), the spectrum of an unobscured AGN shows the so-called "soft excess" (dotted line in Figure 1.2), for which several interpretations have been given, despite a definitive answer is still missing (could be due to reflection of ionized gas; e.g., Fabian et al., 2012). The arising soft emission in obscured AGN, on the other hand, is thought to be due to electron scattering in an ionized zone extended on a size scale larger than the obscuring structure (Bianchi and Guainazzi, 2007), and is well modeled by a power law resembling the primary one (i.e., with roughly the same Γ), rescaled by a factor of a few percent.

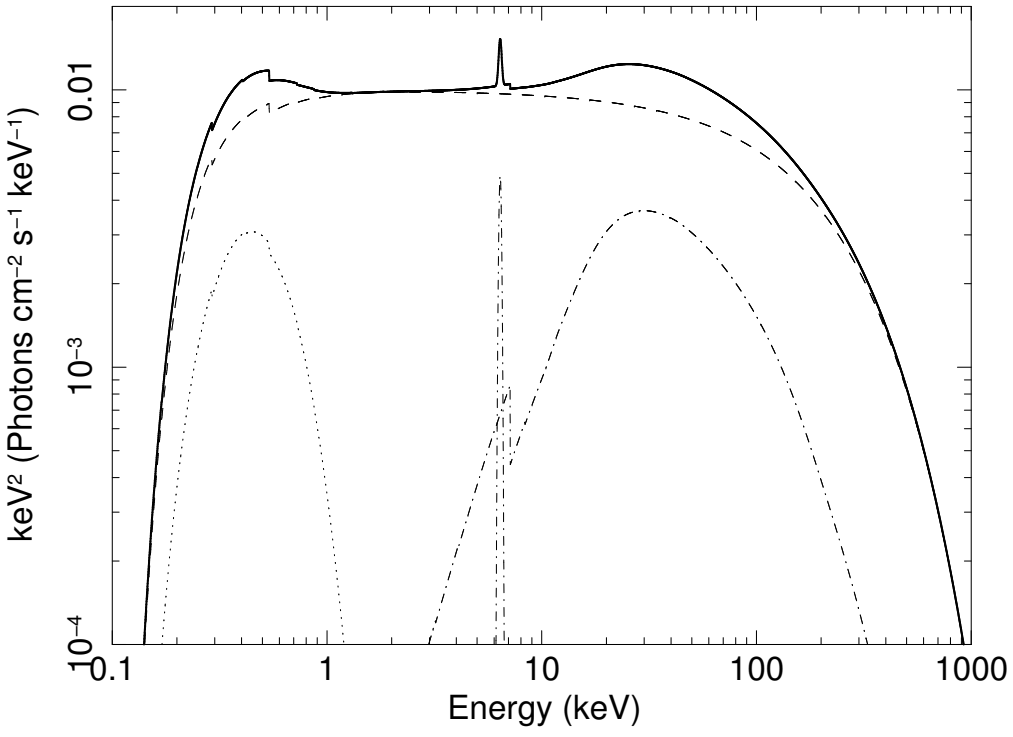

FIGURE 1.2: Zoom-in on the typical unobscured AGN X-ray (100 eV – 1 MeV) SED, where the primary power law is labeled as the dashed line, the reflection and iron fluorescence line are labeled with dot-dashed lines, and the so-called "soft excess" is modeled as a black body and indicated by the dotted line. The spectrum is absorbed by a typical Galactic column density of $N_{\rm H}^{\rm Gal} = 2 \times 10^{20}$ cm^{-2}.

X-ray spectroscopy is a powerful tool to study in detail the X-ray emission from an AGN. It provides fundamental parameters, like the photon index of the primary power law or the high-energy cutoff, which are in turn related to the physics or physical properties of the hot electrons of the corona and its optical depth, the obscuring status of the source and its column density along the line of sight, lines equivalent width, X-ray fluxes and luminosities. In particular, the de-absorbed (i.e., corrected for absorption) X-ray luminosity can be used to get an estimate of the total (i.e., bolometric) luminosity, applying a proper bolometric correction factor $k_{\rm Bol}$, such that $L_{\rm bol} = k_{\rm bol} L_{\rm X}$. On the other hand, an estimate of the SMBH mass allows to calculate the Eddington luminosity $L_{\rm Edd}$, which is defined as the maximal luminosity which an accreting system can have. Beyond this limit, the radiation pressure overbalances gravity and the accreting material is expelled from the system. The ratio between the bolometric luminosity and the Eddington luminosity is defined as the Eddington ratio, $\lambda_{\rm Edd}$, and is a probe of the accretion rate onto a black hole, and is then defined as $\lambda_{\rm Edd} = L_{\rm bol}/L_{\rm Edd} \propto k_{\rm bol} L_{\rm X}/M_{\rm BH}$.

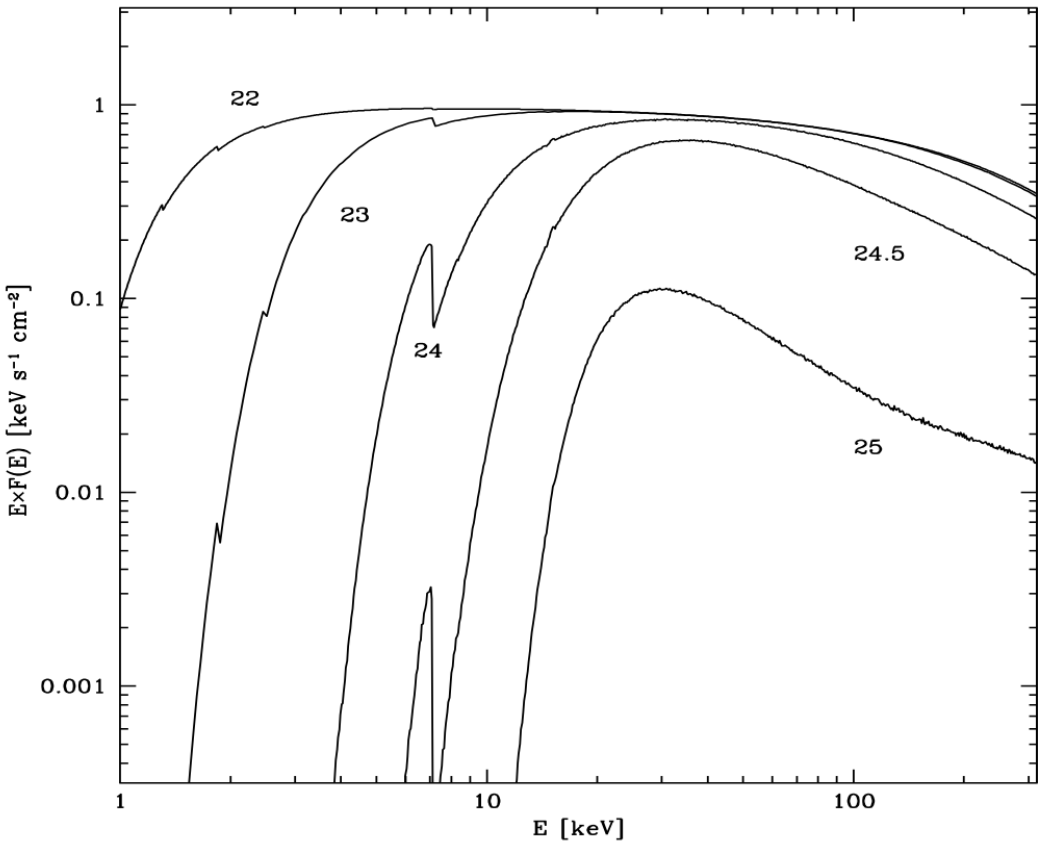

FIGURE 1.3: Effects of different $N_{\rm H}$ on AGN X-ray spectrum with $\Gamma = 2$, affected by photoelectric absorption and Compton downscattering at the highest $N_{\rm H}$. The numbers label the logarithm of the column density expressed in cm^{-2}. Figure adapted from Comastri (2004).

1.2.2 The Cosmic X-ray Background

In analogy with the more famous and intense Cosmic Microwave Background (CMB, Penzias and Wilson, 1965), the discovery of the existence of a Cosmic X-ray Background in the early sixties (CXB, Giacconi et al., 1962) greatly boosted the research on the nature of this diffuse emission, which was immediately recognized as extragalactic in origin. As of today, most of the CXB intensity has been resolved into discrete sources, although for $E < 10$ keV (Worsley et al., 2005; Hickox and Markevitch, 2006; Xue et al., 2011), thanks to the large number of surveys performed by important facilities like *Chandra* (Weisskopf et al., 2000) and XMM-*Newton* (Jansen et al., 2001). Both these instruments brilliantly surveyed the X-ray sky for almost twenty years now, but they are limited mostly to soft X-ray energies ($E < 10$ keV) and suffer a substantial absorption bias. It is well known, indeed, that if an X-ray source is obscured by a certain amount of gas $N_{\rm H}$ along the line of sight to the observer, expressed in cm^{-2}, the X-ray flux can be significantly attenuated, and only a fraction of the intrinsic flux of photons reach the observer, while most of them get scattered or photo-absorbed. The optical depth τ of the intervening gas can be expressed as $\tau = N_{\rm H}\ \sigma_{\rm T}$, where σ_T is the Thomson scattering cross-section. When the optical depth becomes comparable to, or larger than one, the gas becomes Compton-thick (CT), and the corresponding column density is $N_{\rm H} \gtrsim \sigma_{\rm T}^{-1} = 1.5 \times 10^{24}$ cm^{-2}. Above the CT threshold, also the high-energy emission (> 10 keV) is suppressed by downscattering. An example of how the typical X-ray spectrum of an AGN is modified by an intervening column density is shown in Figure 1.3. In principle, the intrinsic emission from the AGN is totally suppressed below $E < 4$ keV by a CT column density. However, Figure 1.3 shows only the primary continuum suppression and no reflection nor the scattered power law are included.
Considering a mixture of populations of AGN with a distribution in redshift, luminosity, and obscuration, one can build a model of the CXB, which represents the integrated emission from AGN at all redshifts, luminosities, and obscuration (Comastri et al., 1995), and fit it to the data.
As shown in Figure 1.4, obscured AGN (i.e., $10^{22} < N_{\rm H} < 10^{24}$ cm^{-2}; also called Compton-thin) account for most of the CXB emission above 2 keV (long dashed component in Figure 1.4), while unobscured AGN (i.e., $N_{\rm H} < 10^{22}$ cm^{-2}) dominate below 2 keV (short dashed component in Figure 1.4). Finally, a population of heavily obscured sources is accounted for, to fit the measured peak of the X-ray background between 20 and 30 keV (e.g. Gilli, Comastri, and Hasinger, 2007), and is labeled as the dot-dashed line. Although not being dominant, such contribution is significant. Assuming indeed that the peak of the CXB could be modeled by Compton-thin AGN only , the relative fraction of obscured sources would significantly overestimate the observed one. The fraction of CT AGN is then a key ingredient of population synthesis models, and while some models assume a relatively high intrinsic fraction of CT AGN (e.g., ~ 40% of all AGN; Gilli, Comastri, and Hasinger, 2007), others adopt different recipes with a much lower fraction of CT AGN in order to fit the observed CXB spectrum, adding other physical

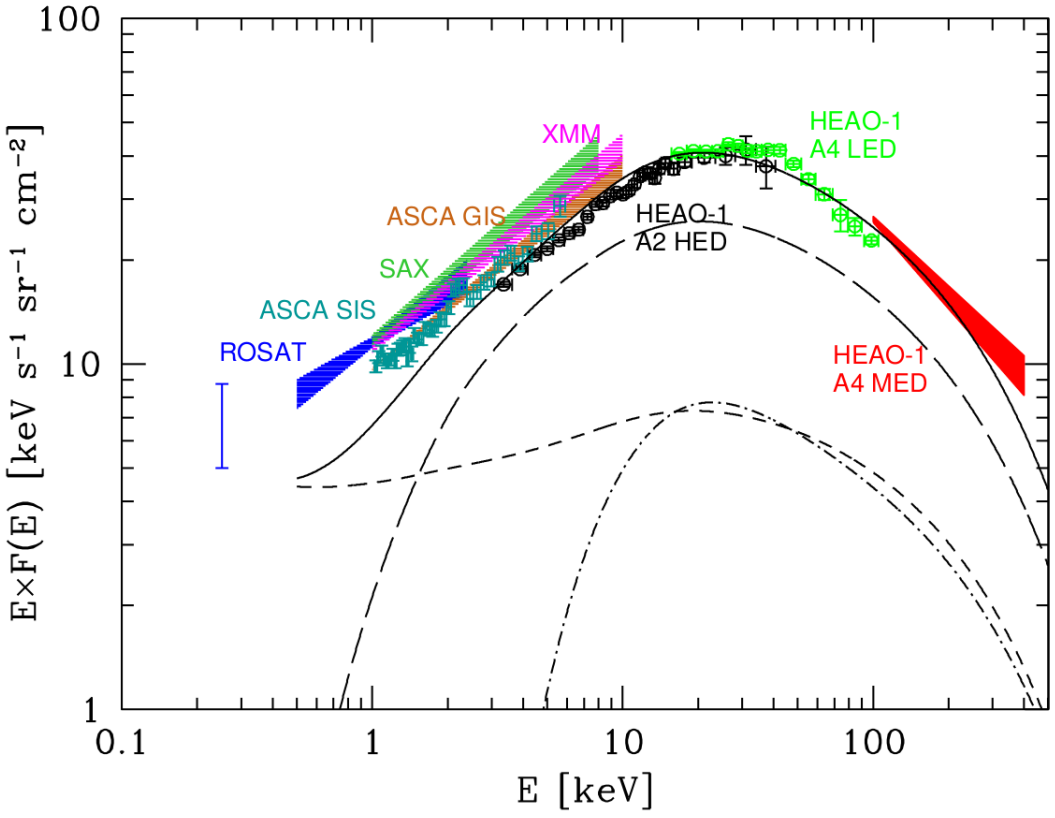

FIGURE 1.4: CXB spectrum between 0.1 – 400 keV, measured by various instruments. The best-fitting model of Comastri et al. (1995) is labeled as the black solid line, while contributions from unobscured ($N_{\rm H}$ < 10^{22} cm^{-2}), Compton-thin (10^{22} < $N_{\rm H}$ < 10^{24} cm^{-2}) and Compton-thick ($N_{\rm H}$ > 10^{24} cm^{-2}) AGN are labeled as the short-dashed, long-dashed and dot-dashed lines, respectively. Figure adapted from Comastri (2004).

parameters such as the strength of the reflection component or the spin of SMBHs, based on observations of statistically significant samples (Treister, Urry, and Virani, 2009; Akylas et al., 2012; Akylas et al., 2016; Vasudevan et al., 2016).

Regardless of their exact fraction, CT AGN are also often considered as a crucial evolutionary phase by many galaxy evolution models, mainly related to merging episodes (see Figure 1.5), in which a large fraction of cold gas is funneled toward the central SMBH, which actively grows and subsequently influences the host galaxy (Sanders et al., 1988; Hopkins et al., 2006; Ricci et al., 2017). This co-evolution of the SMBH with its host galaxy gives then rise to the well-known BH-host scaling relations, such as the $M_{\rm BH} - M_{\rm bulge}$, or the $M_{\rm BH} - \sigma_*$ (Magorrian et al., 1998; Ferrarese and Merritt, 2000). Therefore, active SMBHs hidden by CT obscuration need to be taken into account by theoretical models, both population synthesis and galaxy evolution, but represent also an observing challenge. Indeed, there are indications that many of the AGN closest to our Milky Way are significantly absorbed (Arévalo et al., 2014; Puccetti et al., 2014; Bauer et al., 2015; Annuar et al., 2017) and CT absorption is commonly observed in

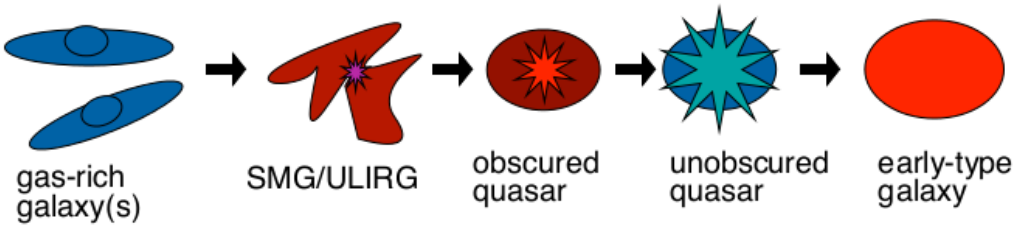

FIGURE 1.5: Cartoon of the merger-driven galaxy evolution model. Mergers are expected to funnel a large amount of cold gas towards the central SMBHs, which eventually merge and actively grow buried in a dense shell of cold gas. The feedback from the obscured (and possibly CT) quasar then expels the surrounding gas, making the AGN shine as unobscured and impacting (positively or negatively) the host galaxy star formation. Figure adapted from Alexander and Hickox (2012).

the local Universe (e.g., Maiolino et al., 1998; Risaliti, Maiolino, and Salvati, 1999). Nonetheless, great efforts have to be done in order to robustly detect these sources in the distant Universe (i.e., at redshift $z > 1$, e.g. Gilli et al., 2011; Lanzuisi et al., 2015). Despite the enormous successes of *Chandra* and XMM-*Newton*, the large majority of the CXB above 10 keV remains unresolved. This is due to the technological difficulty of focusing hard X-rays, and till few years ago, only coded mask instruments, such as *Swift*-BAT and INTEGRAL, were employed to survey the hard X-ray sky. Deep surveys with these instruments were able to resolve up to few percent ($1-2\%$) of the total CXB above 10 keV (Churazov et al., 2007; Krivonos et al., 2007; Ajello et al., 2008; Burlon et al., 2011; Vasudevan, Mushotzky, and Gandhi, 2013; Ricci et al., 2015; Akylas et al., 2016; Koss et al., 2016), but the picture changed with the advent of the *Nuclear Spectroscopic Telescope Array* (NuSTAR).

1.3 The *Nuclear Spectroscopic Telescope Array*

NuSTAR, launched in 2012 (Harrison et al., 2013), is the first focusing hard X-ray telescope, and as such represented a quantum leap forward in hard X-ray astronomy. It operates between 3 and 78 keV, and is equipped with an array of eight CdZnTe detectors separated in two focal plane modules (FPMA and FPMB, respectively). A sketch of the NuSTAR instrument is presented in Figure 1.6.

Thanks to its innovative focusing optics, NuSTAR gained a factor of ~ 100 in sensitivity with respect to coded-mask instruments. As of today, NuSTAR is the only instrument to extend the focusing capabilities beyond 10 keV (see Figure 1.7). With a point spread function (PSF) of half-power diameter (HPD) of $58''$, and a full width at half maximum (FWHM) of $18''$, imaging in the hard X-ray band with a reasonable spatial accuracy has become possible. The drawback of such novel technology has been a rather high background affecting deep observations, since the NuSTAR metallic mast, when fully deployed in orbit, prevents the optics to be perfectly screened by leaking photons.

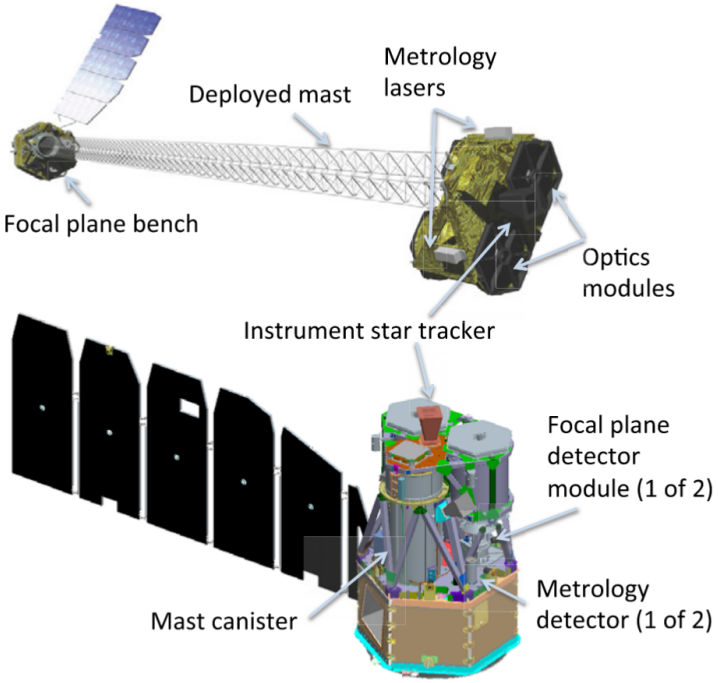

FIGURE 1.6: Sketch of the NuSTAR instrument. The top figure shows the final configuration of the telescope, with the metallic mast extended once it reached its orbit. The bottom figure shows a zoom of the focal plane, where the couple of four-chips CdZnTe detectors lies. Figure adapted from Harrison et al. (2013).

In particular, as explained in Wik et al. (2014) and as shown in Figure 1.8, the NuSTAR background is the sum of different components: below 20 keV, its signal is dominated by photons which are not focused by the mirrors and leak through the open structure of the telescope producing a spatially-dependent pattern (i.e., aperture background). There are also solar photons, a neutron background, and a minor contribution from the focused, but unresolved, sources of the CXB (i.e., fCXB). Above ~ 20 keV, the background is instrumental, and is composed of a nearly flat power law ($\Gamma \approx 0$) with a forest of activation lines, most notably between $\sim 25 - 35$ keV.

One of the primary scientific goals of the NuSTAR mission is to study both local and distant AGN, mainly looking for CT AGN with the aim of directly detecting the contributors to the CXB peak at $\sim 20 - 30$ keV. NuSTAR is the optimal instrument to tackle these tasks, thanks to its high-energy bandpass which makes it less biased to absorption with respect to low energy instruments. To reach this key science goal, a series of Extragalactic surveys have been undertaken, both in the local ($z < 0.5$) and distant ($z \gtrsim 1$) Universe. In the local Universe, together with some pilot studies on nearby and well-known CT AGN, such as Circinus (Arévalo et al., 2014), NGC1068 (Bauer et al., 2015) and NGC4945 (Puccetti et al., 2014), a survey of ~ 100 bright AGN detected by *Swift*-BAT was conducted (see Baloković et al., 2014, for some early results; Baloković et al., in prep). In particular, a subsample of these bright, local AGN is composed by water megamasers, on which we are going to focus in the next Chapter. NuSTAR is

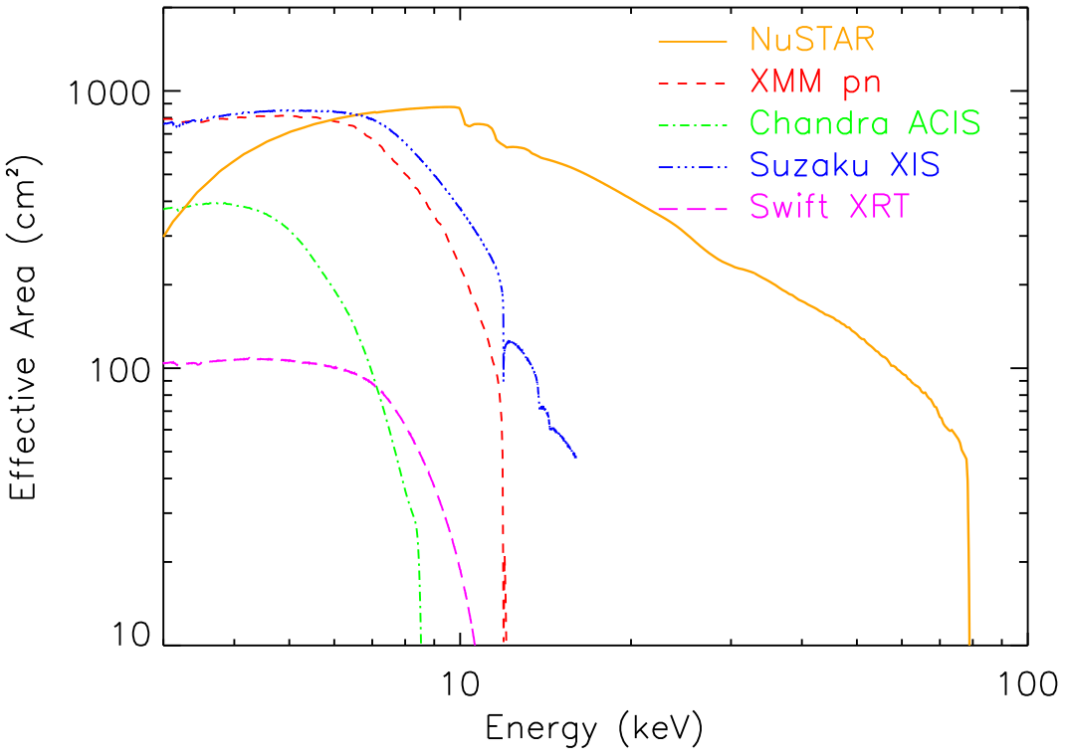

FIGURE 1.7: NuSTAR effective area as a function of energy (orange line), compared with other focusing optics. NuSTAR overlaps with XMM-*Newton*, *Chandra*, *Suzaku* and *Swift*-XRT in the soft X-ray energy band, extending the focusing capabilities beyond 10 keV. Figure adapted from Harrison et al. (2013).

now beginning a new survey in the local Universe, called NuLANDS, with the aim of obtaining an unbiased view of the local absorption distribution of AGN (Boorman et al., in prep).

As of the deep Extragalactic surveys, a wedding-cake approach has been adopted, from a wide area, shallow survey of the COSMOS field (Civano et al., 2015), up to a deep survey of the ECDFS field (Mullaney et al., 2015). An important role is also played by the Serendipitous survey (Alexander et al., 2013; Lansbury et al., 2017b), which recently released its 40-month Catalog (Lansbury et al., 2017b). Other surveys of well-known, multi-wavelength deep fields include the EGS (Aird et al., in prep), CDFN (Del Moro et al., in prep), and UKIDSS-UDS (Masini et al., submitted) surveys.

To date, the surveys undertaken by NuSTAR both in the local and distant Universe provided, among others, important results in the understanding of the physics of obscured AGN. For example, detailed spectral analysis of the high signal-to-noise ratio (SNR) spectra of nearby CT AGN revealed the complexity of the absorbing medium, which is often described as a sum of different absorbing layers (Bauer et al., 2015), or with spatially decoupled reflection and transmission components (Arévalo et al., 2014). Moreover, the detection for the first time of hard X-ray variability, likely due to the intrinsic continuum piercing through the patchy torus, gave a remarkable evidence for

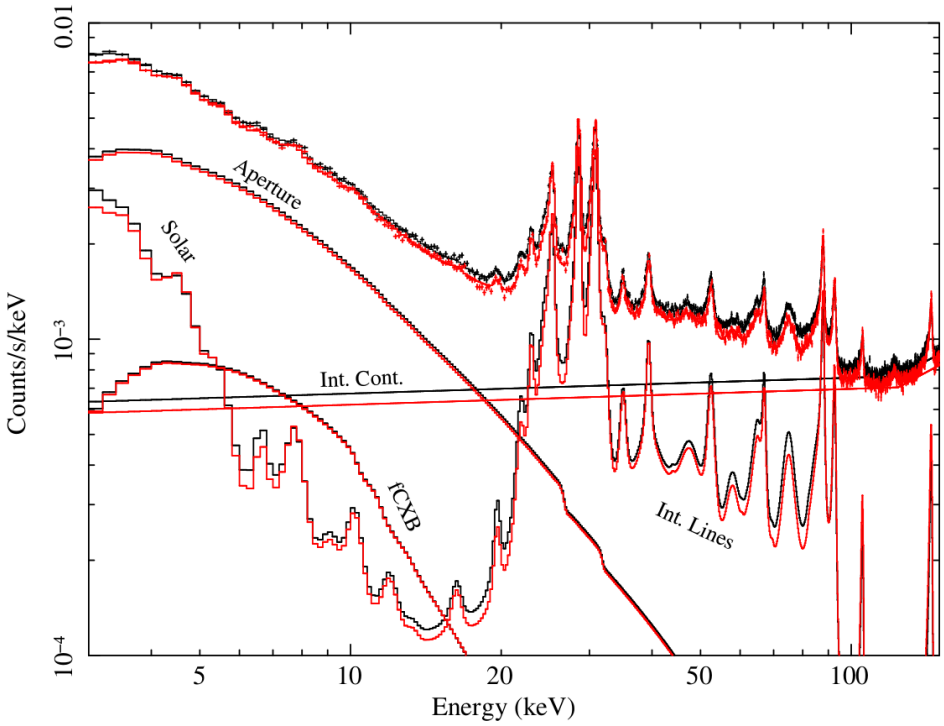

FIGURE 1.8: The NuSTAR background (black for FPMA, red for FPMB) is made up of different contributions, arising from solar, aperture, focused but unresolved CXB, and instrumental components. Figure adapted from Wik et al. (2014).

the clumpiness of the obscuring structure around AGN (Puccetti et al., 2014; Marinucci et al., 2016). On the other hand, the NuSTAR deep extragalactic surveys have so far resolved the ~ 35% of the CXB in the NuSTAR hard (8 – 24 keV) band (Harrison et al., 2016), and allowed the first direct measurement of the > 10 keV X-ray luminosity function (LF) to be measured at $z > 0.1$ (Aird et al., 2015), together with providing a less biased view on the distant AGN population as a whole.

In the next Chapters, we are going to discuss in greater detail the NuSTAR contribution in the search and study of CT AGN, going from the local to the distant Universe.

Chapter 2

Obscured AGN with NuSTAR – The local Universe

In this Chapter, the NuSTAR view of obscured and Compton-thick AGN in the local Universe is presented. Such objects are an important laboratory and test ground for AGN physics, in order to understand the properties and signature of heavy obscuration around SMBHs.
After a general introduction on X-ray spectroscopy, which is the main tool used to perform data analysis throughout this Thesis, the discussion will focus on megamasers, which are a optimal sample of local, heavily obscured AGN. The majority of disk megamasers come with an exquisite measurement of their BH mass, and thanks to radio interferometric observations, allow to study the physics of the obscuring medium at the sub-pc scale. After compiling a sample with both high-quality radio and NuSTAR data, results of X-ray spectroscopy of the entire sample are presented, and an analytical toy model to explain the link between sub-pc scale megamaser disks and pc-scale obscuring tori is developed. In the last part of the Chapter, a few applications of the results obtained on megamasers to the physics of AGN are presented. This Chapter is mainly based on: *"NuSTAR observations of water megamaser AGN"*; Masini, A., Comastri, A., Baloković, M., Zaw, I., et al.; 2016; A&A; 589, A59.

2.1 A discussion on X-ray spectroscopy

Throughout this Thesis, the spectral analysis is always carried out using the XSPEC software (Arnaud, 1996), which allows visualization, modeling and fitting of X-ray spectra. The usual procedure is to start fitting the spectra with simple power law models for an initial visual inspection of the broadband spectral curvature and X-ray absorption. One then builds up more complex models, motivated by the presence of typical features such as the Compton hump, the iron line(s), the high-energy cutoff, the soft excess, and so on (see Section 1.2.1 for a discussion on the principal components contributing to the X-ray emission from an AGN).

2.1.1 Phenomenological models for X-ray spectroscopy

Many models have been developed in the past years to explain and fit the X-ray spectra of AGN, regardless the level of obscuration. One of the advantages of these models is that they are relatively fast and easy to implement. Moreover, they are employed to make comparison with previous result in the literature. Some of the most commonly used phenomenological models when dealing with Seyfert 2 AGN (i.e., obscured AGN) include `plcabs` (Yaqoob, 1997) and `pexrav` (Magdziarz and Zdziarski, 1995), to model the hard X-ray continua. The former describes X-ray transmission of an intrinsic power law with an exponential cutoff through an obscuring medium, taking the effects of Compton scattering into account. However, it is limited to $\sim 15-20$ keV depending on the exact value of the column density. The latter models Compton reflection on a slab of neutral material with infinite optical depth, and provides a good approximation for the reflection from the accretion disk.

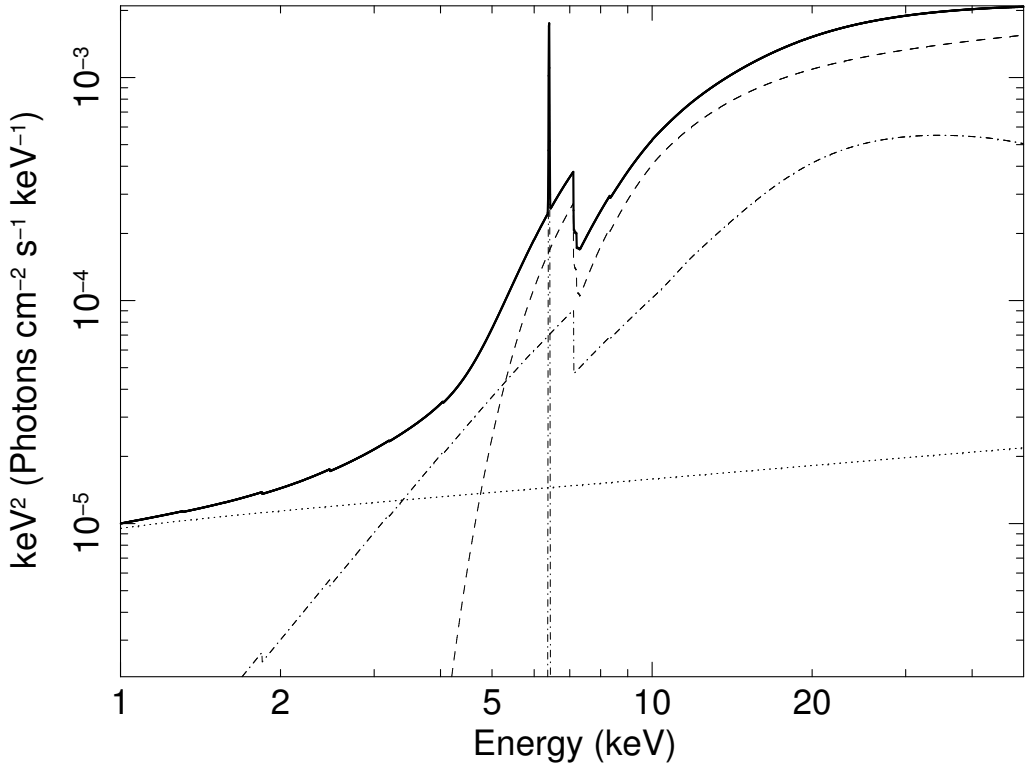

FIGURE 2.1: Example of a phenomenological model for a typical Compton-thick spectrum ($N_{\rm H} = 10^{24}$ cm^{-2}) between 1−50 keV. The photon index is $\Gamma = 1.8$ and the fraction of scattered power law is 1%. The transmitted primary power law (`plcabs`), the reflection/fluorescence components (`pexrav` and `zgauss`), and the scattered power law are labeled as the dashed, dot-dashed and dotted lines, respectively. The total spectrum is the solid black line. Note that the normalizations are quite arbitrary, since the models are independent. We adopted here a normalization for the reflection component a factor of two lower than the transmitted one, i.e. a reflection parameter $R = 0.5$.

A proper combination of these models (see Figure 2.1) often provides excellent fits

to obscured AGN spectra; however, one should always check that the *ad-hoc* combination of such models does not violate any basic physical principle (like the energy conservation law, for example, having more reflected emission of the primary one). Moreover, as pointed out by Murphy and Yaqoob (2009), using `plcabs` and `pexrav` may produce a bias toward fits dominated by the direct continuum. Results obtained with such phenomenological models need to be tested against more self-consistent and physically motivated models.

2.1.2 Toroidal models for X-ray spectroscopy

A bunch of such physically motivated models, based on Monte Carlo simulations, have been developed in the last decade, but only a couple of them are publicly available to date, like `MYTorus` (Murphy and Yaqoob, 2009) and `Torus` (Brightman and Nandra, 2011). Despite having slightly different geometries (sketches of the two models are shown in Figure 2.2), free parameters and implementations, they both model the hard X-ray spectrum emitted through a toroidal reprocessor, consisting of a transmitted continuum (photons passing through the torus without interacting), a scattered or reflected component that is made up of photons that interact with matter via Compton scattering, and emission lines (mostly iron Kα and Kβ).

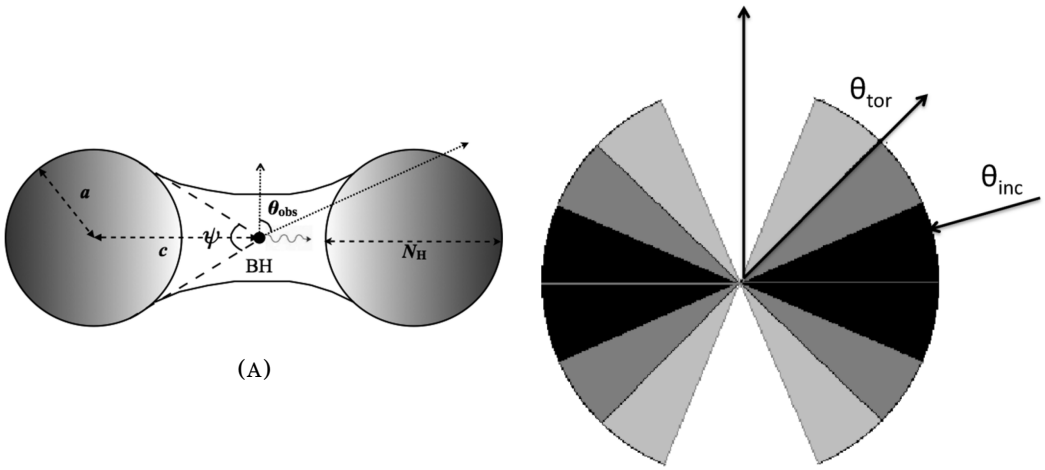

FIGURE 2.2: **(A).** Sketch of the `MYTorus` model, with the most important parameters labeled. The geometry is fixed, with an half-opening angle of 60°, equivalent to $c/a = 2$. Notice that the line of sight $N_{\rm H}$ is different from the equatorial $N_{\rm H}$, unless $\theta_{\rm obs} = 90°$. Figure adapted from Murphy and Yaqoob (2009). **(B).** Sketch of the `Torus` model, where the absorbing medium is arranged as a sphere without two polar bicones. Two angles are then defined, which are labeled in the figure as $\theta_{\rm tor}$ (i.e., the half-opening angle of the torus) and $\theta_{\rm obs}$ (i.e., the inclination of the system with respect to an external observer). The different shadings do not indicate different density, which is assumed uniform instead. Figure adapted from Brightman and Nandra (2011).

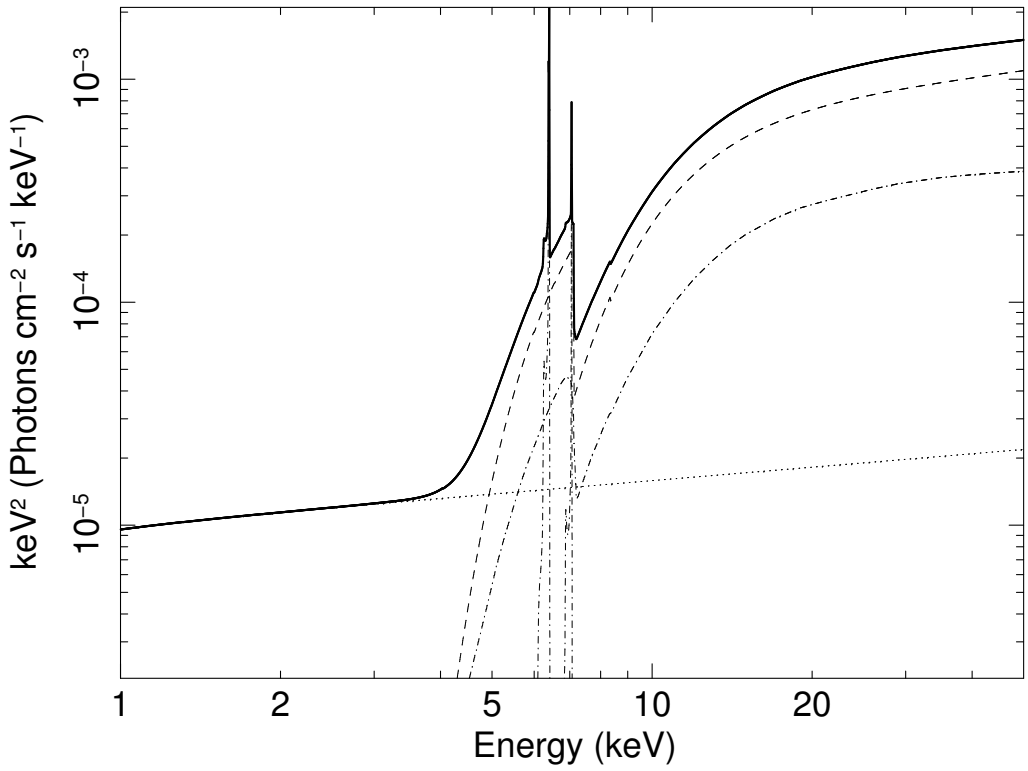

FIGURE 2.3: Same parameters and conventions of Figure 2.1, but adopting a default MYTorus model with $\theta_{obs} = 90°$. Only one normalization is needed here, because all the components are self-consistently computed.

`MYTorus` allows a dynamic decoupling of these three components to simulate different geometries. It can be used in its default configuration ("`MYTorus` coupled", Figure 2.2a), modeling a classical "donut-shaped" toroidal reprocessor with a fixed covering factor of 0.5 (i.e., the half-opening angle θ_{tor} of the torus is 60°, measured as the angle between the axis of the system and the edge of the torus itself; see Figure 2.3 for an example), or in a more complex way, called "`MYTorus` decoupled".

The total X-ray emission reaching a distant observer suffers of attenuation (photoelectric absorption and scattering) by the intervening screen of matter, proportional to $e^{-\tau}$, where τ is the optical depth of the absorbing medium. However, also photons which would not reach the observer are randomly scattered inside the line of sight by the same processes, contributing to the total emission. In addition to this transmitted and scattered radiation through the obscuring medium, part of the reflection from the inner far side of the reprocessor may not intercept the material on the near side of it. In this case, the far-side reflection, at least below $\sim$ 10 keV, can dominate the observed spectrum. This physical situation is parameterized decoupling the inclination angles of the transmitted and scattered components of the `MYTorus` model, as sketched in Figure 2.4. Even if the attenuation and scattering into the line of sight share the same physical process, they are distinct in the `MYTorus` model, and result in two different spectral shapes. The forward-scattered emission and associated emission lines

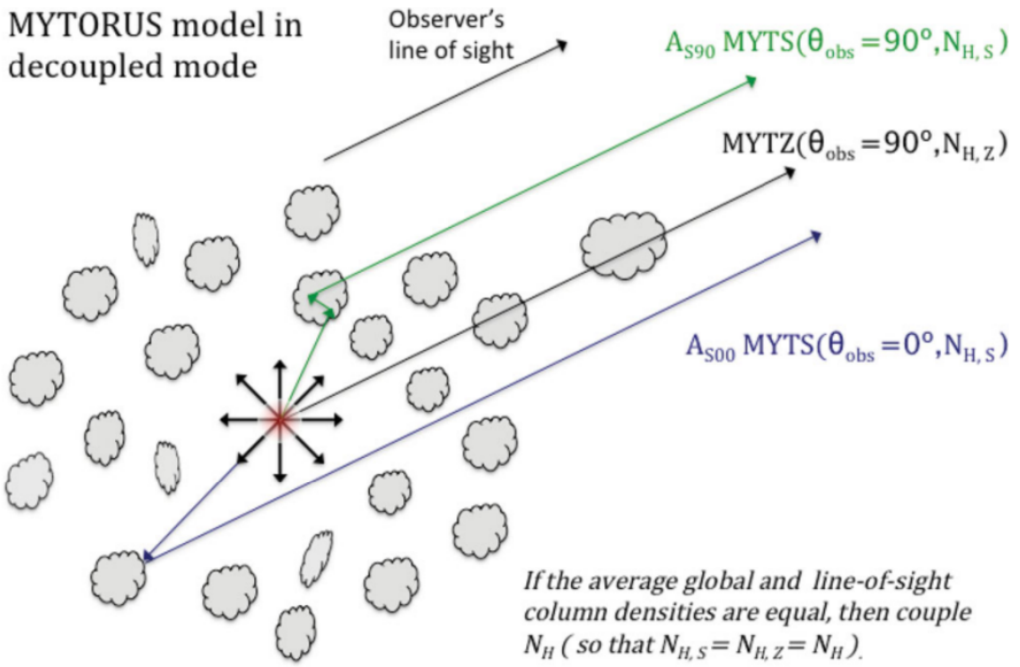

FIGURE 2.4: Sketch of how a particular physical situation (e.g. a patchy and clumpy torus) can be modeled with a decoupled `MYTorus` model. Figure adapted from Yaqoob (2012).

are approximated using a `MYTorus` edge-on reflection spectrum, obtained by fixing $\theta_{\rm obs}$ to 90° (green line in Figure 2.4), while the `MYTorus` face-on reflection spectrum is modeled by fixing the inclination angle of the system $\theta_{\rm obs}$ to 0° (blue line in Figure 2.4). The relative strength of these two components (front and back-scattered) is encoded in two constants, namely A_{S90} and A_{S00}, which are left free to vary. Their respective line components for this geometry are normalized with A_{L90} and A_{L00}. In the most general case, the column density $N_{\rm H}$ obscuring the direct continuum can be decoupled from the column density responsible for the back reflection or the forward reflection or both. A single $N_{\rm H}$ value is often adopted for the sake of simplicity, but see Yaqoob (2012) for an exhaustive example of the use of the model in its decoupled mode. This decoupled configuration allows to simulate different geometries and covering factors with respect to the default one of `MYTorus`, although it is difficult to compute the covering factor of any specific situation.

On the other hand, the `Torus` model does not decouple the three components, but has the opening angle (allowing the measurement of the covering factor; e.g., Brightman et al., 2015) and the iron abundance as free parameters. In the following, we always assume a nearly edge-on inclination of the reprocessor (i.e., we fix the inclination angle of the system, $\theta_{\rm obs}$, to $\sim 90°$), even if the toroidal geometry is slightly different between the two models[1].

[1]As pointed out by Liu and Li (2015), en edge-on `Torus` model in a CT regime may overestimate the soft X-ray spectrum.

Finally, to model the aforementioned scattered power law at low energies, the general procedure is to tie all the power law parameters to the primary one (i.e., photon index, redshift, normalization) and multiply it by a constant, namely f_s, which is a free parameter in the fit that quantifies the fraction of the primary power law scattered at low energies.

2.2 The NuSTAR survey of bright *Swift*-BAT AGN

As already discussed in Section 1.3, in the last few years, NuSTAR began a comprehensive program of hard X-ray surveys, both Galactic (e.g, Mori et al., 2015; Tomsick et al., 2017; Fornasini et al., 2017) and Extragalactic (e.g., Civano et al., 2015; Mullaney et al., 2015; Lansbury et al., 2017b).
As part of its Extragalactic Survey program, a survey of ~ 100 bright AGN detected by *Swift*-BAT was also conducted (see Baloković et al., 2014, for some early results; Baloković et al., in prep). In particular, a subsample of these bright, local AGN is composed by water megamasers.
This class of objects is particularly interesting because of an observed empirical correlation between high obscuration and detected maser emission at ~ 22 GHz.

2.3 Megamasers

A maser is, in analogy with a laser, a physical phenomenon in which a background radiation field stimulates emission by a population of properly excited atoms or molecules. The difference between the well known laser and a maser is about the frequency at which the emission happens: lasers are in the optical band, masers in the microwaves. Consider an atom excited in a metastable energy level: if an incoming photon has the right frequency ν, and the right energy $E_\nu = h\nu$ equal to the energy difference between the metastable and stable energy levels, the atom will be stimulated to relax in the stable energy level, emitting a second photon with the same frequency, phase and direction of the incoming one. This phenomenon is well known since a century, and was first studied by Einstein (1916).
Masers were first studied in laboratory, and then discovered in astrophysical sources. The first ones were hydroxyl and water masers, associated to protostars, HII regions and molecular clouds within the Milky Way (Perkins, Gold, and Salpeter, 1966; Litvak, 1969). Such masers were classified as masers or kilomasers, based on their isotropic luminosity with respect to the solar luminosity, of the order of $10^3\ L_\odot$. Later on, OH and H_2O extragalactic masers were discovered (Churchwell et al., 1977), and were classified as megamasers, having an isotropic luminosity $L > 10^6\ L_\odot$. Megamasers were usually spatially coincident with the nuclei of those galaxies in which they were residing. Due to its nature, the maser emission requires no thermodynamical equilibrium in a population of atoms or molecules, which has to be energetically pumped

(i.e., with molecules in a metastable excited state). In particular, precise physical conditions must be met in order to have non-thermal equilibrium, which depend on the masing molecule; for the water molecule, high density and temperature are required ($10^7 < n_{\rm H} < 10^{11}$ cm^{-3}, $400 < T < 1000$ K; see Lo, 2005). In addition to these physical conditions, the geometry of the system plays a crucial role, since the gain of the stimulated emission depends on the path length. This is due to the very nature of stimulated emission, since the emitted photon has the same direction of the incoming one, rapidly giving rise to a narrow beam of photons that, in turn, stimulates the emission of other photons in the same direction.
In general, water megamasers are due to a rotovibrational transition of the H_2O molecule at 22.23 GHz. Many other transitions are possible at different frequencies, but in this Thesis we are going to focus on 22 GHz water megamasers. They were associated to some sort of nuclear activity since their discovery in the late seventies, and became gradually more and more studied. Nowadays, depending on their geometry, three types of water megamasers are known: jet megamasers, outflow megamasers, and disk megamasers (see Tarchi, 2012, for a review).

2.3.1 Disk megamasers

The typical spectral signature for the presence of a disk megamaser is a triple-peaked profile of the 22 GHz maser line, where the principal peak, called the systemic one, is redshifted at the systemic velocity of the galaxy, while other two smaller peaks (or, better, line complexes) symmetrically bracket the systemic one, equally redshifted and blueshifted from it. These two secondary peaks are called high-velocity peaks and are interpreted as the signature of an edge-on rotating disk. Such structures rapidly gained the scientific interest of a large community, since they provide evidence for rotating molecular clouds around massive central objects. Being the tracers of accretion of molecular disks onto compact objects at the sub-pc scale, the physics and geometry of accretion can be studied with unprecedented detail up to Mpc distances. Moreover, the maser spots sometimes follow a Keplerian rotation curve (with NGC4258 being the archetypal system), allowing the enclosed mass to be precisely computed. Disk megamasers represent today the "golden standard" for SMBHs masses, and by monitoring the systemic maser spots, also the geometric distance to the host galaxy can be measured with a precision as high as $\sim 3\%$ without assuming any cosmological model (e.g., Reid et al., 2013). The Megamaser Cosmology Project[2] (MCP) aims at using a clean sample of megamaser disks to get a cosmology-independent estimate of the Hubble constant H_0. Figure 2.5 shows the maser spectrum of one of the latest disks discovered by the MCP, NGC5765B (Gao et al., 2016), while Figure 2.6a and 2.6b show the VLBI map and Position-Velocity (P-V) diagram, respectively. The VLBI map shows a clear thin disk with an edge-on geometry structure, where the spots are color-coded by

[2] https://safe.nrao.edu/wiki/bin/view/Main/MegamaserCosmologyProject

their Local Standard Rest (LSR) velocity. In the P-V diagram, the Keplerian rotation of the blue and redshifted spots is demonstrated.

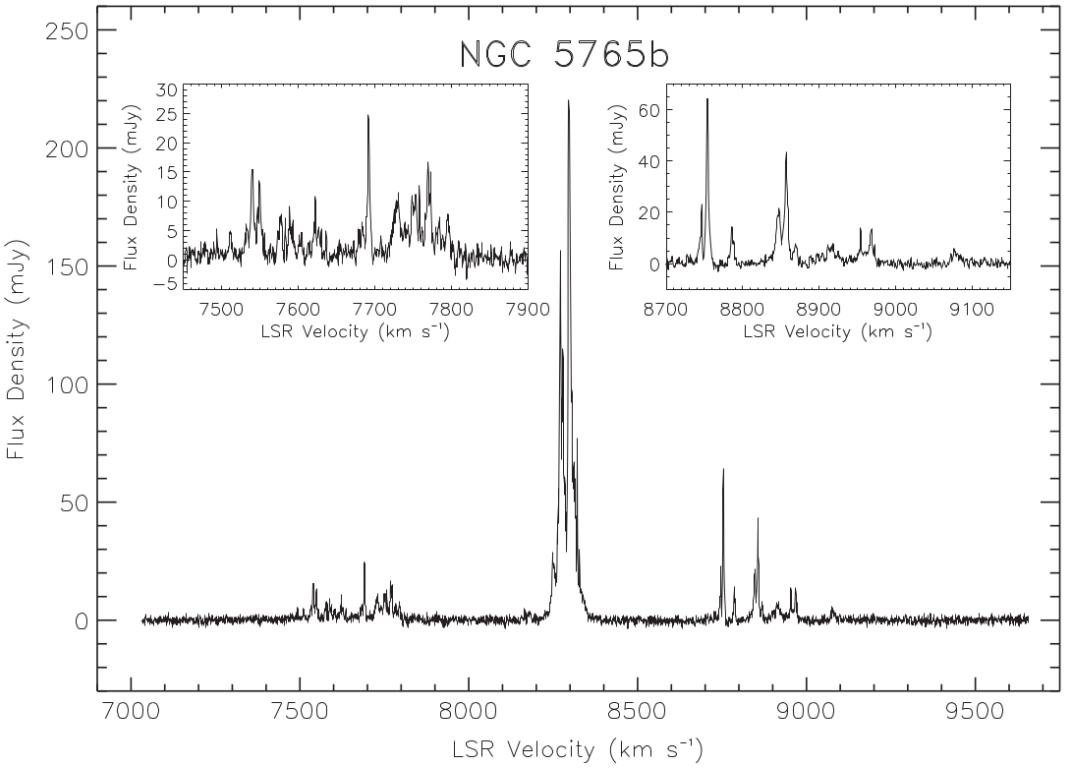

FIGURE 2.5: Maser spectrum of NGC5765B, where the systemic peak stands in the middle of other two complexes, called high-velocity peaks, zoomed into the two insets. Note that each of the peaks represents a so-called maser spot, presumably a molecular cloud rotating and emitting water maser emission. Such a triple-peaked spectrum is the evidence for an edge-on rotating disk. Figure adapted from Gao et al. (2016).

2.4 Disk Megamasers and SMBHs demographics

The scientific interest for water megamasers with a disk geometry is not limited to cosmology, but also extends to galaxy evolution and SMBHs demographics. Recently, disk megamasers started to catch the interest of a larger and larger community, thanks to their "golden" measurements of masses (van den Bosch et al., 2016). These particular megamasers are always found in late type spiral galaxies, often with a circumnuclear bar and/or a nuclear pseudobulge. Moreover, disk megamasers are found around low-mass SMBHs ($M_{\rm BH} \leq 10^7$), and are systematically offset by the famous and already mentioned $M_{\rm BH} - \sigma_*$ relation (Greene et al., 2016). Megamasers become then more and more important as their number grows, to calibrate the $M_{\rm BH} - \sigma_*$ relation, or to explore its universality. Moreover, precise masses from megamasers can be used to cross-calibrate different methods to calculate SMBH masses (e.g., reverberation mapping, gas/stellar dynamics) and better study systematics in each method.

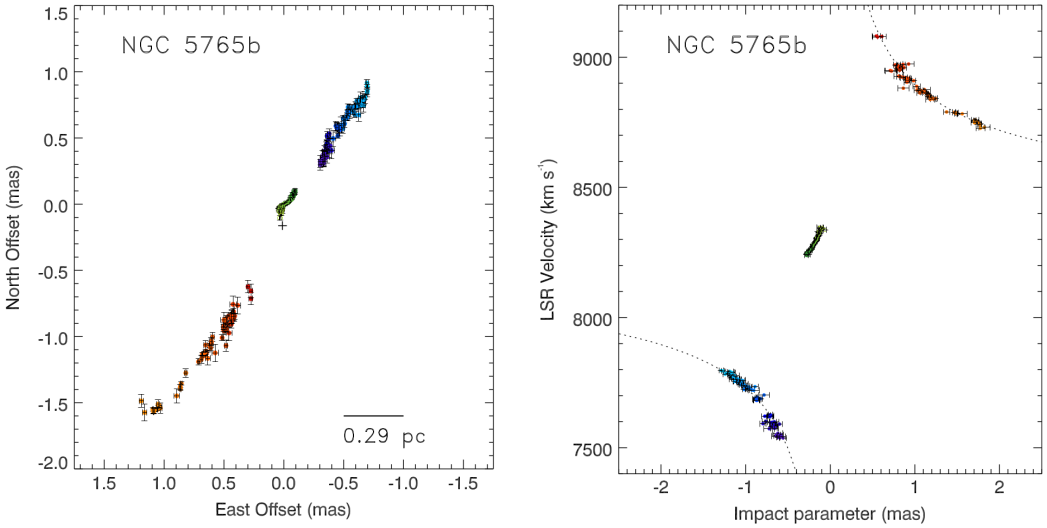

(A) (B)

FIGURE 2.6: **(A).** VLBI map of the maser spots in NGC5765b, color-coded by their local standard rest (LSR) velocities. The green spots mark the systemic masers, while the blue and red spots mark the high-velocity features. The geometry is of an edge-on thin disk. **(B).** Position-velocity (P-V) diagram of the detected maser spots in NGC5765b. The fits to the high-velocity spots are of a Keplerian rotation curve. Figures adapted from Gao et al. (2016).

2.5 Disk Megamasers and obscured AGN

From the point of view of AGN, there is strong evidence that water megamasers with a disk geometry tend to be found in Seyfert 2 (Sy2) galaxies and, in particular, in Compton-thick ones (Greenhill, Tilak, and Madejski, 2008), which according to the AGN unification scheme, are likely to be those where the obscuring structure is seen nearly edge-on. Their importance in modern astrophysics has been already discussed in Section 1.2.2.

High-quality hard X-ray (> 10 keV) data coupled with high-resolution radio maps of the nuclear emission allow new studies of the physics of obscured AGN. Some previous work concentrated on the connection between masing activity and high obscuring column densities in active nuclei, identifying some general and phenomenological results (Greenhill, Tilak, and Madejski, 2008; Castangia et al., 2013). However, many questions are still unanswered. Physical conditions, such as the temperature, density, and pressure of matter in the vicinity of the SMBH, are still uncertain. It is not completely clear whether the maser emission is associated with the outer part of the accretion disk or if it is part of the toroidal structure obscuring the nucleus along our line of sight.

TABLE 2.1: Megamaser sample, global properties, and references. The last three sources are the ones lacking NuSTAR data. (1) - Galaxy name. (2) - Redshift. (3) - Best fit intrinsic column density. (4) - Logarithm of the best fit intrinsic (deabsorbed) $2-10$ keV luminosity. (5) - References for columns (3) - (4): Are14 - Arévalo et al. (2014); Bau15 - Bauer et al. (2015); Cas13 - Castangia et al. (2013); Puc14 - Puccetti et al. (2014). (6) - AGN central mass. (7) - References for column (6): Gre03 - Greenhill et al. (2003); Til08 - Tilak et al. (2008); Kon08 - Kondratko, Greenhill, and Moran (2008); Kuo11 - Kuo et al. (2011); Lod03 - Lodato and Bertin (2003); McC13 - McConnell and Ma (2013); Yam12 - Yamauchi et al. (2012). (8) - Dust sublimation radius, calculated using the relation from Gandhi et al. (2009). See §2.7 for details. (9) - Maser disk inner and outer radii. (10) - References for column (9): Gre97 - Greenhill, Moran, and Herrnstein (1997); Kon05 - Kondratko, Greenhill, and Moran (2005).

Name	z	$N_{\rm H}$ $[10^{24}$ cm$^{-2}]$	$\log(L_{2-10})$ [erg s^{-1}]	Ref.	$M_{\rm BH}$ $[10^6\ M_\odot]$	Ref.	$R_{\rm d}$ [pc]	Disk size [pc]	Ref.
(1)	(2)	(3)	(4)	(5)	(6)	(7)	(8)	(9)	(10)
NGC 1068	0.0038	>5.6	43.34	Bau15	8.0 ± 0.3	Lod03	0.27	0.65 - 1.1	Gre97
NGC 1194	0.0136	$1.4^{+0.3}_{-0.2}$	42.78	this work	65 ± 3	Kuo11	0.14	0.54 - 1.33	Kuo11
NGC 1386	0.0029	5 ± 1	41.90	this work	$1.2^{+1.1}_{-0.6}$	McC13†	0.05	0.44 - 0.94	Til08
NGC 2273	0.0061	>7.3	43.11	this work	7.5 ± 0.4	Kuo11	0.20	0.034 - 0.20	this work*
NGC 2960	0.0165	$0.5^{+0.4}_{-0.3}$	41.41	this work	11.6 ± 0.5	Kuo11	0.03	0.13 - 0.37	Kuo11
NGC 3079	0.0037	2.5 ± 0.3	42.15	this work	$2.4^{+2.4}_{-1.2}$	McC13†	0.07	0.4 - 1.3	Kon05
NGC 3393	0.0125	$2.2^{+0.4}_{-0.2}$	43.30	this work	31 ± 2	Kon08	0.25	0.17 - 1.5	Kon08
NGC 4388	0.0084	0.44 ± 0.06	42.59	this work	8.5 ± 0.2	Kuo11	0.11	0.24 - 0.29	Kuo11
NGC 4945	0.0019	3.5 ± 0.2	42.52	Puc14	$1.4^{+0.7}_{-0.5}$	McC13†	0.10	0.13 - 0.41	this work**
IC 2560	0.0098	>6.7	42.98	this work	3.5 ± 0.5	Yam12	0.17	0.087 - 0.335	Yam12
Circinus	0.0015	8.7 ± 1.5	42.57	Are14	1.7 ± 0.3	Gre03	0.11	0.11 - 0.4	Gre03
NGC 4258	0.0015	0.087 ± 0.003	41.2	Cas13	39 ± 3	Til08	0.02	0.12 - 0.28	Til08
NGC 6264	0.0340	>1	42.6	Cas13	29.1 ± 0.4	Kuo11	0.11	0.24 - 0.80	Kuo11
UGC 3789	0.0109	>1	42.3	Cas13	10.4 ± 0.5	Kuo11	0.08	0.084 - 0.30	Kuo11

† Maser method mass for which in the original paper an uncertainty is not provided. The error given by McConnell and Ma (2013) is overestimated.

†† Error replaced by the average error of maser method; see §2.6.2.

* New maser disk extension estimate from VLBI maps.

** Adapted from Greenhill, Moran, and Herrnstein (1997).

2.6 Data and spectral analysis

2.6.1 The sample

To build up a sample of disk megamaser sources with high-quality maser maps, precise black hole mass estimates, and hard X-ray spectral coverage, we cross-correlated a list of VLBI-mapped water megamasers from the Megamaser Cosmology Project[3] (MCP, see Henkel et al., 2012) with NuSTAR observations and well known disk maser sources studied in the literature. We found 11 objects. We then enlarged the sample by adding three more sources with VLBI radio maps available, but lacking NuSTAR data (refer to Castangia et al., 2013, for X-ray and maser disk properties of these). The total sample is then composed of 14 sources, which are all the disk water megamasers known today with both precise VLBI maps and hard X-ray spectra. Their main properties are listed in Table 2.1. However, we emphasize that this is not a complete sample of all the water megamasers known today, which can be found in Pesce et al. (2015).

2.6.2 Data reduction

We present NuSTAR hard X-ray spectral results for 11 sources. In particular, we use archival data for NGC 1194, NGC 1386, NGC 2273, NGC 2960, NGC 3079, NGC 3393, NGC 4388, and IC 2560, for which observation dates and exposure times can be found in Table 2.2. For NGC 4945, NGC 1068, and the Circinus galaxy, spectral parameters are taken from Puccetti et al. (2014), Bauer et al. (2015), and Arévalo et al. (2014), respectively.

The raw events files were processed using the NuSTAR Data Analysis Software package v. 1.4.1 (NuSTARDAS)[4]. Calibrated and cleaned event files were produced using the calibration files in the NuSTAR CALDB (20150225) and standard filtering criteria with the `nupipeline` task. We used the `nuproducts` task included in the NuSTARDAS package to extract the NuSTAR source and background spectra using the appropriate response and ancillary files. We extracted spectra and light curves in each focal plane module using circular apertures of different radii, aimed at optimizing the signal-to-noise ratio at high energies for every source (see Baloković et al. in prep., for further details). Background spectra were extracted using source-free regions on the same detector as the source. All spectra were binned to a minimum of 20 photons per bin using the HEAsoft task `grppha`.

NGC 1194

NGC 1194 is a nearby Seyfert 1.9 galaxy. It hosts a circumnuclear maser disk, which allowed a precise measurement of the BH mass of $(6.5 \pm 0.3) \times 10^7\ M_\odot$ (Kuo et al., 2011). Fitting the spectrum with an absorbed power law using a Galactic column returns an uncharacteristically hard photon index ($\Gamma \sim 0.5$) and leaves large residuals,

[3] `http://safe.nrao.edu/wiki/bin/view/Main/PublicWaterMaserList`

[4] `http://heasarc.gsfc.nasa.gov/docs/nustar/analysis/nustar_swguide.pdf`

TABLE 2.2: NuSTAR observation details for the eight sources analyzed.

Name	Date of observation	Exposure time [ks]
NGC 1194	2015-Feb-28	31
NGC 1386	2013-Jul-19	21
NGC 2273	2014-Mar-23	23
NGC 2960	2013-May-10	21
NGC 3079	2013-Nov-12	21
NGC 3393	2013-Jan-28	15
NGC 4388	2013-Dec-27	21
IC 2560	2013-Jan-28, 2014-Jul-16	73

in particular a prominent line feature at $\sim 6-7$ keV and an excess between 10 and 30 keV (χ^2/ν = 494/117). These are typical spectral signatures of an obscured AGN. A `plcabs` model (which accounts for obscuration) with two intrinsically narrow (σ = 10 eV) Gaussian components for the lines at $6-7$ keV returns a much better fit (χ^2/ν = 186/112). The obscuration is in the Compton-thin regime ($N_{\rm H} \sim 6 \times 10^{23}$ cm^{-2}), and the photon index is ~ 1. The residuals still show a hump at ~ 20 keV and signatures of soft excess at energies < 5 keV. A better fit is obtained if `plcabs` is replaced by a `pexrav` model (χ^2/ν = 96/113, $\Gamma \sim 1.6$). Using both models returns an even better fit with $\Gamma \sim 1.6$ and $N_{\rm H} \sim 10^{24}$ cm^{-2} (χ^2/ν = 85/111), in which the `plcabs` component is still significant at more than 99% confidence limit. This appears to be an unphysical situation, since the flux in the reflected component is much greater than the total intrinsic flux of the source.

We then apply more physically self-consistent models. An almost edge-on `Torus` model with a fixed opening angle ($\theta_{\rm tor}$ = 60°) returns an unacceptable fit (χ^2/ν = 220/116), with $\Gamma \sim 1.4$ and $N_{\rm H} \sim 7 \times 10^{23}$ cm^{-2}. The fit can be improved by fitting for the torus opening angle (χ^2/ν = 201/116), which has a best fit value of $\theta_{\rm tor}$ = 26° (the lower limit accepted by the model) with $\Gamma \sim 1.4$ and $N_{\rm H} \sim 6 \times 10^{23}$ cm^{-2}. A `MYTorus` model in its default configuration (i.e., coupled mode) returns a similar fit to the `Torus` one: χ^2/ν = 217/116, $\Gamma \sim 1.4$ and $N_{\rm H} \sim 6 \times 10^{23}$ cm^{-2}. A common feature of these models is the underprediction of both the flux of the line component at $6-7$ keV (see, e.g., Vasylenko et al., 2015) and the emission below 5 keV. A `MYTorus` model in its decoupled mode is then applied (χ^2/ν = 161/115). The front-scattered component vanishes, the photon index is ~ 1.6, and the column density is $\sim 10^{24}$ cm^{-2}. These values are consistent with what is found by applying phenomenological models in the first part of the analysis. We note that scattering $\sim 3\%$ of the primary continuum into a scattered power law and adding a line feature at (6.8 ± 0.1) keV do not change the fundamental fit parameters, but improve it at more than 99% confidence limit (χ^2/ν =113/112, $\Delta\chi^2/\Delta\nu$ = 48/3). Even if the best fit model is made up of a combination of `plcabs`, `pexrav`, and `zgauss` models (χ^2/ν = 85/111), we choose to rely on the best fit among the self-consistent ones, as for

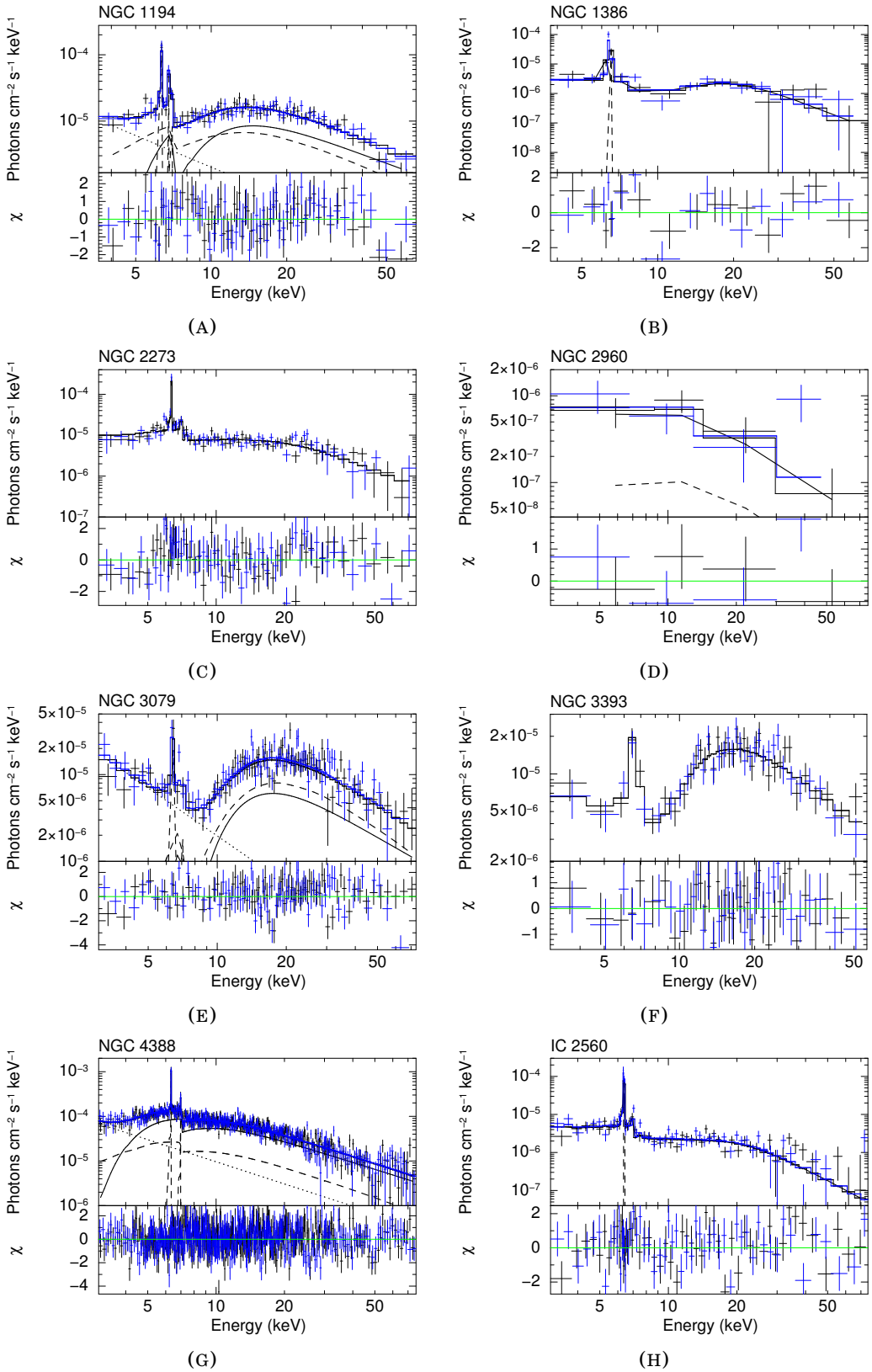

FIGURE 2.7: NuSTAR spectra, best-fitting models and residuals for the eight sources analyzed. FPMA data are shown in black, while FPMB ones are shown in blue. When adopting a `MYTorus` model, the solid line represents the primary continuum. The reflection and line components are shown as the dashed line, while the scattered power law is shown as the dotted line. When adopting the `Torus` model, the solid line represents the total spectrum, while add-on line components are shown as the dashed line.

TABLE 2.3: NuSTAR X-ray best fit spectral results for the eight sources analyzed.

Parameter	NGC 1194	NGC 1386	NGC 2273	NGC 2960	NGC 3079	NGC 3393	NGC 4388	IC 2560
Best fit model	MYT D	T	T	MYT	MYT	T	MYT D	T
χ^2/ν	113/112	32/25	123/113	6/5[a]	189/152	49/69	693/681	125/104
Γ	1.59 ± 0.15	> 2.6	2.1 ± 0.1	1.9 (f)	1.8 ± 0.2	1.8 ± 0.2	1.65 ± 0.08	2.7 ± 0.1
$N_{\rm H}$ [cm^{-2}]	$1.4^{+0.3}_{-0.2} \times 10^{24}$	$(5 \pm 1) \times 10^{24}$	$> 7.3 \times 10^{24}$	$5^{+4}_{-3} \times 10^{23}$	$(2.5 \pm 0.3) \times 10^{24}$	$2.2^{+0.4}_{-0.2} \times 10^{24}$	$4.4 \pm 0.6 \times 10^{23}$	$> 6.7 \times 10^{24}$
A_{Z90}[b]	$0.003^{+0.003}_{-0.002}$	0.07 ± 0.01	$0.07^{+0.02}_{-0.01}$	$1.5^{+2.0}_{-0.7} \times 10^{-4}$	$0.014^{+0.013}_{-0.007}$	$0.017^{+0.012}_{-0.008}$	$0.006^{+0.002}_{-0.001}$	$0.046^{+0.016}_{-0.013}$
A_{S90}[c]	~ 0	-	-	1 (f)	1 (f)	-	~ 0	-
A_{L90}	$= A_{S90}$	-	-	$= A_{S90}$	$= A_{S90}$	-	$= A_{S90}$	-
A_{S00}[c]	$0.8^{+0.4}_{-0.3}$	-	-	-	-	-	$1.7^{+0.6}_{-0.4}$	-
A_{L00}	$= A_{S00}$	-	-	-	-	-	$= A_{S00}$	-
$\theta_{\rm tor}$	-	< 40	73^{+6}_{-11}	-	-	79 ± 1	-	53 ± 23
$f_{\rm s}$ [%]	3 ± 1	< 0.5	< 0.03	-	$1.0^{+0.5}_{-0.4}$	< 0.4	8 ± 2	< 0.1
F_{2-10} [erg cm^{-2} s^{-1}]	1.2×10^{-12}	2.8×10^{-13}	9.5×10^{-13}	5.8×10^{-14}	6.2×10^{-13}	5.1×10^{-13}	7.8×10^{-12}	4.0×10^{-13}
F_{10-40} [erg cm^{-2} s^{-1}]	1.1×10^{-11}	1.4×10^{-12}	5.3×10^{-12}	3.0×10^{-13}	1.2×10^{-11}	1.2×10^{-11}	3.2×10^{-11}	1.3×10^{-12}
$L^{\rm int}_{2-10}$[d] [erg s^{-1}]	6.0×10^{42}	8.0×10^{41}	1.3×10^{43}	2.6×10^{41}	1.4×10^{42}	2.0×10^{43}	3.9×10^{42}	9.5×10^{42}
$L^{\rm int}_{10-40}$[d] [erg s^{-1}]	9.6×10^{42}	1.5×10^{41}	9.3×10^{42}	3.1×10^{41}	1.6×10^{42}	2.3×10^{43}	5.7×10^{42}	2.9×10^{42}
FPMB/FPMA	0.99 ± 0.06	1.1 ± 0.2	1.0 ± 0.1	$0.9^{+0.5}_{-0.4}$	1.06 ± 0.08	1.0 ± 0.1	1.02 ± 0.03	1.0 ± 0.1
$\lambda_{\rm Edd}$[e]	0.012 ± 0.003	$0.09^{+0.08}_{-0.05}$	0.23 ± 0.06	$0.0030^{+0.0008}_{-0.0008}$	$0.08^{+0.08}_{-0.04}$	0.09 ± 0.02	0.06 ± 0.02	0.4 ± 0.1

T = Torus, MYT = MYTorus, MYT D = MYTorus decoupled.

[a] Data for NGC 2960 are just a NuSTAR 3σ detection, so we used the Cash statistic (Cash, 1979) for fitting purposes. We report the reduced χ^2 just for its straightforward interpretation.

[b] Normalization at 1 keV of the direct power law in units of photons keV^{-1} cm^{-2} s^{-1}.

[c] Following Murphy and Yaqoob (2009), A_{S90}, A_{L90}, A_{S00}, A_{L00} are just multiplicative factors of the respective components, and such, lack physical units. To obtain normalizations at 1 keV in units of photons keV^{-1} cm^{-2} s^{-1}, the reader should multiply these factors for the primary normalization, i.e. A_{Z90}.

[d] Luminosities are intrinsic, i.e. corrected for absorption.

[e] The Eddington ratio is calculated as $k_{\rm bol} \times L^{\rm int}_{2-10}/L_{\rm Edd}$, where $k_{\rm bol} = 20 \pm 5$ is the bolometric correction, constant in our range of 2 – 10 keV luminosities.

the other sources, which is the decoupled MYTorus model (see Figure 2.7a).
In summary, given that phenomenological models point toward a highly obscured, reflection-dominated source and that the best fit in a physical and self-consistent model is represented by a back-scattered radiation-dominated MYTorus model, we conclude that NGC 1194 is a Compton-thick AGN with the column density $N_{\rm H} = 1.4^{+0.3}_{-0.2} \times 10^{24}$ cm^{-2}, consistent with the one reported by Greenhill, Tilak, and Madejski (2008). We note that, according to the best fit model, reflection only dominates below ~10 keV. Best fit spectral parameters are given in Table 2.3.

NGC 1386

NGC 1386 hosts a water maser source (Braatz et al., 1997), although it is not clear whether the maser spots trace a rotating thin disk or align in front of an underlying continuum (i.e., are jet masers). This makes the central black hole mass estimate challenging so we adopted the one reported by McConnell and Ma (2013)[5], which is $1.2^{+1.1}_{-0.6}$ $\times$ 10^6 $M_\odot$. A default MYTorus model fails (χ^2/ν = 131/27), and two statistically indistinguishable sets of parameters are possible: one with a Compton-thin obscuration ($N_{\rm H} \sim$ 6 $\times$ 10^{23} cm^{-2}) and $\Gamma \sim$ 1.4, and one with a severely obscured AGN ($N_{\rm H} \sim$ 10^{25} cm^{-2}) and $\Gamma \sim$ 2.6. A decoupled MYTorus model points toward a back-scattered radiation-dominated spectrum with the same parameters as for the coupled case (χ^2/ν = 65/25). The unacceptable fit (χ^2/ν = 57/27) of the Torus model arises from an underestimation of the line contribution and provides the best χ^2 among the physical models. Following Brightman et al. (2015), we added a line component to the fit at (6.5 $\pm$ 0.1) keV and get χ^2/ν = 32/25. A scattered power law is not required by the data (Figure 2.7b). The central source is then obscured by Compton-thick material of column density $N_{\rm H}$ = (5 $\pm$ 1) $\times$ 10^{24} cm^{-2}. Best fit parameters are given in Table 2.3. We note that our results agree with Brightman et al. (2015), where they focused on the Torus model for a covering factor estimate.

NGC 2273

The mass of the SMBH nested in the barred spiral galaxy NGC 2273 was measured by Kuo et al. (2011) to be $M_{\rm BH}$ = (7.5 $\pm$ 0.4) $\times$ 10^6 $M_\odot$. The reported parameters put the maser disk very close to the central engine (0.028 - 0.084 pc). This makes NGC 2273 an outlier in some relations (Castangia et al., 2013). To determine whether it is truly an outlier or whether emission at larger radii is missed by the VLBI observations, we derived radii from the more sensitive single-dish spectra taken with the Green Bank Telescope (Kuo et al., 2011). To do so, we assumed a systemic velocity of 1840 km/s (from NED[6]), a SMBH mass of 7.5 $\times$ 10^6 $M_\odot$ (Kuo et al., 2011), and Keplerian rotation (Kuo et al., 2011). From the highest and lowest velocity emission (we require the emission to be at least 5 times the RMS) of the high-velocity maser features, we find

[5] http://blackhole.berkeley.edu/
[6] http://ned.ipac.caltech.edu/

that the innermost radius is ~ 0.034 pc, consistent with Kuo et al. (2011), but that the outermost radius is ~ 0.2 pc. We adopt these values in the following analysis.
A MYTorus model cannot account for the line emission, and it gives an unacceptable fit (χ^2/ν = 267/113). Its decoupled mode provides an acceptable fit (χ^2/ν = 131/111), pointing toward a back-scattered, reflection-dominated AGN. However, the best fit is found with the Torus model, where the source is heavily Compton-thick and a lower limit on the column density is found ($N_{\rm H} > 7.3 \times 10^{24}$ cm^{-2}), consistently with Guainazzi et al. (2005) and Awaki et al. (2009). Torus spectral parameters are found in Table 2.3, while the best fit model is shown in Figure 2.7c.

NGC 2960

The central black hole mass of the spiral megamaser galaxy NGC 2960 (Mrk 1419) as reported by Kuo et al. (2011) is (1.16 ± 0.05) × 10^7 $M_\odot$. NGC 2960 is very faint, and a 21 ks NuSTAR snapshot resulted in poor quality data that prevented us from significantly constraining spectral parameters. The fitting procedure in XSPEC was carried out using the Cash statistic (Cash, 1979), but we report the reduced χ^2 for direct comparison with other sources. Using a default MYTorus model and fixing the photon index Γ = 1.9 (Figure 2.7d), the fit returns an obscured, but Compton-thin, source ($N_{\rm H} = 5^{+4}_{-3} \times 10^{23}$ cm^{-2}), which is marginally consistent with Greenhill, Tilak, and Madejski (2008). Results are listed in Table 2.3.

NGC 3079

The low ionization nuclear emission-line region (LINER) galaxy NGC 3079 presents a thick, flared, probably star-forming and self-gravitating maser disk (Kondratko, Greenhill, and Moran, 2005). The disk's outer radius is indeed beyond the sphere of influence radius of the central mass, which is $2.4^{+2.4}_{-1.2} \times 10^6$ $M_\odot$ (McConnell and Ma, 2013). Either Torus (χ^2/ν = 193/152) or MYTorus (χ^2/ν = 189/152), both with a scattered power law dominating below 5 keV, give similar results. Using a decoupled MYTorus model (χ^2/ν = 189/150), the back-scattered contribution vanishes, confirming that the source is dominated by reflection below 10 keV. We therefore chose the coupled MYTorus model as the best fit (Figure 2.7e) and conclude that NGC 3079 is transmission-dominated with a column density of $N_{\rm H}$ = (2.5 ± 0.3) × 10^{24} cm^{-2} (see Table 2.3 for other parameters). This result agrees with the one found by Brightman et al. (2015) using the Torus model.

NGC 3393

The nearby barred galaxy NGC 3393 presents an edge-on maser disk that allowed Kondratko, Greenhill, and Moran (2008) to measure the central mass to be (3.1 ± 0.2) × 10^7 $M_\odot$. An excellent fit is found with a Torus model (χ^2/ν = 49/69), with parameters reported in Table 2.3. This fit is formally indistinguishable from a MYTorus model with a scattered power law in the soft part of the spectrum, either coupled or decoupled

(χ^2/ν = 49/69 and χ^2/ν = 48/67, respectively), but we chose `Torus` as the best fit because it only requires one component (i.e., the scattered power law is not significant, see Figure 2.7f). However, the spectral parameters are the same within the uncertainties. We therefore conclude that NGC 3393 hosts a Compton-thick AGN ($N_{\rm H} = 2.2^{+0.4}_{-0.2} \times 10^{24}$ cm^{-2}), in agreement with the results of Koss et al. (2015).

NGC 4388

The Virgo cluster member NGC 4388 hosts an active SMBH of mass (8.5 ± 0.2) × 10^6 $M_\odot$ (Kuo et al., 2011). In their paper, Kuo et al. (2011) suggest using this mass value with caution because of the lack of systemic maser activity and the inability to robustly assess the Keplerian motion of the maser spots. Among the self-consistent models (`Torus`, `MYTorus` coupled, `MYTorus` decoupled) the last gives the best χ^2, although spectral parameters are consistent among them all. A `Torus` model points toward smaller opening angles (i.e., larger covering factor, ~ 0.9), which could account for the line emission (χ^2/ν = 761/684). Fitting with `MYTorus` in coupled mode underestimates the line feature (χ^2/ν = 803/684). This could be due to supersolar iron abundance, a broad range of $N_{\rm H}$ with different covering factors, or to a covering factor greater than that of the model, as suggested by the `Torus` model. Decoupling `MYTorus` does not change the general results, while the back-scattered radiation seems to be favored over the vanishing front-scattered one (χ^2/ν = 729/682). The fit can be improved by adding a scattered power law below 5 keV, which brings the reduced chi-squared to χ^2/ν = 693/681 (Figure 2.7g). According to the best fit model, NGC 4388 is a Compton-thin ($N_{\rm H}$ = 4.2 ± 0.5 × 10^{23} cm^{-2}) transmission-dominated source, and our results agree with the constraints implied by its known hard X-ray variability on scales of days (Caballero-Garcia et al., 2012) and months (Fedorova et al., 2011). The `MYTorus` best fit parameters are reported in Table 2.3.

IC 2560

The barred spiral galaxy IC 2560 hosts a (3.5 ± 0.5) × 10^6 $M_\odot$ active SMBH surrounded by a thin molecular maser disk (Yamauchi et al., 2012) with uncertain geometry (Tilak et al., 2008). The hard X-ray spectrum is well known from previous studies to be reflection-dominated (Baloković et al., 2014; Brightman et al., 2015). A default `MYTorus` model cannot reproduce a reflection-dominated spectrum (χ^2/ν = 364/107). A decoupled version of this model does better (χ^2/ν = 194/105), where all the radiation is back-scattered by Compton-thick material. The best fit is obtained with the `Torus` model (χ^2/ν = 172/107), and adding a line component at (6.49 ± 0.06) keV significantly improves the fit (χ^2/ν = 127/105, Figure 2.7h). The column density is found to be > 6.7 × 10^{24} cm^{-2}. Best fit parameters are given in Table 2.3 and agree with previous results in the literature.

2.6.3 Summary of spectral analysis results

In this section we presented hard X-ray spectral analyses for eight of the megamaser sources observed by NuSTAR. Three quarters turn out to be Compton-thick, while one quarter are Compton-thin. Among the latter, NGC 2960 is a 3σ detection in the NuSTAR snapshot, while NGC 4388 is a well known variable source, presenting column density variability on the scale of days.
Moreover, we note that out of seven sources showing a line feature (we exclude NGC 2960 in this argument, because of its weak detection), two do not have their line component well fit by self-consistent models (`Torus` or `MYTorus`). In both cases (NGC 1386 and IC 2560), the line was underestimated by the models. Finally, we note that using a decoupled `MYTorus` model in the Compton-thin regime (such as in the case of NGC 4388) should be done with caution, since the scattered components could mimic the transmitted primary continuum.
However, in this Chapter we are primarily interested in a robust estimate of the absorption column density, rather than an exhaustive discussion of the spectral properties of individual sources, which will be presented elsewhere (Baloković et al. in prep.). As previously stated, the final sample is completed by adding three NuSTAR-observed well known megamasers (NGC 4945, NGC 1068, Circinus), and three other maser disk AGN whose X-ray (XMM-*Newton* based) and maser disk parameters are taken from Castangia et al. (2013). Summarizing, the fraction of Compton-thick AGN in our final sample of local disk megamasers is at least $\sim 79\%$ (11/14), comparable to the values reported in previous studies (76% – Greenhill, Tilak, and Madejski, 2008; 86% – Castangia et al., 2013) and confirming the tight relation between heavy obscuration and disk maser emission.

2.7 The connection between the maser disk and the torus

The aim of our work is to deepen our understanding of the connection between the torus (seen as the X-ray obscurer) and the maser disk (i.e., an ensemble of clouds orbiting the central black hole, showing water maser activity). First, we can localize the disk. The maser emission occurs too far from the central black hole (in our sample, inner maser radii range from 6.6×10^4 to 7.6×10^6 gravitational radii) to identify the maser disk with the standard accretion disk, which extends up to $\sim 10^3$ gravitational radii (Netzer, 2013, see §7.6, pp. 213- 216). Moreover, the presence of water molecules requires the environment to be dusty. We then expect that the maser disk lies outside the dust sublimation radius $R_{\rm d}$, which identifies the torus inner wall within the standard AGN framework (see, e.g., Netzer, 2015). We used the relation from Gandhi et al. (2009) to calculate $R_{\rm d}$ for our sample, adopting a sublimation temperature of 1500 K for graphite grains with an average radial size of 0.05 μm (Barvainis, 1987; Kishimoto et al., 2007). As expected, comparing $R_{\rm d}$ with the inner maser radius $R_{\rm in}$ and considering the uncertainties, all the sources have the maser disk within the dusty zone (i.e., $R_{\rm in} \geq R_{\rm d}$), except NGC 2273 (as already pointed out by Castangia et al., 2013).

The maser disk can then be generally considered part of the torus with two different possible geometries: one in which the maser disk is the inner, sub-parsec scale part of the equatorial plane of the classical torus, as in Figure 2.8a; and one in which the masing clouds are tracing a real geometrically thin disk that then inflates into a geometrically thicker end, required to have a large covering factor, as shown in Figure 2.8b. There are many cases in which the maser disk is seen to be warped (NGC 2273, NGC 2960, Kuo et al., 2011; NGC 4258, Herrnstein et al., 2005; NGC 6264, Kuo et al., 2011; Circinus, Greenhill et al., 2003), or inflating in its outer part (NGC3079, Kondratko, Greenhill, and Moran, 2005). In particular, in the case of Circinus, the warp is consistent with channeling the nuclear outflow.

These geometries are difficult to explain within the framework of Figure 2.8a. Moreover, the basic model of astrophysical maser emission theory predicts that the disk should be directly irradiated by X-rays coming from the central source (Neufeld, Maloney, and Conger, 1994). Again, this makes it difficult to explain the emerging disk when considering a geometry like Figure 2.8a. Finally, a steep density gradient in the vertical direction would be needed to only see edge-on maser emission; otherwise, maser disks would be ubiquitous among Sy2 galaxies, contrary to observations (Zhu et al., 2011). Here we do not have information on the torus vertical structure, but we can exploit the physical properties of the maser emission to infer something about the most likely geometry. High densities, nearly edge-on geometry, and a temperature range of $\sim 400 - 1000$ K are needed to have maser amplification (Lo, 2005).
In this work, we concentrate only on the density condition. It is indeed difficult to estimate the temperature of the masing gas that is not, by definition, in thermodynamic equilibrium. Instead, we can estimate the density of the masing region, defining the maser disk radial extent $\Delta R = R_{\rm out} - R_{\rm in}$, where $R_{\rm out}$ and $R_{\rm in}$ are the outer and inner radii of the maser disk. They are taken as the locations of the less red/blueshifted and most red/blueshifted maser spots with respect to the systemic velocity of the galaxy, if using the spectrum, or the innermost and outermost spots whether from systemic or red/blueshifted masers, if using the maps. With the disk extent and the column density measured from the X-rays, $N_{\rm H}$, we have a rough estimate of the mean density of the material along the line of sight:

$$\rho = \frac{N_{\rm H}}{\Delta R}\ [{\rm cm}^{-3}], \tag{2.1}$$

which we can compare with the densities predicted by astrophysical maser theory, $10^7 < \rho < 10^{11}$ cm^{-3} (Lo, 2005; Tarchi, 2012).
Looking at the density distribution in our sample, it is clear that densities obtained with (2.1) are too low by at least one order of magnitude. This is a hint that using (2.1) and identifying the absorbing medium with the maser disk is not completely appropriate, and if so, all megamaser sources in the sample should be severely obscured. Indeed, with an average density of 10^9 cm^{-3} in a fraction of a parsec, the column density of such a maser disk should be on the order of 10^{26} cm^{-2}. This is clearly not the

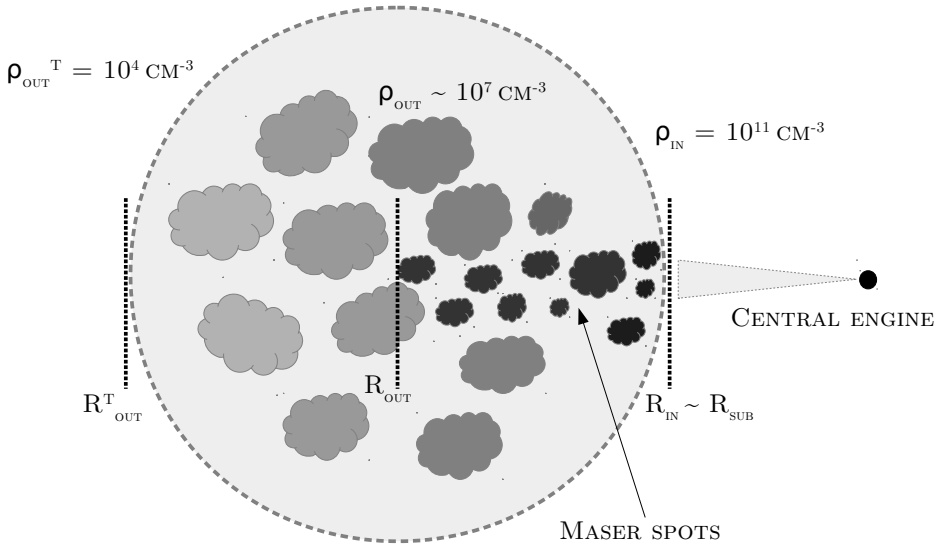

(A)

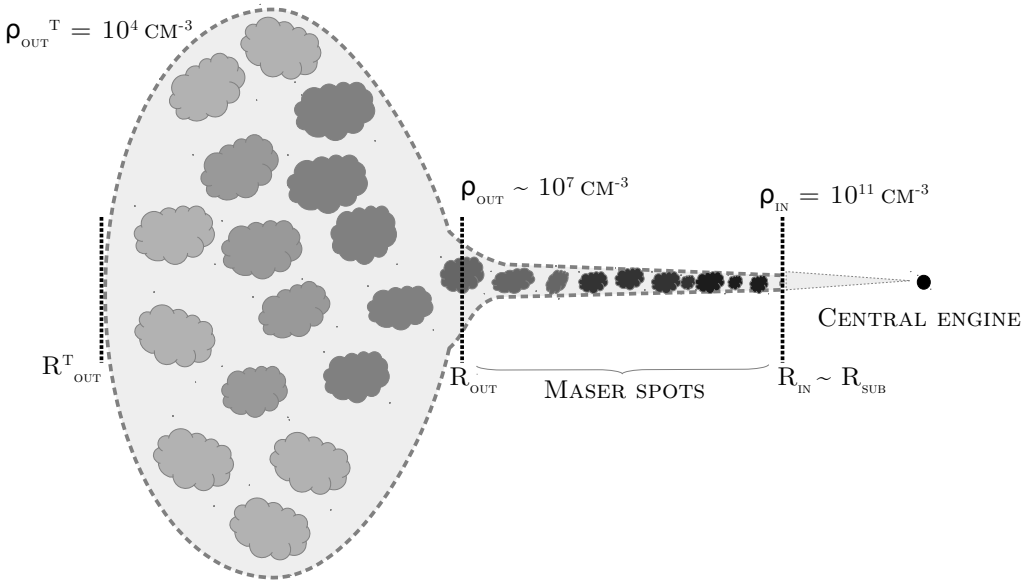

(B)

FIGURE 2.8: Sketches of the two possible geometries for the location of the maser disk inside the torus. Sizes are not to scale, and the sketches are just meant to display the different possible locations of the maser disk. **(A).** The disk is part of the equatorial plane of the torus. **(B).** The disk inflates in its outer part, giving rise to a geometrically thicker structure. The change from the inner part to the outer one is not abrupt and occurs with a gradual change in the dimensions and physical conditions of the clumps, encoded in the same density profile.

case, because 3 out of 14 sources are Compton-thin (i.e. ,$N_{\rm H} < 1.5 \times 10^{24}$ cm^{-2}), and 6 out of 14 are Compton-thick with $N_{\rm H} < 10^{25}$ cm^{-2}.

In general, the maser disk alone cannot replace the standard torus of the AGN unified model: it is too geometrically thin (otherwise nearly every Sy2 would be identified as a maser source, while nuclear water maser emission detection frequency is low, ~ 3%, Zhu et al., 2011) and too optically thick. There could be cases, however, in which a warped disk could simultaneously provide enough obscuration and low covering factor. We discuss this possibility in §2.8.3. Indeed, five sources of the sample present a lower limit on the column density and are therefore consistent with the absorber being the maser disk itself, seen exactly edge-on. Because the density increases overall, approaching the black hole, we may simply guess that the maser spots are detected in a high-density region in the inner part of the torus. Moreover, we can explain the tight relation between high obscuration and edge-on maser emission as a co-alignment between the maser clouds and the obscuring matter. In what follows, we then assume geometric alignment and continuity in the radial density profile between the maser disk and the inflated part of the torus, adopting a geometry as in Figure 2.8b.

An alternative view of the result obtained with Equation (2.1) involves clumpiness, which is addressed quite well by theoretical models. Models like the one by Elitzur and Shlosman (2006) study the interplay between the maser disk and the obscuring medium, followed by subsequent relevant work on this topic (e.g., Nenkova et al., 2008a; Nenkova et al., 2008b). Dusty and molecular clouds orbiting the central engine are expected to have column densities in the range $N_{\rm H} \sim 10^{22} - 10^{23}$ cm^{-2}, and a few clouds are able to provide the necessary obscuration measured with X-ray spectroscopy, together with rapid variability and the radiation reprocessing in the infrared band. Even if many questions are still unanswered, these works point toward the importance of considering a clumpy medium, rather than a smooth one, to interpret and explain many properties of AGN. In this paper, we use analytical expressions of average quantities, like the density, to get our results. Later on, we test whether this methodology is too simplistic or not.

2.7.1 A toy model

Suppose now that the inner and outer radii of the maser disk correspond to the theoretically expected upper and lower limits in density suitable to have maser emission, respectively, and assume a power law for the density profile, such as

$$\rho(r) = \rho_{\rm in} \left(\frac{r}{R_{\rm in}} \right)^{-\alpha}, \tag{2.2}$$

where α is the power law index, which can be estimated for every source taking $\rho_{\rm in} = 10^{11}$ cm^{-3} and $\rho_{\rm out} = 10^{7}$ cm^{-3}:

$$\alpha = \log\left(\frac{\rho_{\rm in}}{\rho_{\rm out}} \right) / \log\left(\frac{R_{\rm out}}{R_{\rm in}} \right) = \frac{4}{\log\left(\frac{R_{\rm out}}{R_{\rm in}} \right)}. \tag{2.3}$$

Once we have recovered the power law index for each source using the maser disk sizes from Table 2.1, a continuity assumption in the radial density profile between the maser disk and the external part of the torus allows us to estimate the torus outer radius. Identifying the outer end of the maser disk with the beginning of the inflated end and keeping the same α, the torus outer radius $R^{\rm T}_{\rm out}$ will be the distance at which the density falls to, say, 10^4 cm^{-3} (see Netzer, 2013, §7.5, pp. 205). This value has a negligible effect on results, as we show in the following:

$$R^{\rm T}_{\rm out} = R_{\rm out} 10^{\frac{1}{\alpha}\log(\rho_{\rm out}/\rho^{\rm T}_{\rm out})} = R_{\rm out} 10^{3/\alpha}. \tag{2.4}$$

Assuming a density profile continuity between the maser disk and the external part of the torus, with this simple toy model one can recover the torus size, and then integrate its density along the line of sight inside the inflated part alone, to recover the column density:

$$N_{\rm H} = \int_{R_{\rm out}}^{R^{\rm T}_{\rm out}} \rho(r) dr = \frac{\rho_{\rm out} R_{\rm out}}{\alpha - 1} \left[1 - \left(\frac{R^{\rm T}_{\rm out}}{R_{\rm out}} \right)^{1-\alpha} \right]. \tag{2.5}$$

Very interestingly, column densities calculated with (2.5) are in good agreement with

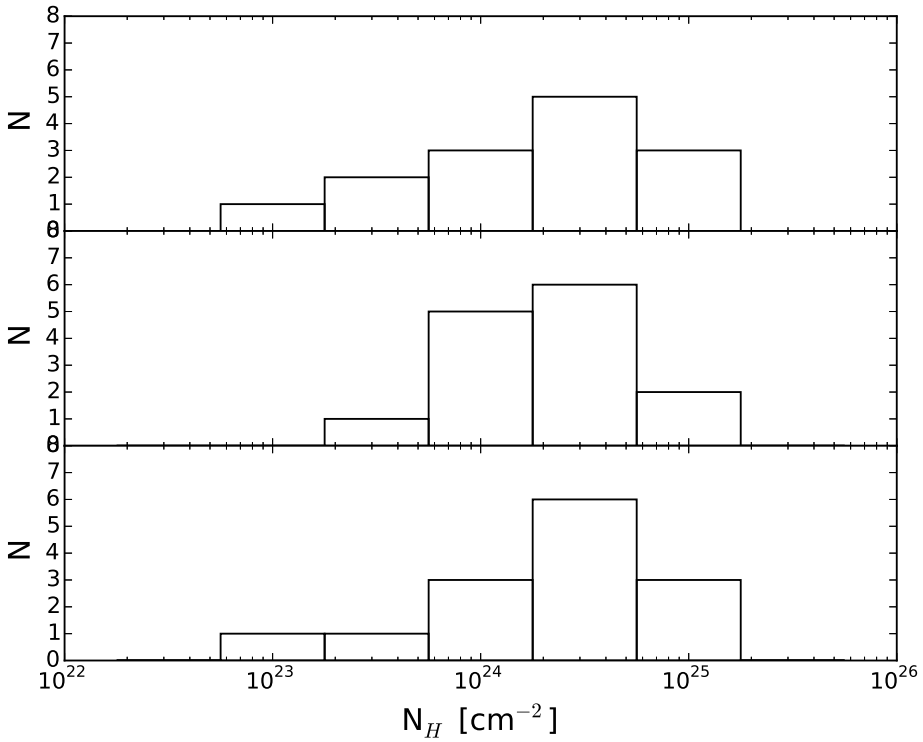

FIGURE 2.9: *Top panel*: distribution of $N_{\rm H}$ as measured by X-ray spectral fitting. *Middle panel*: distribution of column densities predicted by the model, using a power law density profile. *Bottom panel*: distribution of column densities predicted by the model, with mixed exponential density profile (see text).

the ones measured with X-ray spectral fitting (Figure 2.9, middle panel). Moreover, it turns out that between the tunable parameters of the model (the densities $\rho_{\rm in}$ and $\rho_{\rm out}$ at which the maser disk begins and ends, and $\rho^{\rm T}_{\rm out}$ at which the torus ends), results are only sensitive to the outer maser disk density, $\rho_{\rm out}$. This can be seen directly from Equation (2.5). In particular, changing $\rho_{\rm out}$ by one order of magnitude changes $N_{\rm H}$ by a factor ~ 14, while the same variation in $\rho_{\rm in}$ and $\rho^{\rm T}_{\rm out}$ has a negligible impact on the distribution (factor ~ 1.3 and ~ 1.01, respectively). In other words, a small change in the parameter $\rho_{\rm out}$ gives a large change in the recovered $N_{\rm H}$, and this is a hint that the theoretically driven choice of the three densities is the best at reproducing the observed column density distribution.

Another step forward can be made by testing the power law assumption for the density profile. The α parameter in fact only tells how fast the density falls inside the maser disk, decreasing by ~ 4 orders of magnitude in a fraction of a parsec. The resulting distribution of the α parameter is skewed and very steep, peaking at very high values (~ 8).

Clouds orbiting a SMBH at sub-parsec distances are often modeled with a radial dependence of the form $N(r) \sim r^{-q}$, where $N(r)$ is the number of clouds per unit length, and q is usually 1 or 2 (Nenkova et al., 2008b, e.g.,). This translates in a radial dependence of the number of clouds per unit volume of $\sim r^{-3q}$. If every cloud has approximately the same number of atoms and same chemical composition, the same radial trend holds also for the density ρ to which we refer here. In Figure 2.10 we show how our α indexes, which describe the density falling rate in a smooth medium, compare with the power law distributions of clouds in clumpy models. In Figure 2.10 we plot the ratio of the outer and inner maser radii as a function of X-ray (deabsorbed) luminosity in the $2-10$ keV band. There is no clear correlation between the two quantities. The ratios cluster roughly between the values 2 - 4. We also plot the ratios expected for different radial distributions with dashed lines of different colors, showing that q indexes of $2-3$ are preferred. One possibility for explaining this trend is that the density gradient between the inner and outer maser radii is lower than the assumed one (four orders of magnitude, from 10^{11} cm^{-3} at $R_{\rm in}$ to 10^{7} cm^{-3} at $R_{\rm out}$). For example, a decrease of three orders of magnitude (which is reasonable, assuming current uncertainties) would make the data fully consistent with a distribution of clouds with power law index $q = 2$. Another possibility is that in a real medium, which is probably a mixture of clumps, voids, and filaments, the density falls abruptly between clouds, steepening the α index. Also warps in maser disks could bias the inner and outer maser radii measurements. Taking the caveats and uncertainties described above into account, we conclude that our analytical formulas for the density are consistent with a radial distribution of clouds $N(r) \sim r^{-q}$, with $q \sim 2-3$.

An alternative modelization of our steep density profile is an exponential one:

$$\rho(r) = \rho_{\rm in} \exp\left[-\left(\frac{r - R_{\rm in}}{R_{\rm out} - R_{\rm in}}\right)^{1/n} \ln\left(\frac{\rho_{\rm in}}{\rho_{\rm out}}\right)\right], \tag{2.6}$$

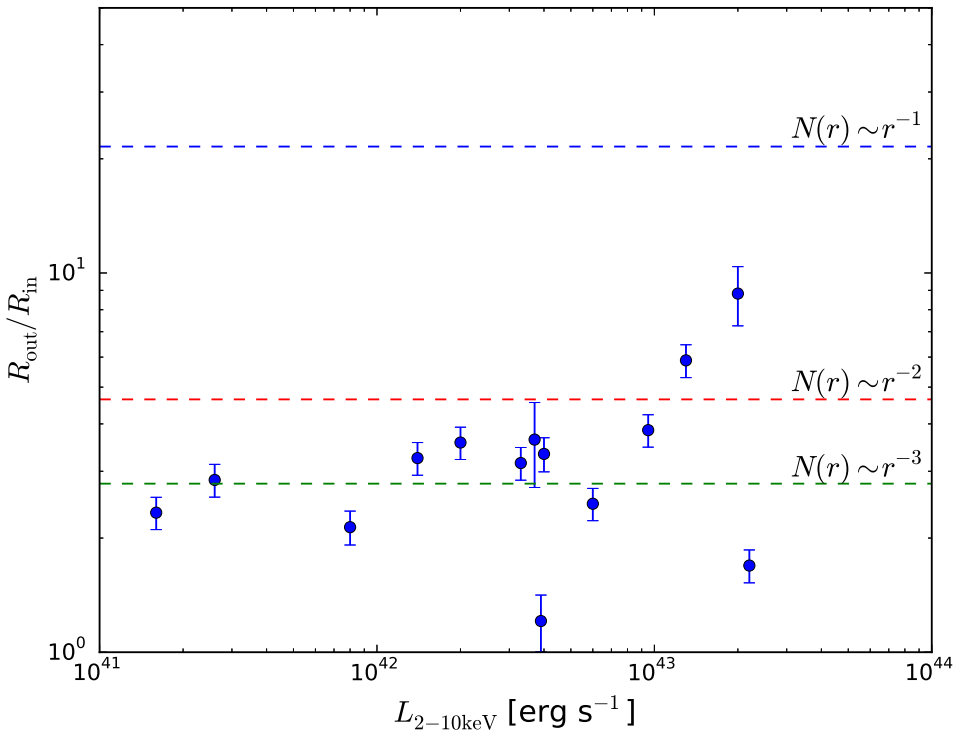

FIGURE 2.10: Ratio of outer and inner maser radii for the sources in the sample as a function of X-ray (deabsorbed) luminosity in the 2 – 10 keV band. The trend $N(r) \sim r^{-1}$ (blue dashed line) seems to be ruled out, while $N(r) \sim r^{-2}$ and $N(r) \sim r^{-3}$ (red and green dashed lines, respectively) are preferred. We note that the ratios expected for different clouds distributions depend on the critical maser densities assumed, being the expected ratio for a particular q, $R_{\rm out}/R_{\rm in} = 10^{\log(\rho_{\rm in}/\rho_{\rm out})/3q}$.

where n is the equivalent of the Sersic index. We note that the $n = 1$ and $n = 2$ cases are, in general, able to represent Compton-thin and Compton-thick sources, respectively. In other words, results similar to the power law case are found for a mixed density profile, different between Compton-thin and thick sources.

For each n, the torus outer radius and the column density can be calculated with

$$R_{\rm out}^{\rm T} = R_{\rm in} + (R_{\rm out} - R_{\rm in}) \left[\frac{\ln(\rho_{\rm out}^{\rm T}/\rho_{\rm in})}{\ln(\rho_{\rm out}/\rho_{\rm in})} \right]^n \tag{2.7}$$

$$N_{\rm H} = \frac{n(R_{\rm out} - R_{\rm in})}{[\ln(\rho_{\rm in}/\rho_{\rm out})]^n} \rho_{\rm in} \left[\Gamma\left(n, \ln\frac{\rho_{\rm in}}{\rho_{\rm out}}\right) - \Gamma\left(n, \ln\frac{\rho_{\rm in}}{\rho_{\rm out}^{\rm T}}\right) \right], \tag{2.8}$$

where $\Gamma(n,x)$ is the incomplete Gamma function, and $\Gamma(n,0) = \Gamma(n)$. In the specific cases $n = 1$ and $n = 2$, equation (2.8) becomes

$$N_{\rm H} = \begin{cases} \frac{(R_{\rm out}-R_{\rm in})}{\ln(\rho_{\rm in}/\rho_{\rm out})} \left(\rho_{\rm out} - \rho_{\rm out}^{\rm T}\right) & n = 1 \\ \frac{2(R_{\rm out}-R_{\rm in})}{[\ln(\rho_{\rm in}/\rho_{\rm out})]^2} \left\{ \rho_{\rm out} \left[\ln\left(\frac{\rho_{\rm in}}{\rho_{\rm out}}\right) + 1 \right] - \rho_{\rm out}^{\rm T} \left[\ln\left(\frac{\rho_{\rm in}}{\rho_{\rm out}^{\rm T}}\right) + 1 \right] \right\} & n = 2 \end{cases}. \tag{2.9}$$

We can then repeat the same analysis, using equations (2.7) and (2.9) to predict

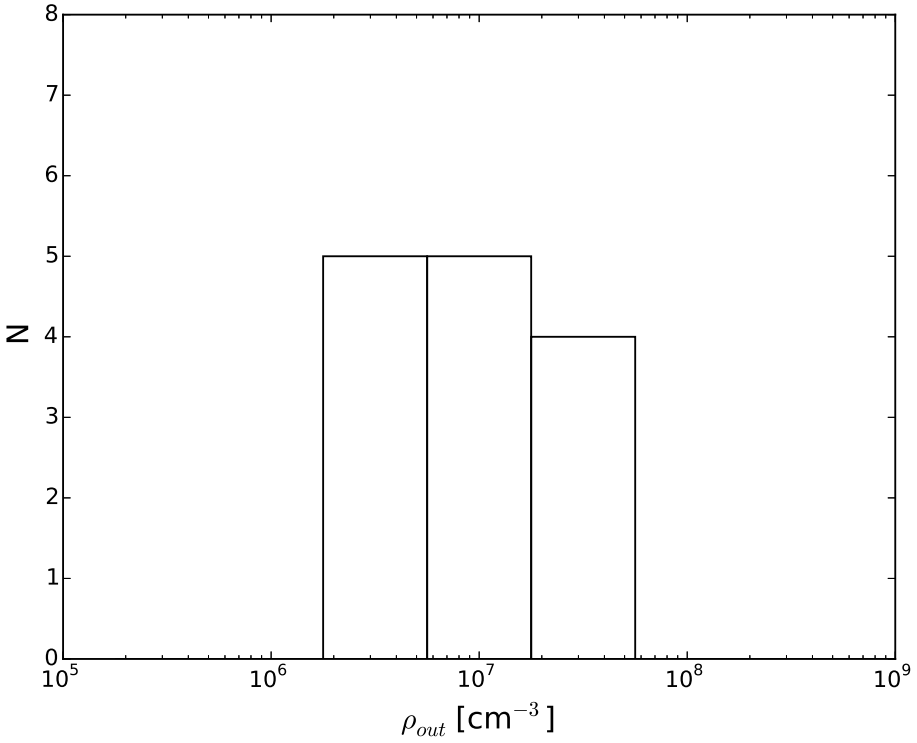

FIGURE 2.11: Distribution of the parameter $\rho_{\rm out}$ in the sample, calculated as described in §2.7.2. See also Table 2.4.

the column density distribution with fixed $\rho_{\rm out} = 10^7$ cm^{-3} (Figure 2.9, bottom panel): notably, the mixed exponential density profile (i.e. with $1 \leq n \leq 2$) can reproduce the observed distribution of X-ray measured column densities better than the power law general case.

2.7.2 The torus size

Instead of assuming the transition density $\rho_{\rm out}$ to infer $N_{\rm H}$, we now use the column densities measured by NuSTAR and reverse the problem. Inverting (2.9), one can calculate the parameter $\rho_{\rm out}$ needed to have a torus with a column density equal to the measured one. The result is that it is sufficient to have a sharp distribution of $\rho_{\rm out}$ peaked at 10^7 cm^{-3} to have tori with the measured column densities. In other words, fixing the inner maser density $\rho_{\rm in}$ and the outer torus density $\rho^{\rm T}_{\rm out}$ and using the measured column densities, the model points toward a transition density of about 10^7 cm^{-2}, without knowing anything of the previous theoretical assumptions.
Figure 2.11 shows the resulting $\rho_{\rm out}$ distribution (see Table 2.4 for numerical values), while Figure 2.12 shows the torus outer radius distribution obtained using equation (2.7) (numerical values are reported in Table 2.4).

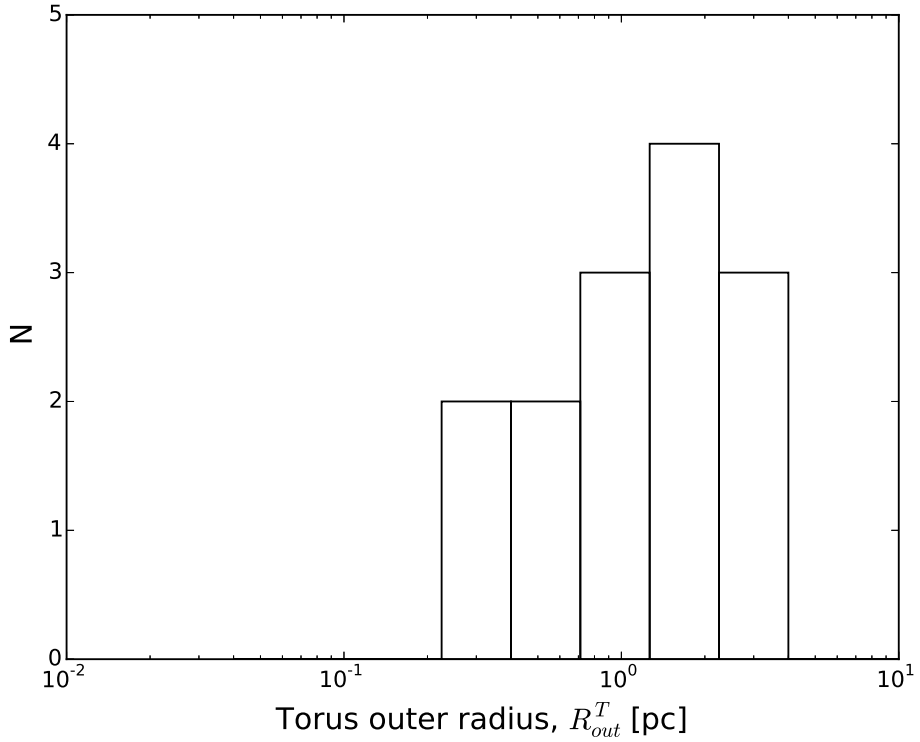

FIGURE 2.12: Distribution of torus outer radius predicted by the model, calculated as described in §2.7.2. See also Table 2.4.

TABLE 2.4: $\rho_{\rm out}$ values needed to have $N_{\rm H,meas} = N_{\rm H,pred}$ with the assumption of maser disk-torus density profile continuity, and output of the model, the torus outer radius.

Name	$\rho_{\rm out}$ [cm^{-3}]	$R_{\rm out}^{\rm T}$ [pc]
NGC 1194	2.8×10^6	2.4 ± 0.2
NGC 1386	1.3×10^7	2.1 ± 0.3
NGC 2273	4.8×10^7	$0.77^{+\infty}_{-0.07}$
NGC 2960	6.5×10^6	$0.53^{+0.06}_{-0.05}$
NGC 3079	4.1×10^6	2.7 ± 0.2
NGC 3393	2.6×10^6	3.3 ± 0.5
NGC 4388	2.4×10^7	0.34 ± 0.07
IC 2560	3.1×10^7	$1.1^{+\infty}_{-0.1}$
NGC 1068	1.6×10^7	$2.2^{+\infty}_{-0.3}$
NGC 4945	1.6×10^7	1.1 ± 0.1
Circinus	3.4×10^7	1.3 ± 0.3
NGC 4258	1.9×10^6	0.36 ± 0.03
NGC 6264	2.8×10^6	$1.6^{+\infty}_{-0.2}$
UGC 3789	6.6×10^6	$0.69^{+\infty}_{-0.06}$

2.8 Discussion

2.8.1 Comparison with mid-infrared interferometry

Our toy model allows us to predict the X-ray column density distribution of a sample of disk maser systems or to calculate the torus outer radius if the column density is known. When dealing with very high column densities (i.e., lower limits on $N_{\rm H}$), the torus outer radius is poorly constrained, since the measured column density can be ascribed to the maser disk without the need of an inflated torus. However, it is interesting to compare our results with mid-infrared (MIR) measurements, which are thought to probe the dusty structure surrounding AGN. In our sample, only NGC 1068 (Raban et al., 2009; López-Gonzaga et al., 2014) and Circinus (Tristram et al., 2007; Tristram et al., 2014) have been observed with MIR interferometry. In both sources two distinct structures responsible for the MIR emission are detected. One is an elongated, disk-like structure, which is co-aligned and co-spatial with the maser emission spots and perpendicular to the ionization cones (albeit with the caveat of uncertainty in the absolute astrometry). The second structure, whose origin and theoretical explanation is still unclear, seems to be responsible for diffuse emission on much larger scales (> 1 pc), broadly perpendicular to the first. The geometry of this double dusty structure is currently challenging the classical torus framework. In Figure 2.13a we show the image in the MIR band obtained by Tristram et al. (2014), and a sketch of the theoretical model invoked to explain such observations in Figure 2.13b. These two-component structures are not considered in our simple toy model; however, we note that the sizes are in broad agreement with our predictions, being parsec scales. Another possibility of comparison comes from considering half-light radii ($r_{1/2}$), enclosing half of the MIR flux of the source, as done in Burtscher et al. (2013). We note that the NGC 1068 and Circinus outer radii are less than a factor of two larger than the $r_{1/2}$ values reported by Burtscher et al. (2013). This could be expected, since the outer torus radius should be larger than the half-light one. Moreover, the $r_{1/2}$ of NGC 1068 is broadly twice the $r_{1/2}$ of Circinus; the same happens with $R^{\rm T}_{\rm out}$ in our toy model. Future observations in the MIR band of other sources are needed to probe this scenario.

2.8.2 Trend with bolometric luminosity

Burtscher et al. (2013) found a clear positive trend of the half-light radius (used as a proxy for the torus size) with the bolometric luminosity, although with large scatter (their Figure 36). In the near-infrared (NIR), a scaling of the dust sublimation radius with $L^{1/2}_{\rm bol}$ is well known. However, this relation is much more scattered in the MIR: more luminous sources generally have larger tori with no clear trend. We can then explore whether a relation between the bolometric luminosity and the torus size holds in our toy model. We take $L_{\rm bol} = k_{\rm bol} \times L^{\rm int}_{2-10}$, where $k_{\rm bol} = 20 \pm 5$ is the bolometric correction, which is constant in our range of intrinsic $2-10$ keV luminosities (Steffen et al.,

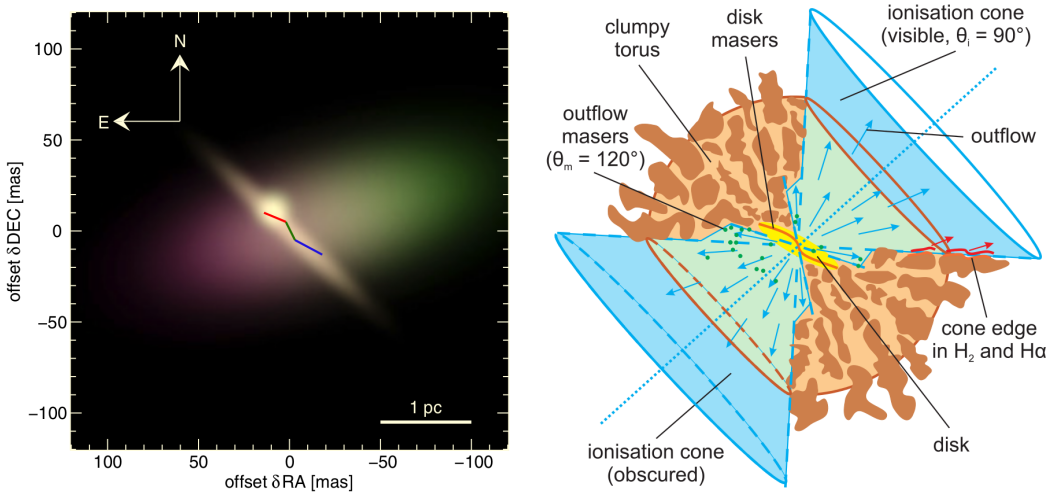

(A) (B)

FIGURE 2.13: **(A).** False-color image of the three-component model for the MIR emission of the nucleus of the Circinus galaxy. Despite the lower surface brightness, 80% of the emission comes from the extended component. Also plotted is the trace of the water maser disk: the blue and red arms trace the approaching and receding sides of the maser disk, respectively. Note that the relative offset of the MIR emission with respect to the maser disk is not known.Figure adapted from Tristram et al. (2014). **(B).** Model of Circinus torus, proposed by Tristram et al. (2007) when the first interferometric data became available. The dominant polar component may be due to an outflowing wind illuminating dust on the foreground. Figure adapted from Tristram et al. (2007).

2006; Lusso et al., 2012). We choose a 25% uncertainty on $k_{\rm bol}$ to also include a reasonable error on the 2 – 10 keV intrinsic luminosity derived from NuSTAR spectral fitting, and we note that using a non-constant bolometric correction would steepen the correlations. We fit our sample with a linear relation of the form $\log y = a(\log L_{\rm bol} - 43.5) + b \pm S$, where $L_{\rm bol}$ is measured in erg s^{-1} and S represents the intrinsic scatter in the relation. We applied a Bayesian analysis with loose priors (uniform for all the unknown parameters, i.e., the slope, the intercept, and the intrinsic scatter). Since our tori are an extension of the maser disks, we first explored the possibility of a correlation between the inner and outer maser radii with bolometric luminosity. Results are shown in the top and middle panels of Figure 2.14. Finally, we repeated the same procedure for the torus outer radius, which is a derived quantity (Figure 2.14, bottom panel - refer to Table 2.5 for best fit parameters in all three cases). We find an interesting evolution of the trend, going from the absence of a correlation between the inner maser radius and the bolometric luminosity to a positive correlation between the torus outer radius and luminosity, although with large intrinsic scatter. The slopes are, however, all consistent within the uncertainties.

The weak trend of the torus's outer radius with luminosity could also reflect the weak correlation between maser disks dimensions with luminosity already noted by Greenhill et al. (2003) comparing NGC 4258 and Circinus inner maser radii. We have here

TABLE 2.5: $R_{\rm in} - L_{\rm bol}$, $R_{\rm out} - L_{\rm bol}$, and $R^{\rm T}_{\rm out} - L_{\rm bol}$ relations: best fit parameters. Errors quoted are 1σ confidence level.

Parameter	$R_{\rm in} - L_{\rm bol}$	$R_{\rm out} - L_{\rm bol}$	$R^{\rm T}_{\rm out} - L_{\rm bol}$
a	$0.02^{+0.16}_{-0.17}$	$0.12^{+0.14}_{-0.14}$	$0.30^{+0.13}_{-0.13}$
b (at $\log L_{\rm bol}/{\rm erg\ s^{-1}} = 43.5$)	$-0.75^{+0.12}_{-0.12}$	$-0.29^{+0.09}_{-0.10}$	$0.04^{+0.09}_{-0.09}$
S [dex]	$0.42^{+0.09}_{-0.09}$	$0.34^{+0.07}_{-0.07}$	$0.30^{+0.07}_{-0.07}$

confirmed that finding with an enlarged sample. As already suggested by Greenhill et al. (2003), warps in maser disks could break the edge-on geometry condition and bias the disk radial extent measurements.

2.8.3 The possible role of warps

Warped disks have been observed in some sources of the sample. (Circinus and NGC 4258 are the clearest cases, see Greenhill et al., 2003; Wu, Yan, and Yi, 2013, and references therein.) Low covering factor and/or fast $N_{\rm H}$ variability (as in the case of NGC 4945, see, e.g., Madejski et al., 2000; Puccetti et al., 2014) could indicate the maser disk as the obscuring structure, instead of invoking an inflated torus. It is easy to see that, when keeping the densities expected by the astrophysical maser theory, only a small fraction of the disk is required to intercept the line of sight to have the measured column density (see Figure 2.15). To calculate the radial extent of such a warp, we define $R_{\rm w}$ as the warping radius and assume that the warp extends up to the maser outer radius, $R_{\rm out}$. To calculate $R_{\rm w}$, it is sufficient to replace $\rho_{\rm out}$ with $\rho_{\rm w}$ and $\rho^{\rm T}_{\rm out}$ with $\rho_{\rm out}$ in Eqs. (2.7) and (2.9), if adopting an exponential density profile. If using a power law density profile, results are the same within the uncertainties.
In a picture in which there is no standard torus, but only a nearly edge-on molecular disk, a warp of depth $\Delta R_{\rm w} = R_{\rm out} - R_{\rm w}$ is required to obscure the central engine. Numerical values for $\Delta R_{\rm w}$ can be found in Table 2.6.

2.9 Megamaser disks as probes of AGN accretion

Thanks to NuSTAR, high-quality intrinsic X-ray luminosities and column densities have been obtained for the megamasers sample. Combining the state-of-the-art hard X-ray information, with the golden estimates of megamasers SMBHs masses and precise VLBI measurements, deeper insights into the physics of AGN can be obtained.

2.9.1 The $\Gamma - \lambda_{\rm Edd}$ relation

A relation between the photon index Γ of the AGN power law and the Eddington ratio $\lambda_{\rm Edd}$ is well-known, and has been studied and calibrated for unobscured AGN (i.e. Seyfert 1 galaxies, see Brightman et al., 2013). The high quality hard X-ray spectra from NuSTAR and the precise measurements of the SMBH mass coming from disk

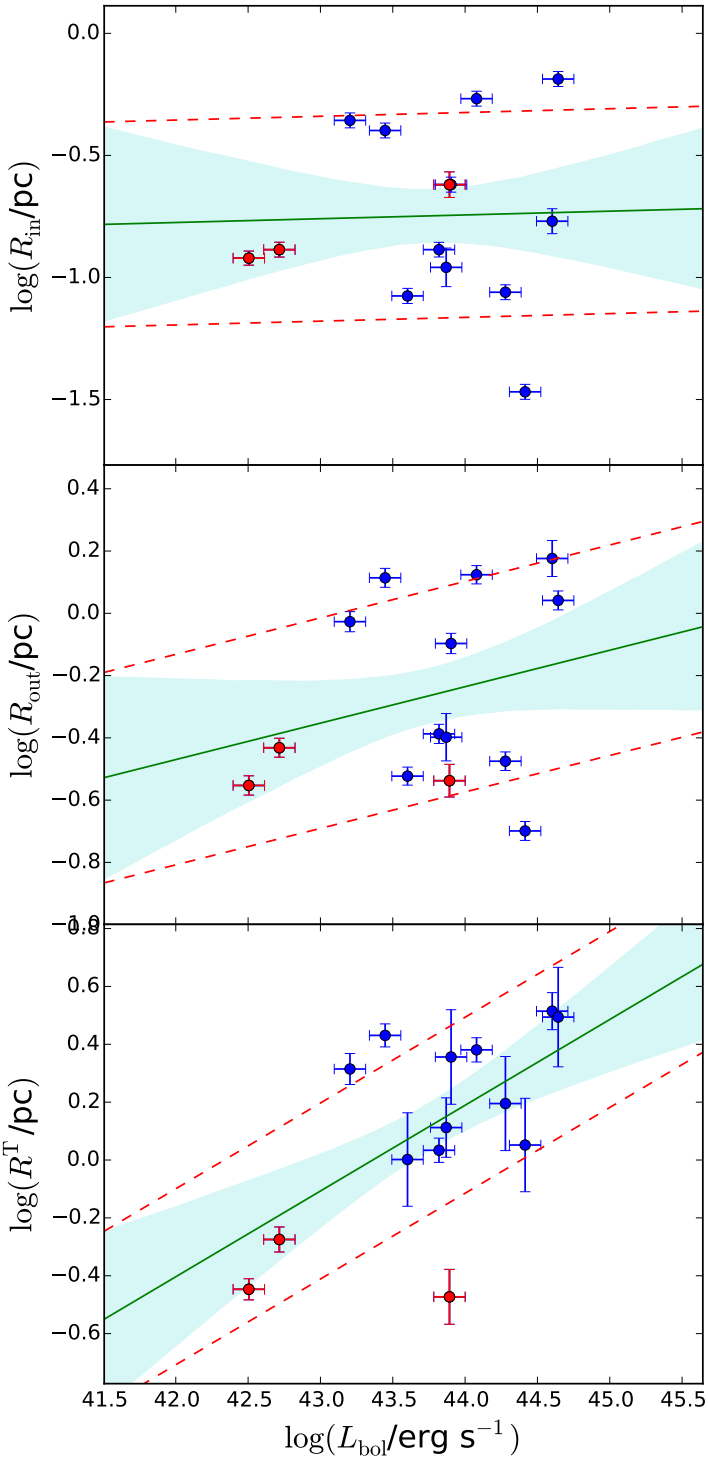

FIGURE 2.14: Size-luminosity relations, with progression from an absence of correlation (top) to a possible one (bottom). Maser disk inner (top), outer (middle) and torus outer (bottom) radius as a function of bolometric luminosity, $L_{\rm bol}$. The three Compton-thin sources are indicated by red points. The green line is the best fit linear model, the red dashed lines show the intrinsic scatter of the data, and the cyan shaded area indicates the uncertainty of the model.

TABLE 2.6: ΔR_w values needed to have $N_{H,meas} = N_{H,pred}$ with the assumption of all obscuration due to a warp of the maser disk entering the line of sight. Uncertainties are neglected for clarity. Warp depths are lower than, or comparable to, the uncertainties on outer maser radii. The five sources with a lower limit on the column density consequently have a lower limit on the warp depth.

Name	R_w [pc]	ΔR_w [pc]
NGC 1194	1.29	0.04
NGC 1386	0.84	0.09
NGC 2273	< 0.13	> 0.07
NGC 2960	0.36	0.01
NGC 3079	1.23	0.07
NGC 3393	1.44	0.06
NGC 4388	0.283	0.007
IC 2560	< 0.25	> 0.08
NGC 1068	< 1.0	> 0.1
NGC 4945	0.35	0.06
Circinus	0.3	0.1
NGC 4258	0.277	0.003
NGC 6264	< 0.77	> 0.03
UGC 3789	< 0.28	> 0.02

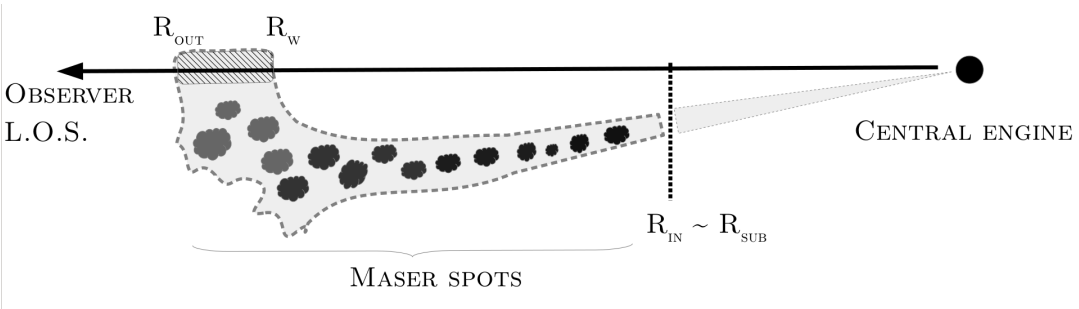

FIGURE 2.15: Possible role of warps: rapid N_H variability and low covering factor. The obscuring column is provided by a warp of depth $\Delta R_w = R_{out} - R_w$. The thick arrow denotes the observer line of sight.

megamasers can be combined in order to obtain as precise as possible Eddington ratios. Our disk megamasers represents a golden sample to explore such relation, in a so far unexplored obscuration state, and even for Compton-thick sources, where reliable intrinsic luminosities are more difficult to obtain. In Brightman et al. (2016), we investigated if highly obscured AGN follow the same relation found for unobscured AGN. The result can be seen in Figure 2.16, where the solid black line and the dotted curves show the best fitting linear relation to the data (red and orange squares) and its uncertainty. The dashed black line, on the other hand, marks the linear relation measured for unobscured AGN by Brightman et al. (2013).

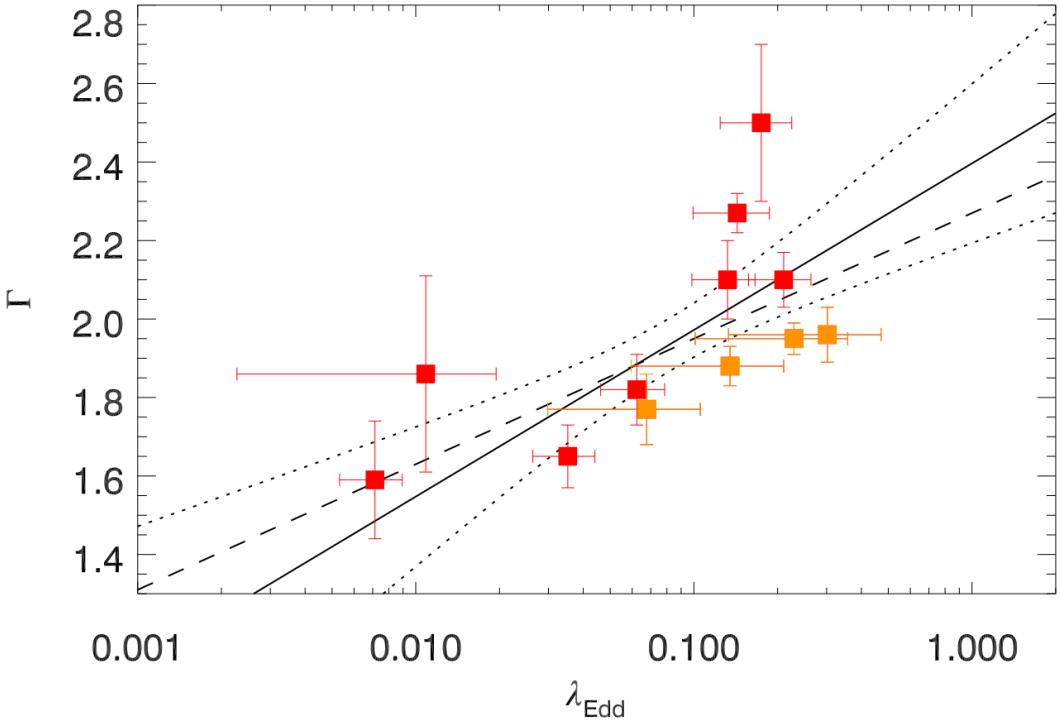

FIGURE 2.16: $\Gamma - \lambda_{\rm Edd}$ relation for CT AGN. Red squares mark the best-quality sources in Masini et al. (2016), while the orange points mark the different observed states in NGC4945 by Puccetti et al. (2014). The solid black line and the dotted curves show the best fitting linear relation to the data and its uncertainty. The dashed black line, on the other hand, marks the linear relation measured for unobscured AGN by Brightman et al. (2013). Figure adapted from Brightman et al. (2016).

The two relations are then consistent within the uncertainties, and we can conclude that the $\Gamma - \lambda_{\rm Edd}$ relation holds even for heavily obscured AGN. This result gives support to the unification model of AGN, implying that heavily obscured AGN (at least locally; the megamasers in our sample are all lying at $z < 0.03$) have the same properties of unobscured AGN, and confirms that the toroidal models adopted in the X-ray spectroscopy are able to correct for heavy absorption in recovering the intrinsic photon index Γ. This is also surprising, since such models often assume a smooth distribution of gas, while the well-known clumpiness of the torus is addressed in other models

(Nenkova et al., 2008a; Nenkova et al., 2008b, e.g.,), mainly used to analyze the IR part of the AGN SEDs.
Once better calibrated, this relation could help in determining the Eddington ratio (and the growth rate) of the most heavily obscured AGN, without measuring the BH mass and using only the measurement of the X-ray photon index. However, to date the very presence of a correlation is challenged by the large scatter observed by the *Swift*-BAT spectroscopic survey of local AGN (BASS; see Trakhtenbrot et al., 2017).

2.9.2 The $k_{\rm Bol}$ of CT AGN

The SED fitting method is an alternative way to get the bolometric luminosity of an AGN, once the galaxy and AGN contributions are separated. In this way, one can estimate the bolometric luminosity of a sample of AGN and compare it with the luminosity computed from the X-ray spectroscopy. The ratio between the bolometric luminosity and the X-ray one gives the X-ray bolometric correction factor $k_{\rm bol}$, which is known to be luminosity-dependent but often assumed to be constant for a defined range of luminosities (Lusso et al., 2012). Thanks to the high quality data obtained from NuSTAR for the megamasers, Brightman et al. (2017) investigated the bolometric correction factor in a so far unexplored obscuration regime, the CT one. After comparing smooth and clumpy torus models, the results suggest that the bolometric correction is stable over five orders of magnitude in column density (see Figure 2.17), once samples with different obscuration are matched in $L_{\rm bol}$.

2.10 Summary of this Chapter

In the first part of this Chapter, we presented hard X-ray spectral analyses of NuSTAR data for eight sources out of a sample of 14 nearby disk megamaser galaxies with the aim of exploring the relationship between the maser disk and the environment in which it resides. In our final sample of 14 AGN, $\sim 80\%$ are Compton-thick, and $\sim 20\%$ are Compton-thin. All these objects are indeed obscured Sy2 galaxies, and show 22 GHz maser emission from water vapor molecules in a dense molecular disk around active SMBHs. We proposed a toy model to explain this connection, where the maser disk is the inner part of the torus, ending in an inflated, geometrically thicker structure. Even if the model is simplistic, it is able to recover the column density distribution for a sample of obscured, disk megamaser AGN, using reasonable density profiles (a power law or, better, an exponential with $1 \leq n \leq 2$). Alternatively, one can start from the measured $R_{\rm in}$, $R_{\rm out}$, and $N_{\rm H}$, assume a reasonable density profile, solve the equations for the crucial parameter $\rho_{\rm out}$, and estimate the torus outer radius, which is found to be on the parsec scale. A direct and robust measure of the torus size is available in two sources (NGC 1068 and Circinus) through mid-IR interferometry. In both cases, the outcomes of the model agree with the half-light radius or single resolved structure size measurements. Clearly, a more physical picture explicitly addressing the known disk/torus clumpiness and warping must rely on numerical calculations.

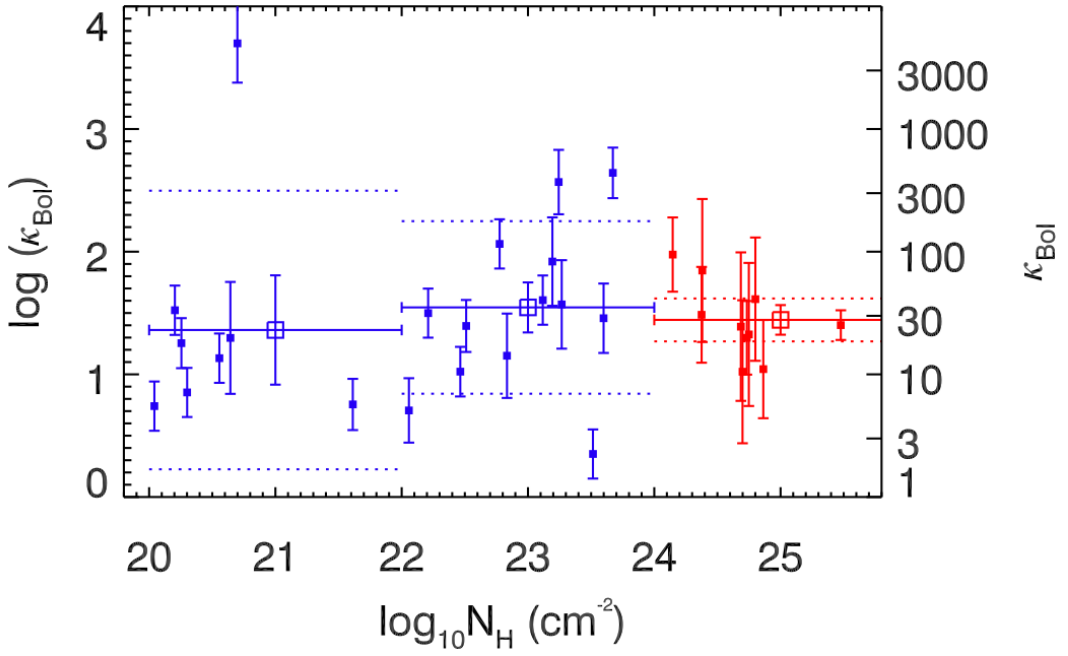

FIGURE 2.17: X-ray bolometric correction as a function of column density N_H. Our CT AGN sample (small filled red squares) is compared to other samples of unobscured and Compton-thin AGNs from Gruppioni et al. (2016) and Brightman and Nandra (2011, small filled blue squares), selected to have the same range of L_{bol} as our sample. The large empty squares represent the means of these data points for three bins in N_H, and the dotted lines mark the estimated σ of the intrinsic scatter. Figure adapted from Brightman et al. (2017).

When we assume a geometry like the one proposed in Figure 2.8b, the column density derived with X-ray spectroscopy is due to the inflated end of the clumpy torus alone. Indeed, in ten sources of our sample, $N_H < 10^{25}$ cm^{-2}. This obscuration can be explained if the line of sight does not intercept the masing disk. In the remaining five sources, the column density is compatible with that of the maser disk, which is very optically thick in this framework (i.e., $N_H \gtrsim 10^{26}$ cm^{-2}): these sources could be those seen exactly edge-on, with the line of sight intercepting the geometrically thin maser disk along the equatorial plane. We note, however, that NGC 6264 and UGC 3789 currently lack NuSTAR spectra, and their column density has been estimated using XMM-*Newton* (Castangia et al., 2013). Future NuSTAR observations may shed light on the exact value of the column density of these two sources, further constraining the fraction of heavily ($N_H > 10^{25}$ cm^{-2}) Compton-thick AGN in our sample. We also found no correlation between the size of the maser disk and the bolometric luminosity of the AGN, derived correcting the absorption-corrected X-ray one with a proper bolometric correction. This lack of correlation has been confirmed by later work (Gao et al., 2016). On the other hand, a possible correlation with the outer end of the torus is suggested. We also discussed the possibility that, in some cases, warps in the maser disk may play the role of the classical torus in the AGN unified model, providing low covering factor

and fast column density variability.
In the last part of the Chapter, we presented two applications of our measurements combining results coming from NuSTAR with the high-quality SMBH masses provided by the maser spots dynamics. We confirmed that the photon index correlates with the Eddington ratio in CT AGN, following the same relation found for unobscured sources, and also that the X-ray bolometric correction is not depending on column density.

Chapter 3

Variability and Compton-thickness: the NuSTAR perspective

After discussing how NuSTAR can help in studying and understanding the physics of heavily obscured AGN, this Chapter follows on the megamasers project and focuses on X-ray variability, being in particular devoted to column density changes on different timescales. A full understanding of the variability phenomenon in AGN is still missing, being band-dependent, timescale-dependent, and physics-dependent. The task of finding and studying Compton-thick AGN is then made harder by their variable obscuration state. In this Chapter, the NuSTAR view of variable obscured AGN is presented through a bunch of case-studies of local, well-known Seyfert 2 AGN. In particular, the peculiar case of NGC7674, a variable CT AGN with a weak iron line, will link the study of local megamasers to the outstanding search of CT AGN in deep surveys, on which the next Chapter will focus. This Chapter is mainly based on: *"The Phoenix Galaxy as seen by NuSTAR"*; Masini, A., Comastri, A., Puccetti, S., Baloković, M., et al.; 2017; A&A; 597, A100.

3.1 Variability and "Changing look" AGN

X-ray variability is a well-known property of active galactic nuclei (AGN). In recent years, many studies have focused on its characterization, and a class of extremely variable sources was found. Sources showing a transition between Compton-thin (i.e. with an obscuring column density of $10^{22} < N_{\rm H} < 10^{24}$ cm^{-2}) and Compton-thick levels of obscuration ($N_{\rm H} > 10^{24}$ cm^{-2}) are called "changing-look AGN", and are important in assessing the relevance and physics of variability. The most famous cases are NGC 1365 (Risaliti et al., 2005; Walton et al., 2014; Rivers et al., 2015b), NGC 6300 (Guainazzi, 2002), NGC 2992 (Gilli et al., 2000) , NGC 7674 (Bianchi et al., 2005; Gandhi et al., 2017), and NGC 7582 (Piconcelli et al., 2007; Rivers et al., 2015a). The nature of X-ray variability could be explained in different ways. A drop in flux can either be due to intrinsic fading of the central engine since we do not expect the accretion of matter

on supermassive black holes (SMBHs) to be constant in time, or to an eclipsing phenomenon caused by some clumpy material absorbing the radiation along the line of sight (l.o.s.). A significant change in the spectral shape with a constant flux can also occur, implying some changing of one intrinsic property of the central source (e.g., the coronal temperature).
In order to adequately study this complex property of AGN, monitoring sources on a wide range of timescales from weeks to years is needed, ideally with high sensitivity in the hard X-ray band (> 10 keV), which more directly probes the primary emission from the innermost regions of the AGN.
In this Chapter, we present some NuSTAR-specific case studies of local obscured sources, focused on their variability properties. The obscuration state of a given source can change significantly on a wide range of timescales, challenging the CT fraction estimates in deep surveys. Understanding the variability of local CT sources sheds light on its relevance in the more distant Universe.

3.2 Mrk1210: a case study

Also known as UGC 4203, Mrk 1210 (z = 0.0135, Figure 3.1) hosts a Seyfert 2 AGN which was initially observed by *ASCA* in 1995 (Awaki et al., 2000). The flat spectrum and high equivalent width (EW) of the iron line at 6.4 keV were interpreted as emerging from reflection off circumnuclear matter of the AGN primary X-ray continuum, severely suppressed by Compton-thick absorption. In 2001, an XMM-*Newton* observation (Guainazzi et al., 2002) found that Mrk 1210, six years after the first observation, was still obscured but at the Compton-thin level only. Interpreting the change as an intrinsic flux enhancement, they coined the name "Phoenix galaxy" for this new changing-look AGN. Also Ohno, Fukazawa, and Iyomoto (2004), in the same year, observed Mrk 1210 with *BeppoSAX* and found similar results. Later on, the Phoenix galaxy was observed by other instruments, always showing variability of less than a factor of two in both intrinsic emission and column density, with the latter always in the Compton-thin regime (Matt et al., 2009; Risaliti et al., 2010). The list of all X-ray observations is presented in Table 3.1.

TABLE 3.1: History of X-ray observations of Mrk 1210.

Instrument	Date of observation(s)
ASCA	1995-Oct-18, 1995-Nov-12
XMM-*Newton*	2001-May-5
BeppoSAX	2001-May-5
Chandra	2004-Mar-4
Swift	2006-Oct-6...2008-Apr-29 (four times)
Suzaku	2007-May-2
Chandra	2008-Jan-15...2008-Feb-06 (five times)
NuSTAR	2012-Oct-5

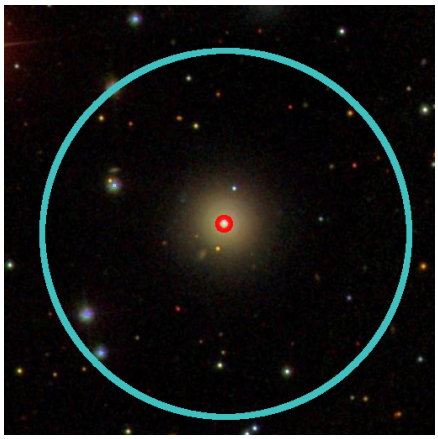

FIGURE 3.1: Sloan Digital Sky Survey (SDSS) optical image of Mrk 1210 (gri composite). The cyan and red circles are the source extraction regions for the NuSTAR (see §3.2.1) and *Chandra* (see Appendix A) spectra, respectively.

While the source has been extensively studied for the past twenty years, the reason for the changes observed between 1995 and 2001 remains unclear. A definitive answer is not yet available; however, as time went by, a change in $N_{\rm H}$ obscuring the nucleus was progressively addressed as the principal effect causing the change in flux. A better understanding of this source can be achieved thanks to NuSTAR.

3.2.1 Data reduction

NuSTAR observed Mrk 1210 on October 5, 2012 for 15.4 ks. The raw event file was processed using the NuSTAR Data Analysis Software package v. 1.5.1 (NuSTARDAS)[1]. Calibrated and cleaned event files were produced using the calibration files in the NuSTAR CALDB (20150316) and standard filtering criteria with the `nupipeline` task. We used the `nuproducts` task included in the NuSTARDAS package to extract the NuSTAR source and background spectra using the appropriate response and ancillary files. We extracted the source spectrum and light curve in both focal plane modules, FPMA and FPMB, using 87"-radius circular apertures, while the background was extracted using three source-free circular regions on the same chip as the source. All spectra were binned to a minimum of 20 photons per bin using the HEAsoft task `grppha`.

3.2.2 Spectral analysis

We used the XSPEC software version 12.9.0 (Arnaud, 1996) to carry out the spectral analysis. The source is clearly detected by NuSTAR up to $\sim$ 60 keV (Figure 3.2a), with a net count rate of 0.3894 ± 0.0052 cts s^{-1} and 0.3762 ± 0.0052 cts s^{-1} for FPMA and FPMB, respectively. During the observation, the source kept a nearly constant flux, with amplitude variations of less than 30% and no systematic trend, as shown in Figure 3.2b.

[1] `http://heasarc.gsfc.nasa.gov/docs/nustar/analysis/nustar_swguide.pdf`

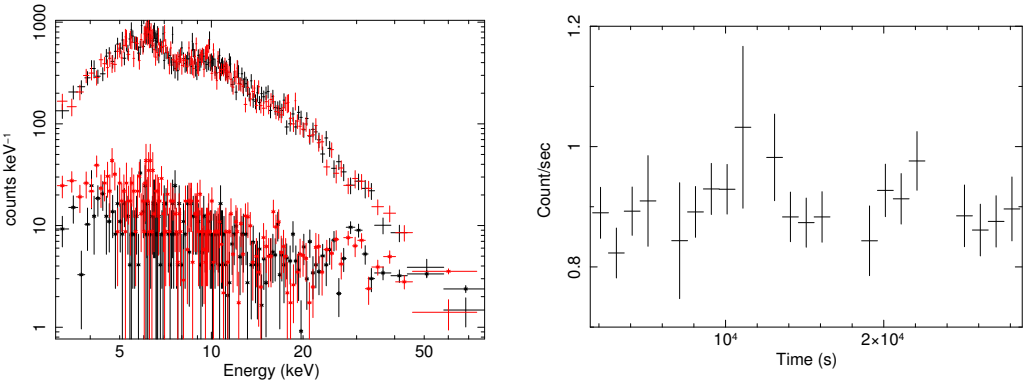

FIGURE 3.2: **(A).** NuSTAR background-subtracted spectrum of Mrk 1210 (FPMA in black, FPMB in red). The background is shown by diamonds, and is lower than the source signal up to ~ 50 keV. Both have been rebinned for plotting clarity. **(B).** 3 – 79 keV lightcurve of Mrk 1210. The background-subtracted FPMA and FPMB lightcurves were summed.

We included in all our fits a Galactic column density $N_{\rm H,gal} = 3.45 \times 10^{20}$ cm^{-2} (Kalberla et al., 2005). In the following spectral analysis, we follow the same approach explained in detail in §2.1.

Phenomenological models

Since we know from previous work that a simple Galactic-absorbed power law is not able to reproduce the spectral complexity of Mrk 1210, we began fitting its spectrum with a `plcabs` model; a power law with an high-energy ($\gtrsim$ 100 keV) exponential cut-off, taking into account Compton scattering and absorption at the source (Yaqoob, 1997). We also added a narrow (σ = 10 eV, fixed) Gaussian line component to fit the clearly visible feature at ~ 6 keV. The fit was good (χ^2/ν = 537/480), with a photon index $\Gamma = 1.40 \pm 0.05$ and an obscuring column of gas along the l.o.s. of $N_{\rm H} = (1.7 \pm 0.2) \times 10^{23}$ cm^{-2}. From previous studies, an additional soft component in the X-ray spectrum of the Phoenix galaxy is known (e.g., Guainazzi et al., 2002). Since this component can contribute between 3 and ~ 5 keV in the NuSTAR band, we modeled it adding another power law, and linking all the parameters (photon index, redshift, normalization) to those of the `plcabs` component. We then allowed for a constant multiplicative value (referred to as $f_{\rm s}$) to vary in the fit, which represents the fraction of the X-ray continuum Thomson-scattered into the soft X-rays. This procedure is often employed in the literature, and fractions of a few percent are typical (Bianchi and Guainazzi, 2007). Adding such a scattered power law (SPL) improved the fit (χ^2/ν = 521/479) at more than a 99% confidence limit, based on an F-test.

Although the fit was already acceptable, we wanted to test if any reflection component was required by the data. We therefore added a `pexrav` model (Magdziarz and Zdziarski, 1995), which includes Compton reflection on a slab of neutral material with

infinite optical depth. The final model in XSPEC notation is the following:

$$\begin{aligned} \text{BASELINE} = \overbrace{\text{constant}}^{\text{cross-normalization}} \times \overbrace{\text{phabs}}^{\text{Gal. absorption}} \times \\ \times (\overbrace{\text{plcabs} + \text{pexrav} + \text{zgauss}}^{\text{nuclear emission}} + \\ + \underbrace{f_s \times \text{zpowerlw}}_{\text{soft component (SPL)}}). \end{aligned} \tag{3.1}$$

We will refer to this as the 'baseline' model. The fit improved dramatically (χ^2/ν = 478/478, $\Delta\chi^2 = 43$, see Figure 3.3a): the source had a photon index closer to the average of AGN, $\Gamma = 1.9 \pm 0.1$, a column density $N_H = 3.0^{+0.7}_{-0.6} \times 10^{23}$ cm^{-2}, a reflection parameter $R = 2.5^{+1.2}_{-0.9}$ (intended as the ratio of the `pexrav` normalization and the `plcabs` one; moreover, a reflection parameter $R = 1$ implies a 2π coverage of the sky seen from the SMBH) and a fraction of the primary power law scattered in the soft part of the spectrum of 8^{+5}_{-6}%, which is higher than the average of Seyfert 2 galaxies, but not unusual (Bianchi and Guainazzi, 2007). This latter component, however, is now only significant at the 97% confidence limit, due to the high level of reflection. Upon removing it, the fit becomes slightly worse (χ^2/ν = 483/479), but the parameters are the same within the uncertainties.

We also note that the best fit line energy is lower than the iron Kα 6.4 keV centroid, although consistent with it at a 99% confidence limit (Figure 3.3b). Using previous versions of the NuSTARDAS software (v 1.2.1) and NuSTAR CALDB (20130909), and applying the same baseline model, we find that all the fit parameters are the same within the uncertainties, with a centroid line energy of 6.35 ± 0.06 keV, which is now consistent with the expected value of 6.4 keV at a 90% confidence limit. Moreover, as we shall see in the following subsections, we get good fits for the line feature adopting both toroidal models, in which the energy line is fixed to 6.4 keV, and a Compton shoulder is self-consistently calculated. Finally, since none of the previous observations found such a significant line energy shift, data with an improved spectral resolution would be needed to assess the relevance of the one found here.

Toroidal models

The high reflection value obtained by applying the baseline model implies a more complicated geometry or some time delay between the components; at the same time, a reflection component alone is not able to successfully fit the spectrum ($\chi^2/\nu = 609/481$). Therefore, we explored more physically motivated models which can take into account both absorption and reflection in a self-consistent way.

To this aim, we tried the `Torus` model (Brightman and Nandra, 2011) and the `MYTorus` model (Murphy and Yaqoob, 2009), a description of which can be found in §2.1.2.

We first applied the `Torus` model to the data, fixing the inclination angle of the torus (i.e., the parameter θ_{inc}; $\theta_{inc} = 0$ describes a face-on view) to 87°. The fit was acceptable

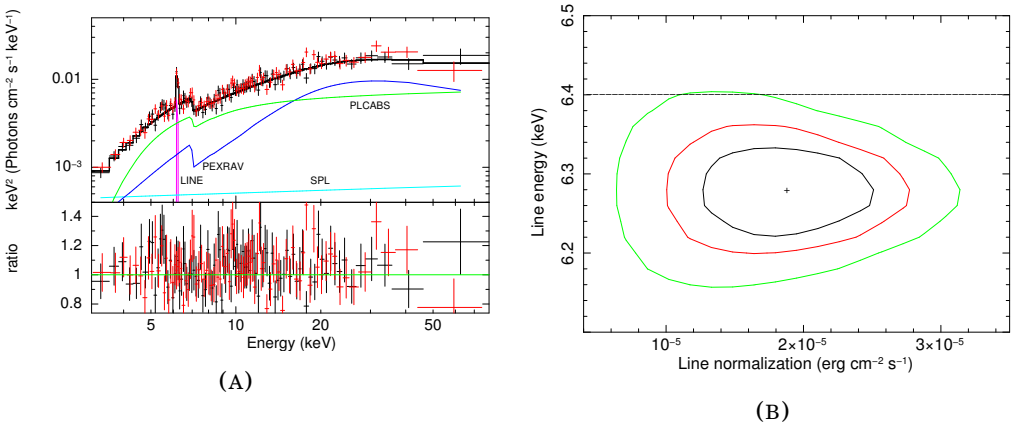

FIGURE 3.3: **(A).** Fit with the baseline model (3.1) to the NuSTAR spectrum of Mrk 1210 (FPMA in black, FPMB in red). **(B).** 68% (black), 90% (red), 99% (green) confidence contours. The two-dimensional confidence contours allow a marginal consistency with the iron Kα line at 6.4 keV, indicated by the dashed horizontal line.

($\chi^2/\nu = 517/481$), with $\Gamma = 1.57^{+0.10}_{-0.06}$, $N_{\rm H} = 2.8^{+0.7}_{-0.5} \times 10^{23}$ cm^{-2}, and half-opening angle of the torus $\theta_{\rm tor} < 65°$, from which a covering factor of > 0.4 is inferred. A very high fraction, 16^{+4}_{-5}%, of the primary power law is scattered below 5 keV.
Similarly, the `MYTorus` model in its "coupled", default mode (i.e., with a donut-shaped, smooth reprocessor with a covering factor of 0.5) gives an acceptable fit: $\chi^2/\nu = 512/480$, $\Gamma = 1.63 \pm 0.08$, $N_{\rm H} = (3.5 \pm 0.6) \times 10^{23}$ cm^{-2}, with a high fraction, (12 ± 3)%, of the primary power law scattered below 5 keV. However, using either torus model, the flattening in the spectrum above 20 keV is not properly fitted (see Figure 3.4), and we conclude that they are not able to capture the spectral shape of Mrk 1210 while the phenomenological baseline model does. This suggests that the Mrk 1210 torus contains Compton-thick material producing the pronounced Compton hump, but our line of sight does not pass the Compton-thick part in the NuSTAR observation.

A physical picture

In the previous Section we found that the reflection component, modeled with a `pexrav` model, has a normalization a factor of ~ 2.5 larger than the primary continuum from the AGN. Indeed, applying other self-consistent models based on Monte Carlo simulations with a classic toroidal geometry, we found worse fits with respect to that obtained with the baseline model, due to the presence of the reflection excess.
While the `Torus` model allows the user to fit for the torus opening angle and hence to get an estimate of the covering factor of the source, the three components of the `MYTorus` model can be decoupled (transmitted flux, reflected flux, and fluorescence lines) to simulate different and more complex geometries. We refer to Yaqoob (2012) for an extensive explanation of the decoupled version of the model, and also LaMassa et al. (2014) for a systematic application of the model on a sample of sources.

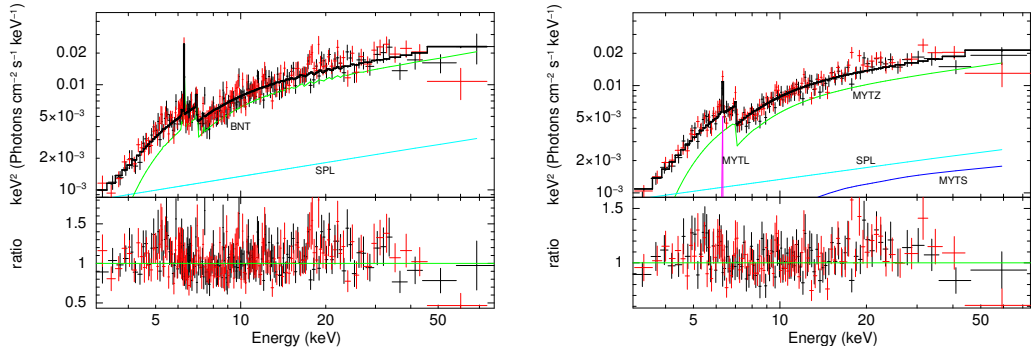

(A) (B)

FIGURE 3.4: **(A).** Fit (top) and data/model ratio (bottom) with with the `Torus` model to the NuSTAR spectrum of Mrk 1210 (FPMA in black, FPMB in red). **(B).** Same of the left Figure, for the coupled `MYTorus` model.

The way in which the `MYTorus` model can be decoupled has been already explained in §2.1.2. We briefly recall that, together with the canonical components with a l.o.s. angle fixed at 90° (called front-scattered, with the subscript 90), the decoupled version includes an additional couple of scattered+line components seen face on, that is, with the l.o.s. angle fixed to 0° (called back-scattered, with the subscript 00). The relative normalizations between the 90° and 0° components (called A_{S90} and A_{S00}, respectively) can be untied and left free in the fit. Additionally, one can also untie the column densities of the two scattered/reflected components. In XSPEC notation, this model is described as

$$\begin{aligned} \text{MYT\_DEC} = {} & \overbrace{\text{constant}}^{\text{cross-normalization}} \times \overbrace{\text{phabs}}^{\text{Gal. absorption}} \times \\ & \times (\overbrace{\text{zpowerlw} \times \text{MYTZ}}^{\text{absorption}} + \overbrace{\text{MYT}_{\text{S,90}} + \text{MYT}_{\text{L,90}}}^{\text{front-scattering}} + \\ & + \overbrace{\text{MYT}_{\text{S,00}} + \text{MYT}_{\text{L,00}}}^{\text{back-scattering}} + \overbrace{f_{\text{s}} \times \text{zpowerlw}}^{\text{soft component (SPL)}}). \end{aligned} \tag{3.2}$$

If we decouple the model (i.e., we leave free the constants A_{S90} and A_{S00}), and allow the obscuring columns to be different (i.e., $N_{H90} \neq N_{H00}$), we get a good fit (χ^2/ν = 489/479, Figure 3.5). The front-scattered component vanishes (i.e., $A_{S90} \to 0$), while the back-scattered component converges to the same normalization as the primary continuum (i.e., $A_{S00} \to 1$, preserving the internal self-consistency of the model), and the clouds responsible for the reflection component are Compton-thick, with an optical depth $\tau \sim 2.7$ ($N_{\text{H}} \sim 4 \times 10^{24}$ cm^{-2}). Moreover, the upper limit on the column density is unconstrained by the fit. In other words, the column density obscuring the l.o.s. is different from the column density of the clouds responsible for the back-scattered reflection. Fixing the normalizations of the back-scattered component and the primary power law to be equal as suggested by the fit (i.e., $A_{S00} = 1$) does not change the result regarding the different column densities for the two components. On the other hand,

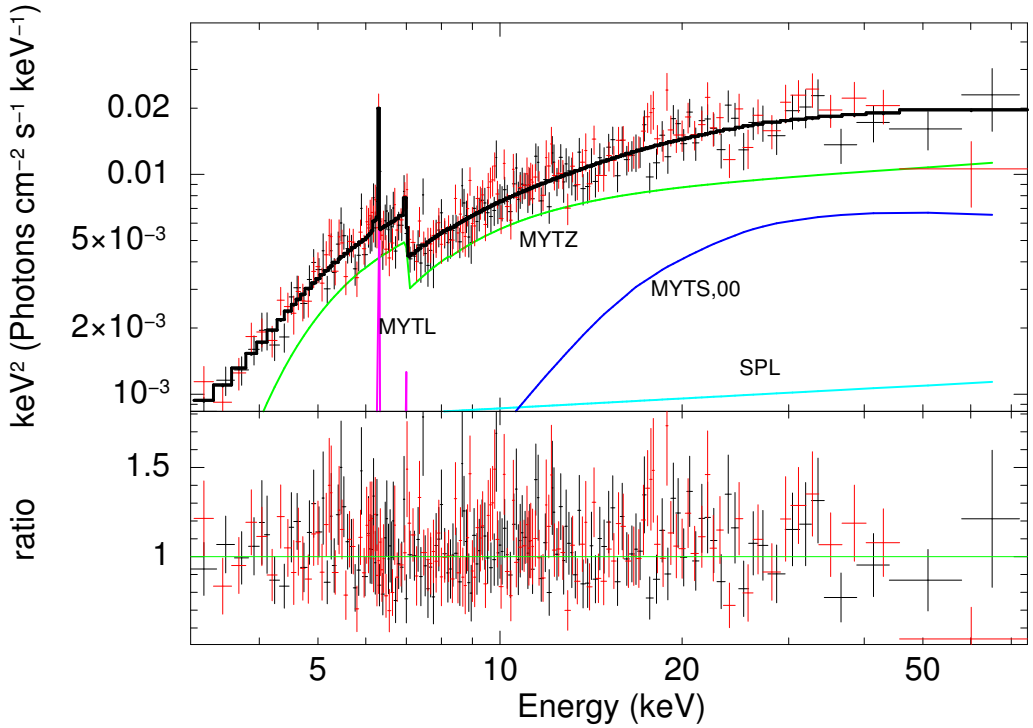

FIGURE 3.5: Fit with the `MYTorus` decoupled model (3.2), with normalizations and column densities decoupled (FPMA in black, FPMB in red). Fitting parameters are reported in Table 3.2.

TABLE 3.2: Summary of spectral analysis.

Parameter	Models		
	BASELINE	MYT*	MYT decoupled
χ^2/ν	478/478	512/480	489/479
Γ	$1.90^{+0.11}_{-0.12}$	$1.63^{+0.08}_{-0.07}$	1.85 ± 0.12
$N_{\rm H}$ [cm^{-2}]	$3.0^{+0.7}_{-0.6} \times 10^{23}$	$3.5^{+0.6}_{-0.6} \times 10^{23}$	$3.3^{+0.8}_{-0.7} \times 10^{23}$
Norm transmitted comp @1 keV [ph cm^{-2} s^{-1} keV^{-1}]	$5.1^{+1.3}_{-1.0} \times 10^{-3}$	$4.8^{+1.3}_{-1.1} \times 10^{-3}$	$7.8^{+3.8}_{-2.6} \times 10^{-3}$
Norm reflected comp @1 keV [ph cm^{-2} s^{-1} keV^{-1}][a]	$1.2^{+0.9}_{-0.5} \times 10^{-2}$	4.8×10^{-3} (fixed)	$7.7^{+5.1}_{-3.1} \times 10^{-3}$
$N_{\rm H00}$ [cm^{-2}][b]	–	–	$4.0^{+u}_{-1.6} \times 10^{24}$
Line Energy [keV]	$6.28^{+0.06}_{-0.07}$	–	–
EW Line [eV]	141 ± 50	–	–
Norm line component (flux) [ph cm^{-2} s^{-1}]	$(1.9 \pm 0.7) \times 10^{-5}$	–	–
$f_{\rm s}$ [%]	8^{+5}_{-6}	12^{+3}_{-2}	8^{+3}_{-2}
F_{2-10} [erg cm^{-2} s^{-1}]	7.6×10^{-12}	7.8×10^{-12}	7.7×10^{-12}
F_{10-40} [erg cm^{-2} s^{-1}]	3.0×10^{-11}	2.9×10^{-11}	3.0×10^{-11}
$L^{\rm int}_{2-10}$ [erg s^{-1}]	6.0×10^{42}	8.6×10^{42}	1.0×10^{43}
$L^{\rm int}_{10-40}$ [erg s^{-1}]	6.1×10^{42}	1.3×10^{43}	1.1×10^{43}
FPMB/FPMA	1.05 ± 0.03	1.05 ± 0.03	1.05 ± 0.03

The values of the fluxes reported in the table are the observed ones, while those of the luminosities are intrinsic, i.e., deabsorbed.

* The results using a `Torus` model are the same within the uncertainties, and the main parameters of the fit are described in the text. We chose to show the `MYTorus` results to facilitate comparison between the coupled and decoupled cases.

[a] The reflection component is the `pexrav` model in the first column. In the coupled configuration of `MYTorus`, absorption, fluorescence and reflection are self-consistently treated. For this reason, only one normalization is needed to describe all the components (second column). In the last column, the reflection is instead made up from the back-scattered `MYTorus` component, namely MYTS,00.

[b] The column density is associated with the back-scattered reflection component in the decoupled `MYTorus` model, MYTS,00.

the fit becomes worse (χ^2/ν = 505/479, $\Delta\chi^2$ = 16 for the same number of degrees of freedom) if the reflection component is front-scattered, that is, if we simply decouple the column densities from the default configuration of `MYTorus`. Also in this case, the data require two different absorbing columns: a Compton-thin one obscuring the primary emission, and a thick one producing the reflection. The parameters of the models used for fitting (baseline, toroidal, `MYTorus` decoupled) are shown in Table 3.2.

Intrinsic luminosity

Our models find an intrinsic $2-10$ keV luminosity in the range $0.6-1\times10^{43}$ erg s^{-1}. It is interesting to compare these results with other commonly used proxies for the X-ray luminosity. Using the mid-infrared luminosity, the *WISE* all-sky catalog (Wright et al., 2010; Cutri et al., 2013) reports a $W3$ (12 μm) magnitude of 4.634 ± 0.015, which translates to a 12 micron luminosity $L_{12\mu\mathrm{m}} = 4.6\times10^{43}$ erg s^{-1}, with a $\sim$ 1.5% statistical error, using the standard *WISE* zeropoints. The $W1-W2$ color is 1.392 ± 0.030, suggesting that the mid-infrared luminosity is AGN-dominated, being the source above the color threshold of $W1-W2>0.8$ identified by Stern et al. (2012). Then, from the mid-IR/X-ray relation (Gandhi et al., 2009; Asmus et al., 2015), one would predict $\log(L_{2-10}[\mathrm{erg/s}]) \sim 43.3$, which is consistent with our `MYTorus` luminosity given the $\sim$ 0.3 dex of intrinsic scatter reported by Asmus et al. (2015).
We can also use the optical [OIII] emission line to provide another independent estimate of the X-ray luminosity. Koss et al. (2017) report a dust reddening-corrected [OIII]λ5007 flux of $F^{\mathrm{c}}_{[\mathrm{OIII}]} \sim 8.03\times10^{-13}$ erg cm^{-2} s^{-1}, from which we derive a luminosity of $L_{[\mathrm{OIII}]} \sim 3.0\times10^{41}$ erg s^{-1}. Using the relationship for Seyfert galaxies between L_{2-10} and $L_{[\mathrm{OIII}]}$ with a scatter of 0.5 dex presented in Berney et al. (2015), we predict $\log(L_{2-10}[\mathrm{erg/s}]) \sim 43.3$, consistent with the luminosity derived from the infrared and with that obtained by our spectral analysis. These values suggest that the luminosity derived by the baseline model is likely underestimated by a factor of $\sim$ 2, due to the phenomenological combination of the absorbed power law and infinite slab reflection models. The physically motivated, decoupled `MYTorus` model alleviates this problem and allows for a more reliable estimate of the intrinsic luminosity of the source.

3.2.3 Long-term behavior and discussion

In order to understand the time dependent variation of the X-ray spectrum, we compiled the observed $2-10$ keV fluxes, iron line equivalent widths, and column densities from the literature together with results of this work to gain a global picture of the behavior of the source. We choose to use our baseline model parameters (shown in Table 3.2) in order to compare directly with the results from previous papers based on the same phenomenological models. To do so, we reduced the data of the six *Chandra* observations with standard procedures. See the Appendix A for the analysis of the 2004 observation (hereafter "C0"), while for the other five observations during 2008

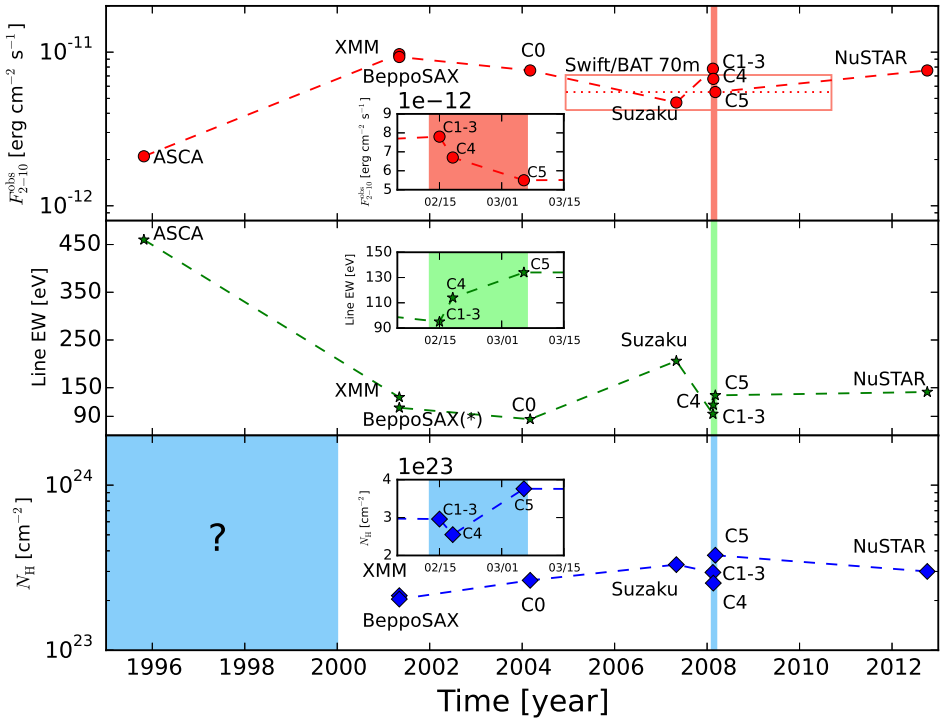

FIGURE 3.6: Observed flux in the 2 – 10 keV band of Mrk 1210 (top panel), Fe Kα line equivalent width (middle panel) and column density (bottom panel) as a function of time. The inset panels show the zoomed-in region of the five *Chandra* observations during 2008. (*) We report here the equivalent width of model 1 instead of that of model 2 in Ohno, Fukazawa, and Iyomoto (2004). The two values are consistent within the uncertainties, and we adopt the more constrained one for clarity.

(namely, "C1-5") the best-fitting models of Risaliti et al. (2010), analogous to our baseline model, were applied. We also note that Mrk 1210 is bright enough to be detected by the Burst Alert Telescope (BAT) onboard *Swift*, and it is indeed present in the *Swift*-BAT 70-month catalog (Baumgartner et al., 2013). As can be seen easily from the top panel of Figure 3.6, the source was in a low-flux state during the *ASCA* observation. It has been seen in a high-flux state since then, with different observatories. The equivalent widths of the iron line (Figure 3.6, middle panel) reflect this trend. From the bottom panel of Figure 3.6 it is clear that the column density of the source has been around $2-4\times10^{23}$ cm^{-2} since 2001, while the *ASCA* data do not help in shedding light on the column density in 1995. Both Awaki et al. (2000) and Guainazzi et al. (2002) found a Compton-thin obscuration applying a pure transmission model to the *ASCA* data, despite obtaining a worse fit with respect to a reflection-dominated scenario. The absorption-corrected 2 – 10 keV luminosity reported by Awaki et al. (2000), on the other hand, is a factor of approximately five lower than the later, intrinsic luminosities, but the quality of the data does not allow for a robust estimate of the intrinsic luminosity, nor a robust detection of the transmitted continuum, leaving total degeneracy between

TABLE 3.3: *ASCA* best fit parameters compared with NuSTAR `pexrav+zgauss` only model. The NuSTAR line equivalent width is calculated with respect to the reflection continuum.

Parameter	*ASCA*	NuSTAR (pexrav+line)
Γ	$1.95^{+0.45}_{-0.40}$	$1.90^{+0.11}_{-0.12}$
Line EW [eV]	460 ± 210	484
F_{2-10} [cgs]	1.8×10^{-12}	2.3×10^{-12}
$L^{\rm int}_{2-10}$ [cgs]	2.3×10^{42}	0.9×10^{42}

heavily absorbed and intrinsically faint primary emission scenarios. In the following, both the flux change and the eclipsing scenario are discussed.

Change in intrinsic luminosity

If we suppose that Mrk 1210 was Compton-thin also during the *ASCA* observation, but with the intrinsic emission shut off, the reflection-dominated spectrum was entirely due to an echo of a previous high-flux state.

Thanks to the high-quality NuSTAR spectrum, we are able to disentangle the intrinsic power law and the reflection component. If we shut off the intrinsic component in our NuSTAR data, leaving only the `pexrav` model and the line component (i.e., a reflection dominated model), we find an observed flux and line equivalent width consistent with the values reported by Awaki et al. (2000), albeit that uncertainties on these values cannot be reliably computed, being a reflection dominated scenario highly disfavored by the NuSTAR data, as already discussed in §3.2.2 (see Table 3.3).

Moreover, from the NuSTAR best fit baseline model, we can easily adjust the fit parameters, and vary only the normalization of the intrinsic continuum, to recover all the subsequent states of Mrk 1210, which are similar to the NuSTAR one. This means that keeping a reflection component constant and varying only the intrinsic continuum, together with minor (factor $\sim$ 2) but required column density variations on shorter timescales (as noted by Risaliti et al., 2010), all the observations of the Phoenix galaxy during the last $\sim$ 20 years can be explained.

As a further check, the $10-40$ keV observed flux and line flux are plotted in Figure 3.7. In the top panel, we computed the $10-40$ keV flux, which is the band where the reflection component is thought to dominate, from *BeppoSAX*/PDS[2], *Swift*-BAT 70-month catalog[3], and NuSTAR. We also extrapolated the *ASCA* $10-40$ keV flux, using the same procedure of *Swift*-BAT. The bottom panel shows the line flux for the iron line component, measured using different instruments. Both panels appear to confirm the constancy of the reflection through the years, with a hint of a slightly enhanced line during the *Suzaku* observation.

If this is the correct picture, Mrk 1210 turned on between 1995 and 2001, and stayed

[2] adapted from `http://www.asdc.asi.it/bepposax/nfiarchive/reproc/5125800200/html/index.html`

[3] the $14-195$ keV flux was converted to a $10-40$ keV using the `dummyrsp` command in XSPEC.

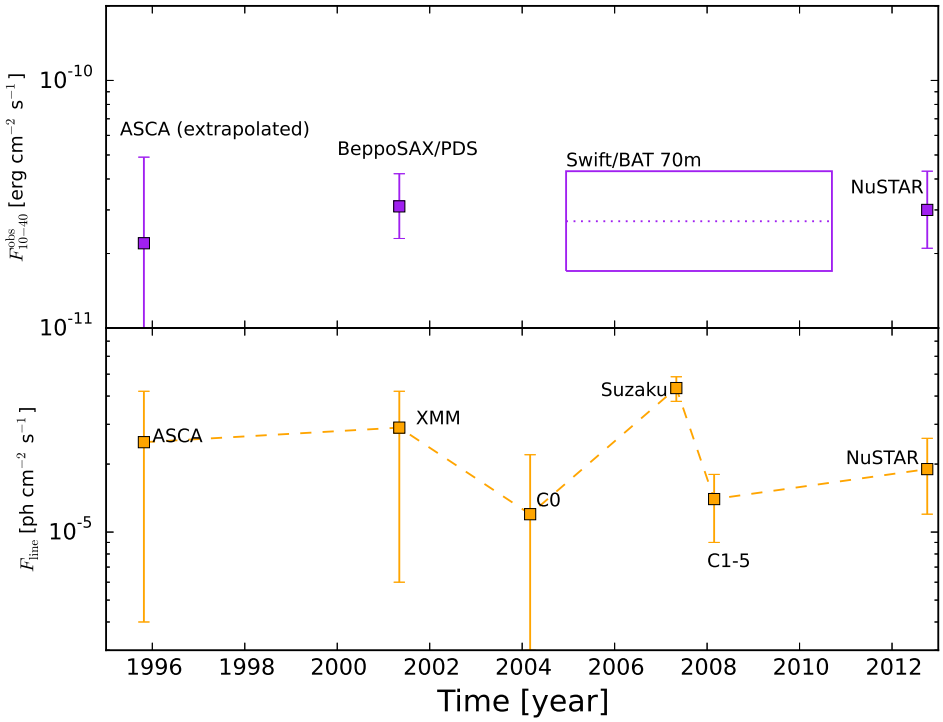

FIGURE 3.7: Observed $10-40$ keV flux (top panel) and iron line flux (bottom panel) of Mrk 1210, as a function of time.

more or less constant since then. The reflection component, though, still has to adjust and respond to this change, since it can be considered constant between all the observations. A simple light-travel argument can then put constraints on the distance between the central source and the reflector. For an edge-on view of the system, $D = c\Delta t/2$, and $\Delta t > 12-17$ yr, depending on when the source switched on (between the beginning of 1996 and the beginning of 2001). In this case, the distance between the source and the reflector is $D > (1.9-2.6)$ pc. First a fading, and then an increase in reflection is then expected to occur in the future, and monitoring of the source is the only way to keep track of its changes. Monitoring could also shed new light on the role of the X-ray absorber, which varies on much shorter temporal scales and seems to be associated with broad line region (BLR) clouds (see Risaliti et al., 2010). If this is the case, the physical interpretation of our result applying the decoupled `MYTorus` model is straightforward: the l.o.s. is intercepting the variable (and presumably compact) Compton-thin absorber, while the reflector is located on larger scales and the photons reflecting back to our l.o.s. are 'seeing' a Compton-thick column of gas. Risaliti et al. (2010) suggest that the absorber is a BLR cloud, assuming a central black hole (BH) mass of $5-7\times10^7\ M_\odot$. In this picture, a second "screen" is required to obscure the broad lines in the optical spectrum, which is instead likely showing an outflow, resulting in the classification of Mrk 1210 as a Seyfert 2 (Mazzalay and Rodríguez-Ardila,

2007). However, if the reflection component comes from photons reflecting off the far inner wall of the torus, delayed with respect to the intrinsic emission, a rather distant torus edge is needed with respect to the dust sublimation radius $R_{\rm sub}$, which is usually thought to mark the inner wall of the torus, and in this case is ~ 0.2 pc (Gandhi et al., 2009 and references therein, and adopting a bolometric correction of 20, Lusso et al., 2012).

Eclipsing event

The *ASCA* data cannot distinguish between a Compton-thick eclipsing event and an intrinsic low-flux state of the central engine. A random pass of a Compton-thick cloud (or an alignment of clouds along the l.o.s.) during the *ASCA* observation is consistent with the known clumpiness of the gas surrounding obscured AGN. During the two observations by *ASCA* in 1995, separated by 25 days, Mrk 1210 was in a low-flux state. In an eclipsing scenario, this means that the putative eclipsing event lasted for at least 25 days. Assuming Keplerian motion of the clump, the linear size eclipsed by a moving Compton-thick cloud in a given time interval can be written as $s = 4.5 \times 10^{13} (M_7/D_{\rm pc})^{1/2} \Delta t_{25}$ cm, where $D_{\rm pc}$ is the distance from the center in parsecs, and Δt_{25} is the eclipse time interval in units of 25 days. This implies that the cloud is rotating with a Keplerian velocity $v_{\rm K} \sim 210 (M_7/D_{\rm pc})^{1/2}$ km/s. Finally, assuming a Compton-thick column density, the average density of the clump is $\rho \sim 2 \times 10^{10} N_{\rm H,24} (D_{\rm pc}/M_7)^{1/2}/\Delta t_{25}$ cm^{-3}, where $N_{\rm H,24}$ is the column density in units of 10^{24} cm^{-2}. Interestingly, high-density clumps on a parsec-scale (or subparsec-scale) are observed in some systems showing water maser emission at 22 GHz. Mrk 1210 is indeed one of them (Braatz, Wilson, and Henkel, 1994), even if the association of the maser spots to a particular geometry is still unclear and sensitive VLBI observations are needed to further investigate the nuclear environment. The maser activity could indeed be associated with a dusty Keplerian disk orbiting the SMBH, from which the most precise BH mass available to date could be derived (e.g., Kuo et al., 2011). This would allow a direct comparison of this object with other samples of disk masers (Pesce et al., 2015; Masini et al., 2016) and retrieve information about the X-ray absorber. On the other hand, the maser spots could be associated with the outflow seen in the optical spectrum, invalidating any possible BH mass estimate. Moreover, as reported by Storchi-Bergmann, Fernandes, and Schmitt (1998) and Mazzalay and Rodríguez-Ardila (2007), Mrk 1210 probably shows a recent circumnuclear starburst. If the masers are associated with the outflow responsible for the broad components of the optical lines, the Phoenix galaxy could be a very interesting and local laboratory to study the interplay between AGN activity and star formation.

3.3 Variability and iron lines in other nearby Seyferts

3.3.1 IC3639

IC3639 is a nearby ($z = 0.011$) barred spiral galaxy hosting an obscured AGN. It has been recently object of a NuSTAR observation (Boorman et al., 2016), which found it extremely obscured ($N_{\rm H} \gtrsim 10^{25}$ cm^{-2}) with a very prominent iron Kα line (EW $\sim 2-3$ keV). A joint *Suzaku* and NuSTAR spectrum of IC3639 is shown in Figure 3.8a. Previous observations found the same results (Risaliti et al., 1999), suggesting that the system is stable in obscuration and accretion state. The stability of the obscuration state of the system during time is also confirmed by the determination of the intrinsic parameters of the source (i.e., intrinsic luminosity, Eddington ratio), which are consistent with multiple observations reported over almost two decades. As already mentioned, Boorman et al. (2016) calculated the iron line EW carrying out a four dimensional grid to step over the fit parameters, and found an extreme value of EW $= 2.94^{+2.79}_{-1.30}$ keV. IC3639 is then at the highest end of the EW distribution of local *bona-fide* CT AGN, contrary to NGC7674, of which we shall discuss next.

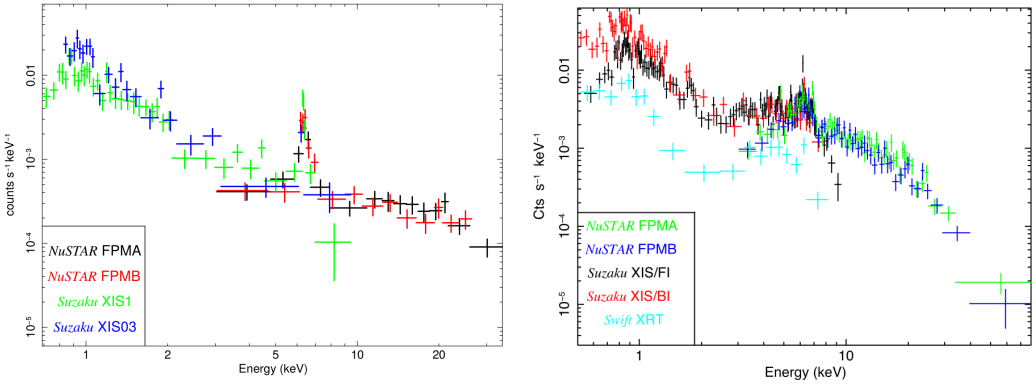

FIGURE 3.8: **(A).** NuSTAR and *Suzaku* broadband ($0.7-35$ keV) spectrum of IC3639 (FPMA in black, FPMB in red; XIS1 in green, XIS03 in blue). The iron line between 6 and 7 keV is very evident. The spectrum resembles the reflection-dominated spectra of extremely obscured megamasers of Chapter 2. Figure adapted from Boorman et al. (2016). **(B).** NuSTAR, *Suzaku* and *Swift*-XRT broadband ($0.5-80$ keV) spectrum of NGC7674. Despite being both CT AGN, the two sources show different spectral shapes, mainly in the NuSTAR band. Figure adapted from Gandhi et al. (2017).

3.3.2 NGC7674

NGC7674 ($z = 0.0289$) is the brightest member of the Hickson 96 interacting group, and is a well-known Seyfert 2 galaxy. Similarly to what happened for Mrk1210, this source was first reported to be a reflection-dominated, highly obscured AGN in 1996 by a BeppoSAX observation (Malaguti et al., 1998). However, previous detections reported a rather high-flux state of the source activity, arguing for a changing-look behavior

as well. The state transition went from a high-flux state to a low-flux one, contrary to the "awakening" (Phoenix galaxy effect) of Mrk1210. A NuSTAR observation of NGC7674, together with a thorough analysis of its long-term variability, is presented in Gandhi et al. (2017). The peculiarity of this source is given by its weak iron Kα line (EW= $0.38^{+0.10}_{-0.09}$ keV) despite its CT obscuration state. NGC7674 is indeed at the lower extreme of the iron Kα EW distribution, being the *bona-fide* CT AGN with the weakest line to date. This fact may be due to a low iron elemental abundance, or to an absorbed scattering solution, while the dilution by a jet is considered to be unlikely. Sources like NGC7674 further challenge the search for CT AGN in deep surveys, where the photon statistics is poor. Indeed, Koss et al. (2015) demonstrated that a robust characterization of typical nearby CT AGN (such as NGC3393, one of the megamasers already discussed), relying on detection of the Fe Kα emission line and broad-band continuum for spectral modeling, is only possible at relatively low redshifts of $z < 0.2$. With a value of EW weaker by a factor of ~ 3 than NGC3393, it becomes even more difficult to identify an object similar to NGC7674 as being CT in a deep survey. Indeed, Gandhi et al. (2017) shift the spectrum of NGC7674 to $z = 0.25$, simulated on its best-fitting, CT toroidal model, and fit it again in low signal-to-noise regime. The same toroidal model returns a Compton-thin column density in such a regime, indicating that a spectrum like NGC7674 would not be considered as CT in a deep, hard X-ray survey, due to the combination of lack of a prominent iron line and low statistics.

3.4 Summary of this Chapter

In this Chapter devoted to AGN variability with a NuSTAR perspective, we presented a snapshot observation of Mrk 1210, also known as the Phoenix galaxy. It is a long-studied object, considered to be part of the "changing-look" class of AGN. NuSTAR observed Mrk 1210 obscured by a Compton-thin column of gas similarly to other instruments over the past 16 years. The data are also showing an enhanced reflection component, which requires two different columns of gas to be taken into account. Many previous studies have suggested the presence of a variable X-ray absorber, inducing changes in the absorbing column of a factor ~ 2 on the timescales of days and weeks. We note that these short-term column changes, properly complemented by long-term intrinsic variability of the central engine, are able to explain the line equivalent widths and fluxes observed by different instruments over the last ~ 20 years. If the low flux-state observed by *ASCA* in 1995 is due to an intrinsic fading of the engine, we note evidence that the reflection component has remained constant with time. In this scenario, we infer that the physical distance between the source and the reflector is of the order of at least 2 pc. First a drop, and then an enhancement of the reflection component are then expected to occur in the future, in response to the source "low-flux state" (seen by *ASCA*) and soft X-ray "awakening" (i.e., the Phoenix effect, Guainazzi et al., 2002) seen between 1996 and 2001. On the other hand, if the low-flux state of

Mrk 1210 during the *ASCA* observation can be ascribed to the presence of a Compton-thick cloud obscuring the l.o.s., the cloud can be identified with a maser-emitting clump on the sub-pc scale. Indeed, if the torus-like structure is clumpy, a random passage of an over-dense cloud along the l.o.s. is expected (Wada, 2012). The frequency in which such events are to be expected could be evaluated with precise hydrodynamical simulations of the nuclear environment, but we refer to Markowitz, Krumpe, and Nikutta (2014) for a statistical study on this topic.
Monitoring in the X-ray band is needed, either to detect the expected behavior of the reflection component and clarify the relation between the X-ray absorber and reflector, which seem to be on different spatial scales, or to possibly detect another low-flux state and further study the properties of the clumpy (sub)pc-scale absorber. To this extent, radio VLBI monitoring at 22 GHz would also be extremely useful to clarify the nature of the nuclear water maser activity. In the last part of the Chapter, we also discussed two other examples of local CT AGN studied by NuSTAR, both lacking and showing X-ray variability, one with an extreme EW iron line (IC3639) and one with an unexpectedly weak iron line (NGC7674). Studies of local samples of CT AGN, such as the megamasers, or peculiar objects like NGC7674, can help to understand the biases and systematics affecting deep X-ray surveys searching for CT AGN at the peak of cosmic AGN and star formation (SF) activity ($z \gtrsim 1$).

Chapter 4

Obscured AGN in deep surveys: the NuSTAR UKIDSS - UDS survey

In this Chapter, based almost entirely on the paper submitted to ApJ *"The NuSTAR Extragalactic Surveys: source catalog and the Compton-thick fraction in the UDS field"*, by Masini, A., et al., the NuSTAR survey of the UKIDSS-UDS field is presented. After discussing the major results obtained by NuSTAR thanks to its Extragalactic Survey program, the survey strategy, the detection algorithm and simulations used to assess the reliability and completeness of the survey are described. The detected sources are first matched to their soft X-ray counterparts, employing XMM-*Newton* and *Chandra* catalogs, and then to their optical counterparts. The majority of the NuSTAR-detected sources have a redshift, and allow a joint XMM-*Newton*/*Chandra* + NuSTAR broadband ($0.5-24$ keV) spectral analysis to be performed in order to obtain the column density distribution of the entire sample. In the last part of the Chapter, the observed CT fraction in the UDS field is computed combining the standard hardness ratio diagnostic with results from the broadband spectral analysis of all the sources in the catalog, adopting toroidal models for the spectral fitting of CT candidates. The *observed* CT fraction is going to be measured, since the *intrinsic* CT fraction is an even more difficult measurement to perform in such deep surveys, needing the absorption biases and survey completeness to be taken into account when correcting the observed value. This is the first contribution of NuSTAR to a robust determination of the observed CT fraction in a deep survey field, and the result is compared to predictions of some theoretical models of the X-ray background.

4.1 Hard X-ray surveys with NuSTAR, and the UDS field

As already discussed in Chapter 1 (Section §1.2), AGN are effectively detected, traced and studied by X-ray surveys (Brandt and Alexander, 2015), due to their high luminosity at X-ray wavelengths ($L_{\rm X} \gtrsim 10^{42}$ erg s^{-1}). Indeed, in the past decades, the advent of XMM-*Newton* and *Chandra* was a breakthrough in AGN research, and dozens of

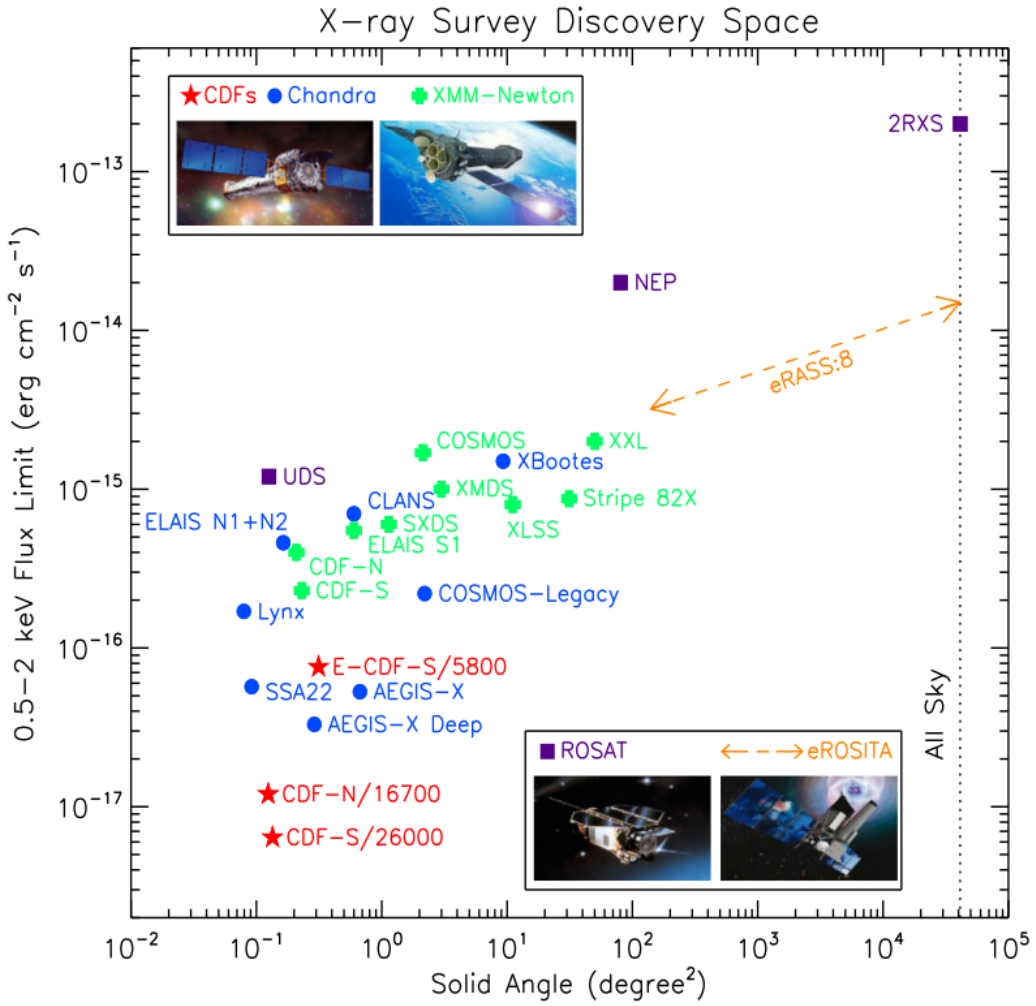

FIGURE 4.1: Limiting $0.5-2$ keV flux as a function of solid angles covered by some X-ray surveys from XMM-*Newton*, *Chandra*, ROSAT, and eROSITA. Figure adapted from Xue (2017).

X-ray surveys covered a wide range in the flux-area plane (see Figure 4.1), exploring a large range in redshift and luminosity. These works allowed the luminosity function of AGN to be measured up to $z \sim 5$, both for unobscured ($N_{\rm H} < 10^{22}$ cm^{-2}) and obscured ($N_{\rm H} > 10^{22}$ cm^{-2}) sources (e.g., Ueda et al., 2003; La Franca et al., 2005; Polletta et al., 2006; Vito et al., 2014; Marchesi et al., 2016).

However, as already discussed in this Thesis, these surveys were biased against the detection of AGN obscured by large columns of gas such as the CT AGN, mainly in the local Universe, up to $z \lesssim 1$.

Given the importance of CT AGN in the recent developments of the AGN field (Section §1.2.2), the fraction of CT AGN is a key observable for X-ray surveys, but its determination suffers degeneracies and observational biases, which have been partially mitigated with the advent of NuSTAR (Harrison et al., 2013), as already discussed in Chapter 1. Thanks to NuSTAR, sensitive hard X-ray surveys above 10 keV started to

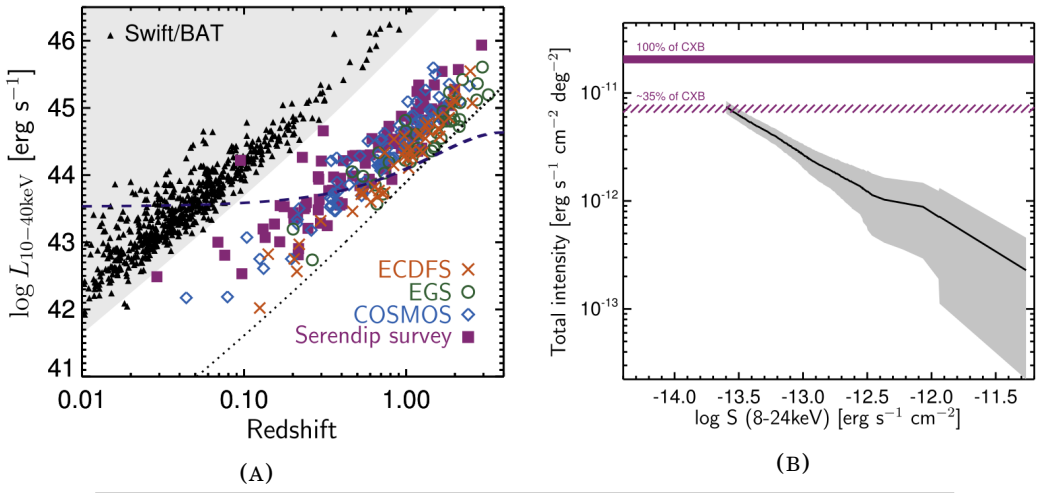

FIGURE 4.2: **(A).** Luminosity in the 10 – 40 keV band as a function of redshift for some selected NuSTAR surveys. Small black triangles refer to 70-month *Swift*-BAT sources (Baumgartner et al., 2013). Figure adapted from Harrison et al. (2016). **(B).** Cumulated intensity of resolved sources from some NuSTAR surveys, as a function of their 8 – 24 keV flux. At the flux limit of NuSTAR, the total intensity makes up for the 35% of the total CXB intensity. Figure adapted from Harrison et al. (2016).

be feasible (Figure 4.2a), and allowed pushing the search for CT AGN beyond the local Universe, directly resolving up to the 35% of the CXB in the 8 – 24 keV band (Harrison et al., 2016, and Figure 4.2b). A wedding-cake strategy for the NuSTAR surveys was adopted: a shallow, wide area survey of the Cosmic Evolution Survey field (COSMOS, Civano et al., 2015, C15 hereafter), a deep, pencil-beam survey of the Extended *Chandra* Deep Field-South (ECDFS, Mullaney et al., 2015), and a Serendipitous survey (Alexander et al., 2013; Lansbury et al., 2017b) were the first steps of a comprehensive survey program, which is now complemented by the observations of the Extended Groth Strip (EGS, Aird et al. in prep), *Chandra* Deep Field-North (CDFN, Del Moro et al. in prep) and UKIDSS - Ultra Deep Survey (UDS) fields (Masini et al. submitted).
In this Chapter, we present the NuSTAR survey of the UDS field. This field is the deepest component of the UKIRT Infrared Deep Sky Survey (UKIDSS; Lawrence et al., 2007; Almaini et al., 2007), and has an extensive multi-wavelength coverage. In the radio band, there is a Very Large Array (VLA) coverage at 1.4 GHz (Simpson et al., 2006). Submillimeter coverage comes from the SCUBA Half-Degree Extragalactic Survey (SHADES) survey of the central region of the UDS field (Coppin et al., 2006). The infrared (IR) band is the most covered, with both ground-based and in-orbit facilities: *Herschel* observed the UDS field as part of the HerMES program (Oliver et al., 2012), while *Spitzer* observed UDS within the SWIRE survey (Lonsdale et al., 2003) and, more recently, within the SpUDS Spitzer Legacy Survey (PI: Dunlop). Ground-based IR facilities observed the field, primarily the UKIRT WFCAM (Casali et al., 2007) and VISTA, as part of the VIDEO survey (Jarvis et al., 2013). Also *Hubble* Space Telescope (HST) WFC3 coverage is available (Galametz et al., 2013), together with deep optical

Subaru Suprime-cam imaging data (Furusawa et al., 2008). Coverage in the U band is provided by the CFHT Megacam (PIs: Almaini, Foucaud). Despite this large suite of multi-wavelength coverage, we will focus on the X-ray coverage only, and leave the exploiting of such large datasets to future projects (e.g., to study the morphology and environment of the CT candidates identified by NuSTAR). In the X-ray band, the NuSTAR coverage is centered on the coordinates (J2000) R.A. = 34.4 deg and DEC. = −5.1 deg, and it overlaps with the Subaru XMM-*Newton* Deep Survey (SXDS, Ueda et al., 2008) and *Chandra* UDS survey (Kocevski et al. 2017 submitted) fields. The different X-ray coverages are shown in Figure 4.3a.
In the following, we assume a flat ΛCDM cosmology ($H_0 = 70$ km s^{-1} Mpc^{-1}, $\Omega_M = 0.3$, $\Omega_\Lambda = 0.7$).

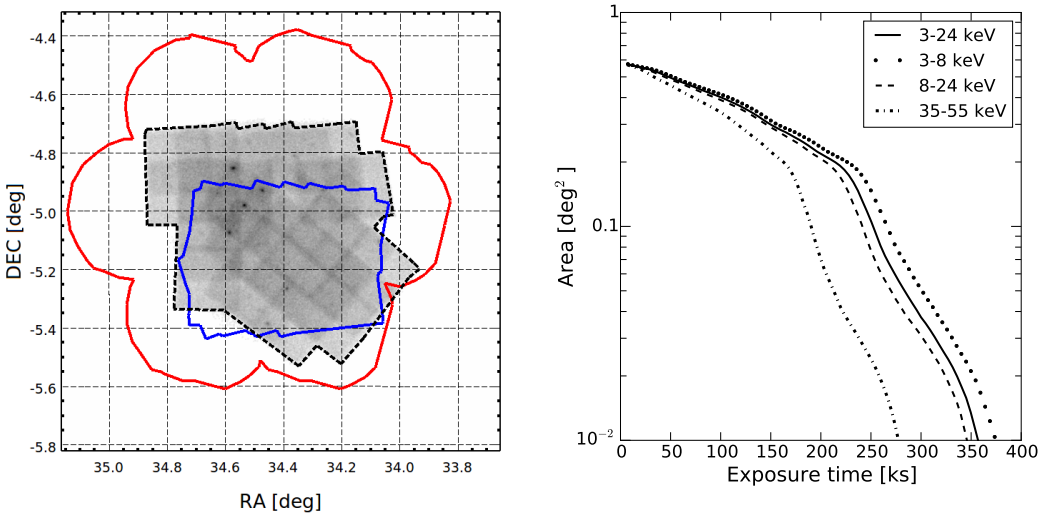

(A) (B)

FIGURE 4.3: **(A).** Different coverings of the UDS field in the X-ray band. The NuSTAR coverage (dashed black) is compared with the flower-shaped XMM-*Newton* (red) and the *Chandra* (blue) coverages. **(B).** Cumulative survey area as a function of exposure depth (FPMA+FPMB), for different energy bands. The total area is 0.58 deg^2, and the depth at half area is ~ 155 ks in the full (3 – 24 keV) band.

4.2 Data reduction

The survey consists of 35 observations, completed during two different passes, tiled with a half-Field of View (FoV) shift strategy to provide a coverage as uniform as possible, despite the roll angle changed significantly between the two passes. The first pass on the field (20 pointings) was performed between January-February 2016, while the second pass (15 pointings) was completed in October-November 2016, for a total observing time of ~ 1.75 Ms. A summary of all the observations is presented in Table 4.1.

TABLE 4.1: Details of the individual UDS observations. (1) Observation ID. (2)-(4) Coordinates and roll angle for each pointing. (5) Exposure time for FPMA, corrected for flaring episodes.

OBSID	R.A. [deg]	DEC. [deg]	Roll angle [deg]	$t_{\rm exp}$ [ks]
60111001002	34.0911	−5.1991	319.3	45.8
60111002002	34.1591	−5.2775	319.3	49.9
60111003002	34.1613	−5.137	319.3	49.5
60111004001	34.1838	−4.9979	319.3	50.1
60111005002	34.2129	−5.3638	319.2	51.6
60111006001	34.2336	−5.2305	319.1	49.8
60111007002	34.2434	−5.0723	319.2	48.2
60111008001	34.2905	−5.2937	319.3	45.4
60111009002	34.3116	−5.1499	319.3	48.1
60111010001	34.3165	−5.0071	319.2	48.0
60111011002	34.3548	−5.3761	319.2	46.5
60111012001	34.3691	−5.2269	319.2	43.3
60111013002	34.384	−5.0892	319.3	44.3
60111014001	34.3973	−4.9459	319.3	43.8
60111015002	34.44	−5.3067	324.2	51.0
60111016001	34.4424	−5.1637	324.2	55.7
60111017002	34.4632	−5.0225	324.3	51.0
60111018001	34.5089	−5.2441	324.3	49.8
60111019002	34.5231	−5.0892	324.3	48.9
60111020001	34.5345	−4.9615	324.3	50.5
60111031002	34.6363	−5.2345	175.5	51.9
60111032002	34.6439	−5.1313	177.5	48.4
60111033002	34.6426	−5.0273	179.5	48.8
60111034002	34.5369	−5.0254	179.4	50.5
60111035001	34.5345	−4.9285	179.4	50.1
60111036002	34.6373	−4.9261	180.5	51.2
60111037001	34.7387	−4.9268	182.5	50.3
60111038001	34.7404	−4.8277	184.4	51.2
60111039001	34.6419	−4.8248	187.4	50.7
60111040001	34.5355	−4.8189	190.3	49.9
60111041001	34.4367	−4.8301	194.4	51.2
60111042002	34.3471	−4.804	273.9	50.0
60111043001	34.249	−4.8016	275.9	51.3
60111044001	34.2525	−4.9036	277.4	51.7
60111045001	34.1518	−4.9055	278.9	52.1

4.2.1 Flaring episodes

The raw event files are processed using the `nupipeline` task available in the NuSTAR Data Analysis Software (NuSTARDAS[1]). Following C15, full-field lightcurves in the 3.5 – 9.5 keV energy band with a binsize of 500 s are produced in order to look for high-background time intervals. The following OBSIDs result affected by background flares (i.e., with a count rate more than a factor of ∼ 2 higher than the average, quiescent state) after the analysis of the lightcurves: 60111001002, 60111006001, 60111008001, 60111011002, 60111012001, 60111013002, 60111014001, 60111015002, 60111016001, 60111019002, 60111031002, 60111032002, 60111035001, 60111039001, 60111040001, 60111042002. After cleaning for Good Time Intervals (GTI), the time loss is 39 ks for each focal plane module (FPM), 2.2% of the total time, resulting in a total cleaned observing time of 1.730 Ms and 1.726 Ms for FPMA and FPMB, respectively.

4.2.2 Data, exposure, and background mosaics

After cleaning for flaring background episodes, we run again `nupipeline` taking into account the GTI in order to have the final list of cleaned event files. For each observation, we produce images in the 3 – 24 keV, 3 – 8 keV, 8 – 24 keV, 8 – 16 keV, 16 – 24 keV, and 35 – 55 keV energy bands. We will refer to these bands as full (F), soft (S), hard (H), hard-one (H1), hard-two (H2), and very-hard (VH), respectively. The motivation in splitting the H band into two sub-bands comes from multiple sides. On one side, the background contribution is limited in the H1 band, allowing some sources to be more significantly detected narrowing the band; on the other hand, selecting sources at ∼ 15 – 20 keV in the H2 band helps us selecting directly those AGN contributing the most to the peak of the CXB.
Since the effective area is a continuous function of energy, and producing an exposure map at every energy is extremely time-consuming, we weight the exposure map in every band with an average energy, obtained convolving the NuSTAR instrumental response with a power law of photon index $\Gamma = 1.8$. Exposure maps are created in the F, S, H, and VH energy bands with the `nuexpomap` task. A plot of the survey area as a function of vignetting-corrected exposure time is shown in Figure 4.3b.
Following the general strategy adopted for all the contiguous NuSTAR surveys, we use the `nuskybgd` software (Wik et al., 2014) to model the background in each energy band. As explained in Wik et al. (2014) and already summarized in Chapter 1 (Section §1.3), the NuSTAR background is the sum of different components; in particular, above ∼ 20 keV, the background is instrumental, and is composed of a nearly flat power law with a forest of activation lines (between ∼ 25 – 35 keV). This is the reason why the usual NuSTAR surveys are performed in the 3 – 24 keV band. We further decide to explore the energy range between the end of the strong instrumental lines, at 35 keV, up to 55 keV, where the NuSTAR effective area starts to decrease substantially.
We extract background spectra from four $160''$−radius circular regions, one for each

[1] `https://heasarc.gsfc.nasa.gov/docs/nustar/analysis/nustar_swguide.pdf`

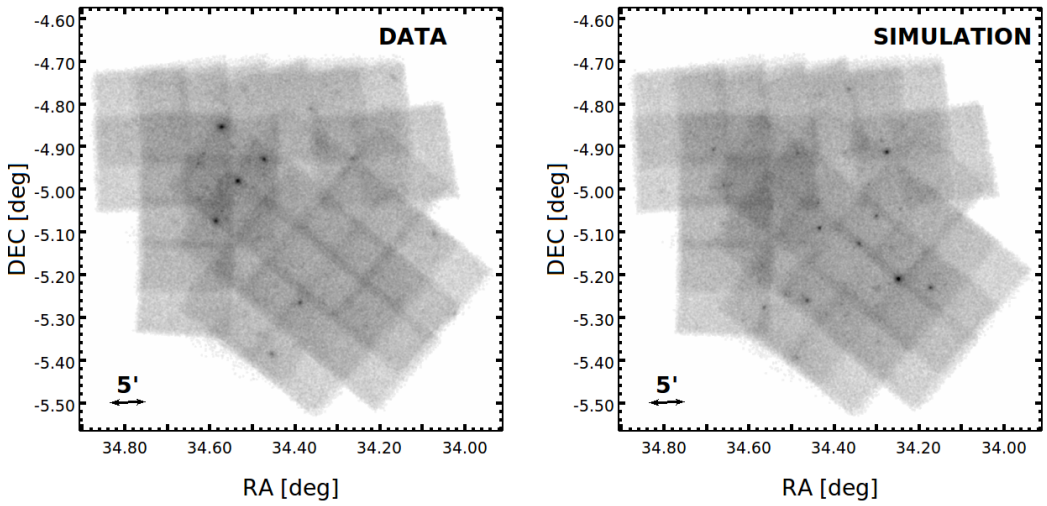

FIGURE 4.4: NuSTAR merged FPMA+FPMB 3 – 24 keV band mosaic (left panel), and one of the 400 simulations (right panel). The two pictures are in the same band, same scale, and same smoothing radius.

quadrant, avoiding chip gaps. Once the user-defined regions are provided, the `nuskybgd` software extracts and fits their spectra in XSPEC (v 12.9.1, Arnaud, 1996) with the appropriate model, and saves the best-fit parameters. These parameters can be used to extrapolate and produce a background spectrum in a particular region of the FoV, or to produce a background image of the entire FoV.

Following C15, we thaw all the relevant parameters but the normalization of the fCXB, kept frozen to its nominal value (Boldt, 1987). We then fit all the parameters using the Cash statistic (Cash, 1979), and ultimately fit for the fCXB normalization. While this procedure gave very good results in C15 (giving a $< 1\%$ discrepancy in counts between data and background) and other NuSTAR surveys (e.g. Mullaney et al., 2015), it underestimates the background counts by $3 - 4\%$, which cannot be explained by bright sources, possibly due to a fluctuation of the CXB. After an extensive number of tests, we decide to keep the normalization of the fCXB frozen to its default value (Boldt, 1987) in our fits. This recipe reconciles our background maps with the data mosaics with a maximum counts discrepancy of $\sim 1\%$. Data, exposure, and background mosaics are produced with the FTOOLS task XIMAGE.

4.3 Simulations

In order to define detection parameters, an extensive set (following C15, 400 for each energy band) of simulations is run, following the same strategy adopted by C15, that we briefly summarize here.

TABLE 4.2: Comparison between observed counts and average of simulations, after the second run.

	Data	⟨Sim⟩	(D − ⟨Sim⟩)/D [%]
3 – 24 keV	873931	874376	-0.05
3 – 8 keV	392794	392723	+0.02
8 – 24 keV	481137	481356	-0.05
8 – 16 keV	291663	291646	+0.006
16 – 24 keV	189474	189513	-0.02
35 – 55 keV[a]	357133	358531	-0.39

[a] We do not rescale the fCXB component for the VH band, since the background is instrumental only.

4.3.1 Initial setup

A first run of simulations is performed extracting sources from a logN-logS distribution (Ballantyne et al., 2011) to a minimum flux which is ∼ 10 times fainter than the expected survey limit, and placing them on a background without the fCXB component. This is done in order to prevent the simulations from having too many counts, since the fake, unresolved sources make up a part of the fCXB itself. As a result, after the first run of simulations, only a certain fraction of the fCXB contribution is missing. The fraction of fCXB that has to be added to the background depends on the (band-dependent) input limiting flux, and ranges from 61% in the S band to 94% in the H2 one. Since between 35 and 55 keV the background is only instrumental and no fCXB component is contributing, no correction is applied in the VH band.
After rescaling and adding a certain fraction of the fCXB component to the background maps, we run the simulations again and we verify that, on average, our simulations optimally represent our data mosaics. The comparison between observed data and simulations counts in each band is shown in Table 4.2, while a qualitative comparison with one of the simulated realizations is shown in Figure 4.4.

4.3.2 Reliability, completeness, and sensitivity

Once the simulations are completed, we have a set of 2400 simulations (400 for each band) which on average accurately represent our real observations. This large set of simulations is used to maximize the efficiency of our detection procedure.
Following C15, we smooth every simulation (and the background mosaic) with $10''$ and $20''$ radii circular top-hat function. Then, we convert the resulting smoothed maps into probability maps, using the `igamma` function (i.e. incomplete Γ function) in IDL, which returns the probability of having a certain number of counts $C_{\rm im}$ in the data mosaic given $C_{\rm bkg}$ background counts in the background mosaic at the same position:

$$P = \texttt{igamma}(C_{\rm im}, C_{\rm bkg}). \tag{4.1}$$

In every point of our probability maps, the numerical value is then given by $\log 1/P$. We use the *SExtractor* software (Bertin and Arnouts, 1996) on the probability maps (both $10''$ and $20''-$smoothed) to detect sources in our simulations. The two lists of sources are merged together; as discussed in C15, using two different smoothing radii increases the number of detections. Every source is then evaluated calculating its Poisson probability of being a spurious fluctuation of the background. Every source is assigned a DET_ML number, which is simply DET_ML $= -\ln P$. The higher the DET_ML, the higher the probability of the source being real, and the higher its significance. In the case where the same source is found in both the $10''$ and $20''-$smoothed maps, the most significant one (i.e., the one with the highest DET_ML) is retained. Duplicates are assessed cross-correlating the catalogs with a matching radius of $30''$. Following Mullaney et al. (2015), a deblending algorithm for counts of the detected sources is run, in order to take into account the possible contaminations induced by objects closer than $90''$. A deblended DET_ML is then re-calculated using deblended source and background counts to assess the post-deblending significance of every source.
After these steps, we end up with a catalog of sources for every simulation. Comparing the final list of sources, detected and matched, with the ones input to the simulations allows the calculation of the sample reliability, i.e. the ratio between the cumulative distribution of matched sources and the cumulative distribution of detected sources, as a function of their significance:

$$\mathrm{Rel(DET\_ML)} = \frac{\mathrm{Matched}}{\mathrm{Detected}}. \tag{4.2}$$

Highly significant sources are also correctly matched to their input counterparts, and the reliability curve is 1 at high values of DET_ML. It then falls steeply at lower significance, where the number of spurious detections starts to increase. We can set a DET_ML threshold where the reliability falls to the 99%, or 97% of its maximum value; at these thresholds, we expect to have a spurious fraction of 1% and 3%, respectively. As an example, in the full 3–24 keV band, these thresholds (DET_ML = 14.42 and DET_ML = 12.39) correspond to a probability P $\sim 5.5\times10^{-7}$ and P $\sim 4.1\times10^{-6}$, respectively, of a source being spurious. The left panel of Figure 4.5 shows the cumulative distribution of reliability for all our bands.
Once the DET_ML threshold is fixed at a given reliability, comparing how many sources are detected above the chosen threshold and matched to the input ones as a function of input flux gives the catalog completeness:

$$\mathrm{Compl}(F_{\mathrm{Input}}) = \frac{\mathrm{Detected\ above\ thr\ \&\ Matched}}{\mathrm{Input}}. \tag{4.3}$$

The right panel of Figure 4.5 shows the sample completeness at 97% reliability for all bands but the VH one, for which the curve is partially shown because it lies out of scale. Table 4.3 shows different values of completeness for each band. Rescaling the completeness curve for the maximal area of the survey in a given energy band results

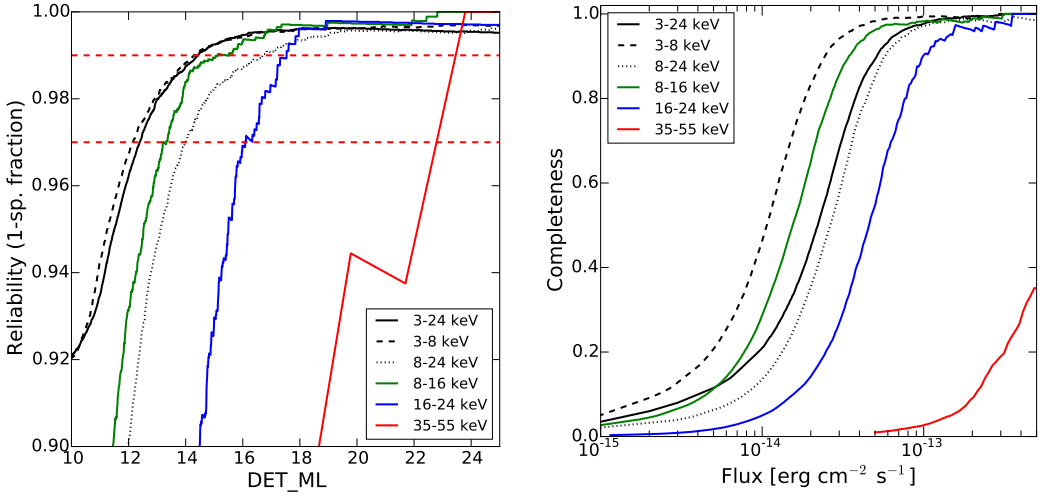

(A) (B)

FIGURE 4.5: **(A).** Cumulative reliability as a function of DET_ML. The two red dashed horizontal lines show the 99% and 97% of reliability thresholds. In black, the three canonical bands are shown as solid (F), dashed (S), and dotted (H) lines. In green, blue and red solid lines we show the H1, H2 and VH bands respectively. We note that, the harder the band, the noisier the curve, due to low statistics. **(B).** Cumulative completeness as a function of input flux, at the 97% of reliability. Colors and line styles are the same as the left panel. The completeness curve for the VH band is barely shown because it lies out of scale, which is chosen to emphasize the difference between the canonical bands instead.

in a sky coverage, or sensitivity plot. The sensitivities of our survey are shown in Figure 4.6, while Table 4.5 summarizes the results of the detection on simulations. Table 4.5 shows that the simulations predict non-detection in the VH band, while on average only 1-2 sources are expected in the H2 band and the H1 bands returns a number of sources larger, or comparable to, the H band. We also note that combining the detection catalogs coming from differently smoothed maps is advantageous only in the hard bands.

We perform aperture photometry, on the un-smoothed simulations, of detected and

TABLE 4.3: Completeness as a function of flux, 97% reliability catalog. Fluxes are in units of erg cm^{-2} s^{-1}.

Band	Completeness			
	90%	80%	50%	20%
3 – 24 keV	5.1×10^{-14}	3.8×10^{-14}	2.2×10^{-14}	9.5×10^{-15}
3 – 8 keV	2.5×10^{-14}	1.9×10^{-14}	1.0×10^{-14}	5.0×10^{-15}
8 – 24 keV	5.7×10^{-14}	4.4×10^{-14}	2.7×10^{-14}	1.4×10^{-14}
8 – 16 keV	3.5×10^{-14}	2.6×10^{-14}	1.5×10^{-14}	7.5×10^{-15}
16 – 24 keV	9.8×10^{-14}	7.7×10^{-14}	4.6×10^{-14}	2.5×10^{-14}
35 – 55 keV	1.8×10^{-12}	1.3×10^{-12}	6.3×10^{-13}	3.1×10^{-13}

TABLE 4.4: Summary of detection, UDS97. Capital letters are for sources above the threshold, while lower case letters refer to sources detected but below the threshold.

Bands	Number of sources
F + S + H	14 (21%)
F + S + h	10 (15%)
F + s + H	1 (2%)
F + S	15 (22%)
F + s	3 (4%)
f + S	4 (6%)
F + H	3 (4%)
F + h	8 (12%)
f + H	1 (2%)
F	7 (10%)
S	1 (2%)

matched sources, extracting counts in 20″ circular apertures with standard tools, such as the CIAO task `dmextract`, and converting the count rates to fluxes with an appropriate, band-dependent, conversion factor (see Table 4.5). We further apply an aperture correction, to get the total flux in each band, such that $F_{\rm corr} = F/0.32$ (see C15 for further details). A direct comparison with the fluxes input to the simulations for the F band is shown in Figure 4.7, where an excellent agreement between output and input fluxes is recovered to $F_{\rm in} \sim 5 \times 10^{-14}$ erg cm^{-2} s^{-1}, where the Eddington bias (Eddington, 1913; Wang, 2004) makes the relation flatten below $F_{\rm in} \sim 3 - 4 \times 10^{-14}$ erg cm^{-2} s^{-1}, corresponding to the flux limit of the survey at $\sim 80\%$ of completeness (see Table 4.3).

We repeat the same procedure of source detection on the data mosaics. After deblending the list of potential sources, we detect 43 unique sources above the threshold of 99% of reliability in at least one of the "canonical" F, S, and H bands. When considering the 97% reliability threshold, we detect 67 sources. We will refer to these catalogs as UDS99 and UDS97, respectively. Data mosaics in the F band, with sources detected in both catalogs are shown in Figure 4.8, while the detailed numbers of detections for each band are reported in the last two rows of Table 4.5. We note that the numbers of detections agree very well (within 1σ of the distributions; see Figure 4.9) with the simulation expectations. To maximize the statistics, we will focus on UDS97 henceforth, keeping in mind that the spurious fraction of this catalog is 3%. For homogeneity with the other NuSTAR surveys, and given the few detections in the H1, H2 and VH bands, we will also consider only the 67 sources detected in the canonical bands (of which two are expected to be spurious), while discussing the results in the new bands elsewhere (Masini et al. in prep). In Table 4.4 is shown how these 67 sources are distributed within the F, S and H bands.

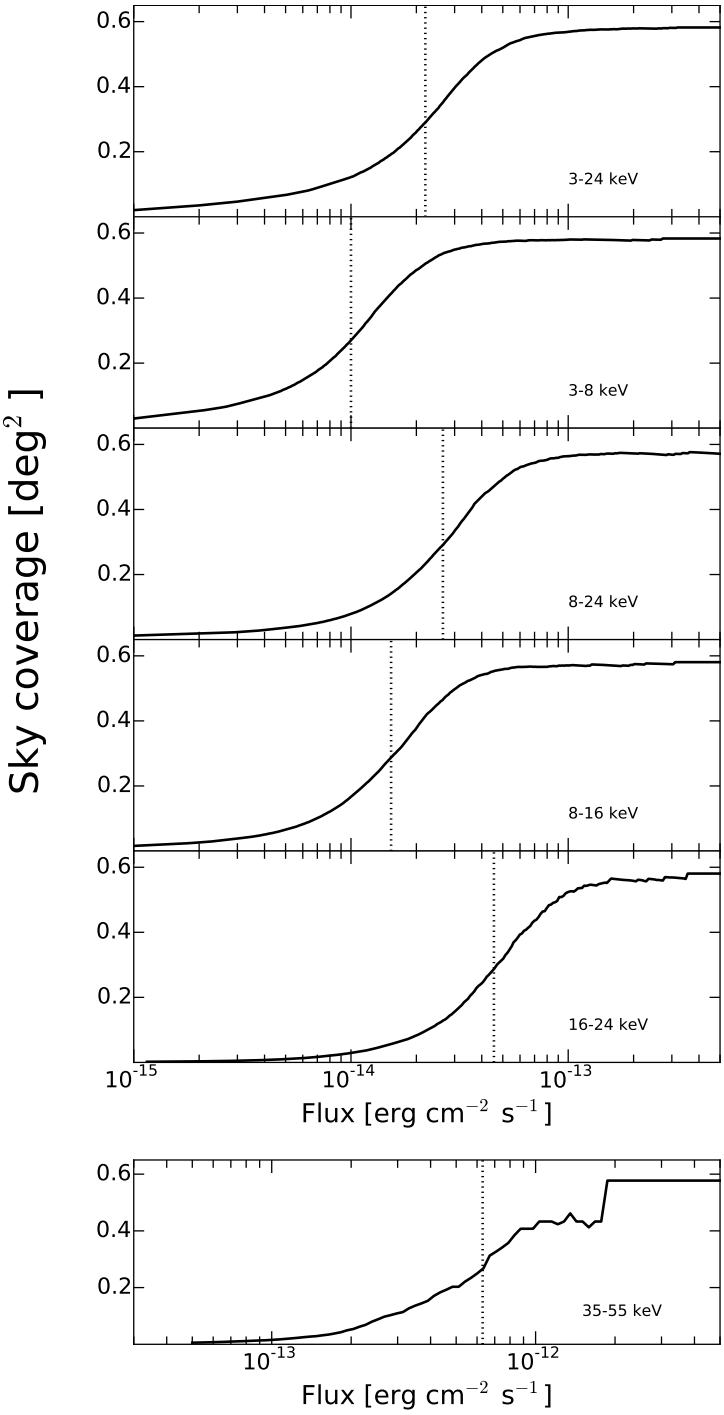

FIGURE 4.6: Sky coverage as a function of input flux for all the bands (from top to bottom: F, S, H, H1, H2, VH). In each panel, the dotted vertical line marks the half-area flux. Notice the different scale for the VH band in the bottom plot. No area is seen in the VH band at fluxes of $F_{35-55} < 10^{-13}$ erg cm^{-2} s^{-1}; very bright sources are needed in order to be detectable in this band. Furthermore, the curve is very noisy due to scarce statistics. Increasing the number of simulations would increase accordingly the number of significantly detected sources and the smoothness of the curve.

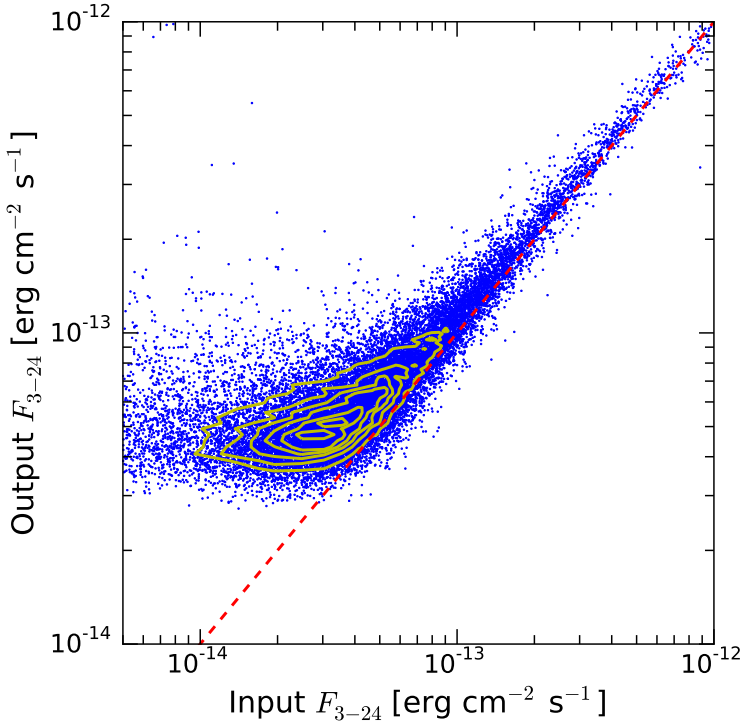

FIGURE 4.7: Results of aperture photometry on simulations, in the full band. Sources detected above the 97% reliability threshold and matched to their input counterparts are plotted as blue dots. The red dashed line is the 1:1 relation, while the yellow contours indicate where most of the points lie. The Eddington bias flattening is clearly visible for input fluxes $F_{\rm in} \lesssim 5 \times 10^{-14}$ erg cm^{-2} s^{-1}.

4.3.3 Catalog creation

We create a catalog of the 67 sources detected in the three canonical bands of UDS97, the contents of which are described in Appendix B.2. Following the same strategy adopted for the simulations, we use `dmextract` to get total and background counts from circles of 20″ of radius, from the data and background mosaics, respectively. Similarly, we extract the exposures from the exposure map mosaic in order to compute the count rates for each source and each band, which are then aperture-corrected and converted into fluxes with the appropriate conversion factors. If a source is detected below the threshold, or undetected, in a given band, 3σ upper limits are provided extracting counts at its position. For detections, 1σ uncertainties are obtained using Equations 9 and 12 of Gehrels (1986), while for non-detections we use Equation 10 of Gehrels (1986) with S = 3. The distributions of net counts and fluxes for our sources are shown in Figure 4.10.

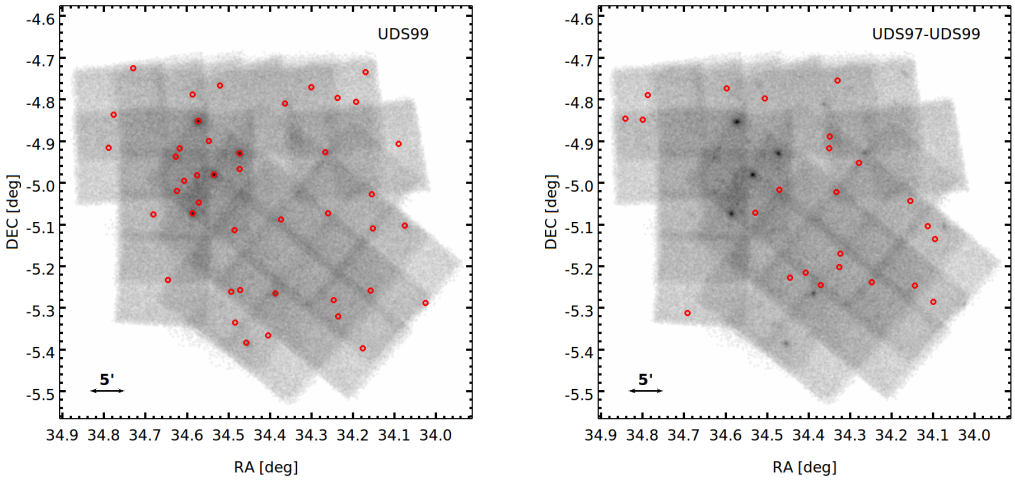

FIGURE 4.8: NuSTAR 3 – 24 keV band mosaics with the 43 sources detected in at least one of the three F, S, H bands (red circles, left panel), and with the 24 additional sources detected in the 97% reliability catalog, where we detect 67 sources in total (red circles, right panel). See Section §4.3.2 for details.

4.4 Match with XMM-*Newton* and *Chandra* catalogs

The 67 NuSTAR-detected sources are cross-matched with the Subaru XMM-*Newton* Deep Survey catalog of Ueda et al., 2008 and *Chandra* catalog of Kocevski et al. (submitted), with a matching radius of 30″. A flux cut was applied to both catalogs, excluding counterparts with a 3 – 8 keV flux more than a factor of three lower than that measured by NuSTAR.

4.4.1 XMM-*Newton*

We directly match 88% of our sources (59/67) with XMM-*Newton* sources in the SXDS catalog. We further find a counterpart at a distance of 4″ for uds7, which is falling in the tiny fraction of NuSTAR area not covered by the SXDS survey (see Figure 4.3a), in the 3XMM-DR6 catalog (Rosen et al., 2016) so that the final fraction of XMM-*Newton*-matched sources is 60 out of 67 (90%). Of the seven sources not matched, uds59 is detected above the 97% threshold in all the three F, S and H bands. It is also above the threshold in the H1 band, and is detected above the 99% reliability threshold in the F, H, H1 bands. More details on this source are provided in §4.4.1. Two other sources have an XMM-*Newton* counterpart, but with a very low 3 – 8 keV flux, while one is a blending of two SXDS sources with the same 3 – 8 keV flux slightly lower than the chosen threshold, and are then excluded by our cut. The remaining three unassociated sources could be the spurious ones expected from our chosen reliability threshold. Out of 60 matched sources, 4 have two possible XMM-*Newton* counterparts, and one has triple counterparts within 30″. We have then 55 sources with an unique XMM-*Newton* counterpart. To properly deal with multiple counterparts, we adopt the

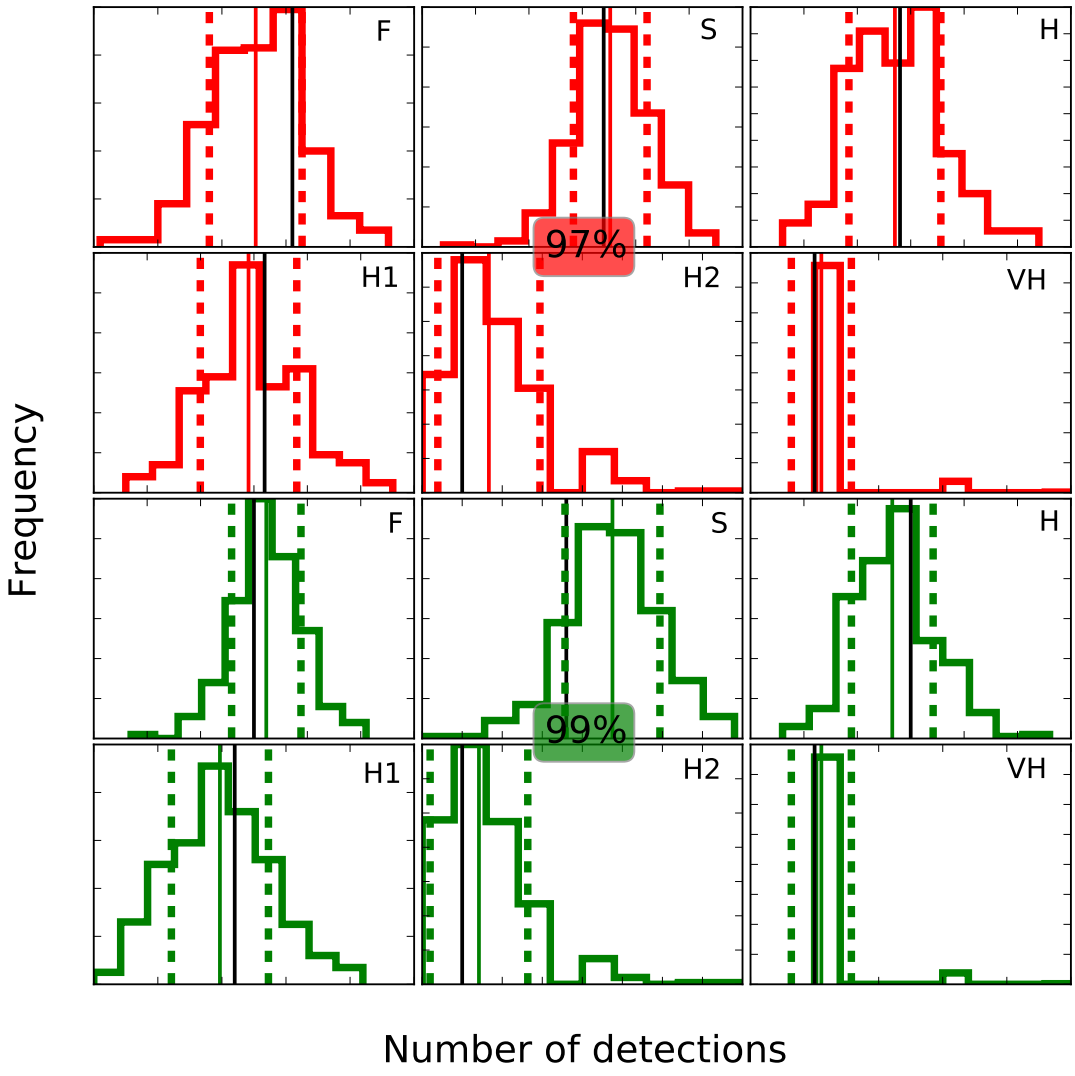

FIGURE 4.9: Distribution of detections within the simulations. The six upper panels, in red, refer to the six bands at 97% of reliability threshold. The six lower panels, in green, to the 99% of reliability. From top left to bottom right, the bands are: F, S, H, H1, H2, VH. In each panel, the dashed lines mark the $\pm 1\sigma$ interval from the average, while the black solid line marks the position of the detections in the data mosaic, which are always within $\pm 1\sigma$ from the mean of the simulations, shown by the solid red or green line. Numerical values for the average number of detections in the simulations in each band, and the number of detections in the data mosaics, are explicitly addressed in the last four rows of Table 4.5.

following strategy: if the closest of the counterparts within 30″ has also the highest "hard" (i.e., 3 – 8 keV) flux, it is considered as the primary counterpart of the NuSTAR source. Otherwise, it is considered blended and is then excluded from the following analysis. With this prescription, we add two sources in which the closest XMM-*Newton* counterpart is also the brightest, having a total of 57 unique matches.

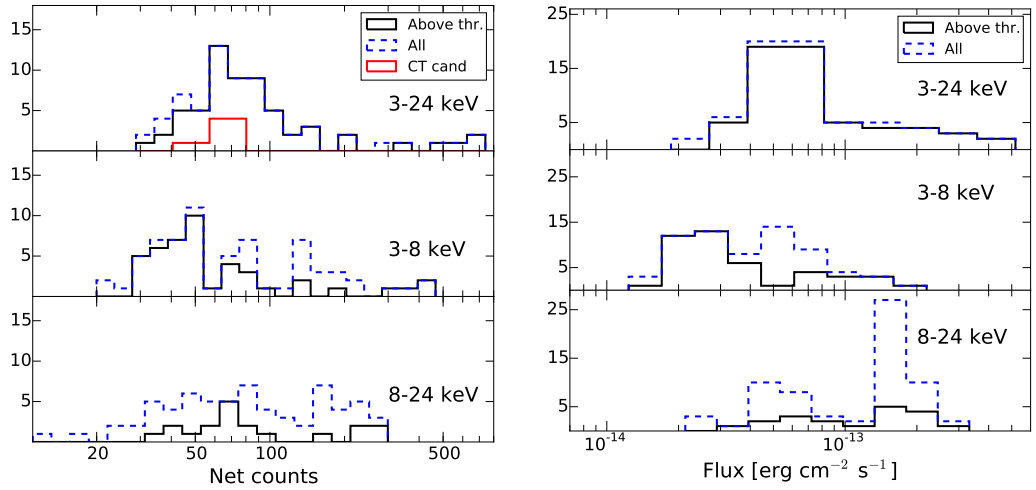

FIGURE 4.10: Net counts (left panel) and fluxes (right panel) distribution in the F band (top panel), S band (middle panel) and H band (bottom panel) for all the sources (blue dashed histogram), and sources above the threshold only (black solid histogram). Note that the "All" histograms (dashed blue lines) include upper limits. The red histogram in the top panel of the net counts distribution shows the net counts distribution in the F band for our CT candidates (see §4.5.1).

The case of uds59

As previously mentioned (§4.4), uds59 is detected by NuSTAR above the 97% reliability thresholds in 4 out of 6 bands (F, S, H, H1). We note that it is present also in the UDS99 catalog, although it is under-threshold in the S band. Detected with 82 net counts in the F band, uds59 is located in a part of the mosaic where only XMM-*Newton* coverage is available, and is not matched to any SXDS source. At its position, SDSS maps show the presence of a group of galaxies, which is indeed detected as a galaxy cluster in the CFHTLS 4 Wide Fields Galaxy Clusters catalog (Durret et al., 2011) at $z_{\rm phot} \sim 0.45$. Moreover, two galaxies of the group are detected by *WISE* (Wright et al., 2010) and are $4.7''$ and $11.5''$ away from the NuSTAR position, as shown in Figure 4.11. Since uds59 is then a strong candidate to be a newly discovered source, we extract its NuSTAR X-ray spectrum, assuming the redshift of the group ($z_{\rm phot} = 0.45$) and we fit the spectrum with a simple Galactic-absorbed power law. The returned photon index is quite flat, implying that the source is obscured ($\Gamma = 0.68^{+0.53}_{-0.54}$), consistent with the non-detection by XMM-*Newton*. Adding a screen along the line of sight (through a zwabs model) and fixing $\Gamma = 1.9$, we get a good fit (CSTAT/DOF=200/235) with the source being heavily obscured ($N_{\rm H} = 8.2^{+6.1}_{-4.2} \times 10^{23}$ cm^{-2}). A very similar result is obtained using a MYTorus model (Murphy and Yaqoob, 2009, CSTAT/DOF=202/235, $N_{\rm H} = 7.1^{+5.5}_{-3.8} \times 10^{23}$ cm^{-2}). We can also use these models to calculate the flux in the three canonical bands, and we have:

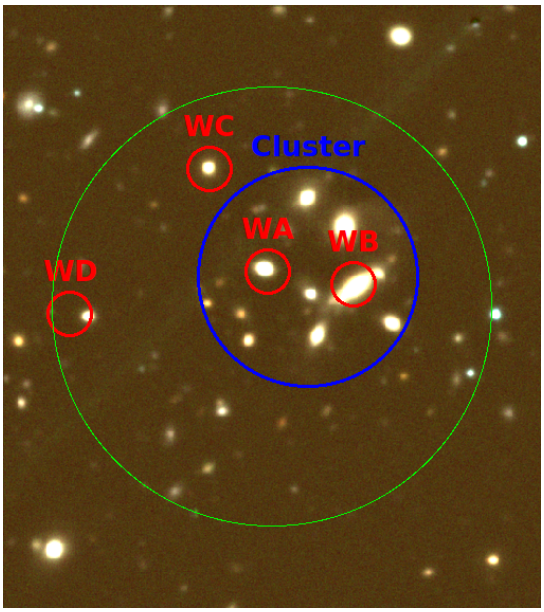

FIGURE 4.11: JHK composite image from the UKIDSS-UDS DR11 (Almaini et al., in prep) of uds59 region. The green circle has a radius of 30″ and marks the NuSTAR position. The blue circle marks the cluster detected by (Durret et al., 2011), while the four *WISE* sources within 30″ of the NuSTAR position are marked with red circles and capital letters in order of growing distance.

$$F_{3-24} = 1.2^{+0.3}_{-0.3} \times 10^{-13} \text{ erg cm}^{-2}\text{s}^{-1},$$
$$F_{3-8} = 2.3^{+1.0}_{-0.8} \times 10^{-14} \text{ erg cm}^{-2}\text{s}^{-1},$$
$$F_{8-24} = 9.6^{+2.9}_{-4.7} \times 10^{-14} \text{ erg cm}^{-2}\text{s}^{-1}.$$

We can compare the soft band flux with the upper limit obtained from the 0.2-12 keV XMM-*Newton* mosaic. Extracting the total number of counts in a circular region of 20″ of radius and using the average vignetting-corrected exposure at the same position, we get a count rate of 1.16×10^{-2} cts s^{-1} for the PN, which translates into a predicted $F_{3-8} \sim 9.2 \times 10^{-15}$ erg cm^{-2} s^{-1}. A combination of intrinsic obscuration and low-exposure coverage (the effective exposure time at the position of the source is only 9.8 ks for the PN) is likely responsible for the non-detection by XMM-*Newton*.

4.4.2 *Chandra*

As ∼ 30% of the NuSTAR UDS field is not covered by *Chandra*, only 41 sources have *Chandra* coverage, and 40 of them are matched. Notably, uds45, the only one missing a *Chandra* counterpart, is not matched in the XMM-*Newton* catalog either, and is then a strong candidate to be one of the two expected spurious sources in the catalog. Out of 40 *Chandra*-matched sources, 5 have a double counterpart and 2 have a triplet in the *Chandra* catalog. As done for XMM-*Newton*, each case is evaluated and we add

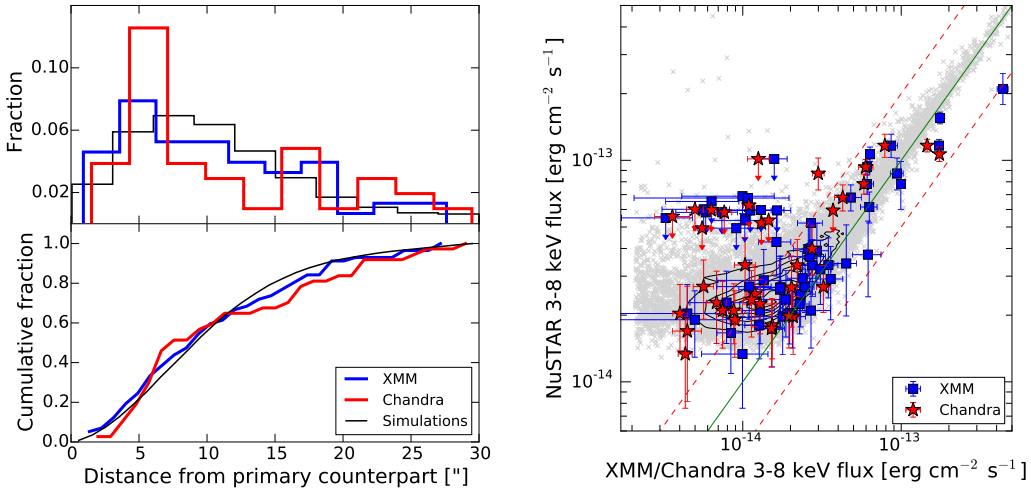

(A) (B)

FIGURE 4.12: **(A).**(Top) Distribution of separation between our NuSTAR sources and XMM-*Newton* (blue solid line) and *Chandra* (red solid line) counterparts, compared with the simulations in the S band. (Bottom) Cumulatives of the distributions shown in the top panel. More than 50% of our sources are matched within 10″, and 80% within 20″. Colors as in the top panel. **(B).** NuSTAR 3 – 8 keV fluxes as a function of XMM-*Newton* (blue squares) and *Chandra* (red stars) 3 – 8 keV fluxes. Upper limits on NuSTAR fluxes are represented as downward arrows. The green solid line is the 1:1 relation, while the red dashed lines are a factor of two displaced from it. At low fluxes, the Eddington bias makes the points deviate from the 1:1 relation. The gray crosses and the black contours on the background are the expectation from the simulations in the 3 – 8 keV band (see Figure 4.7).

another 4 counterparts to the 33 unique matches, for a total of 37 unique matches. The distribution of separations between our NuSTAR sources and their low-energy counterparts, and its cumulative, are shown in Figure 4.12a; 60% of the sources are matched within 10″, while 80 – 90% are matched within 20″. We note that the distribution peaks are consistent with the simulated source distribution in the 3 – 8 keV band. These fractions are comparable with the ones found by C15 taking into account the secondary counterparts, while slightly lower than the separations with the primary counterparts, but considering a higher reliability sample. In Figure 4.12b we also compare NuSTAR, XMM-*Newton* and *Chandra* fluxes in the 3 – 8 keV band converting the XMM-*Newton* 4.5 – 10 keV count rates and the 2 – 10 keV *Chandra* fluxes to 3 – 8 keV fluxes assuming a $\Gamma = 1.8$ power law.

4.4.3 Optical counterparts

Akiyama et al., 2015 provide optical counterparts for a large fraction of the catalog of Ueda et al., 2008, and an optical spectrum is also available for the counterpart of uds7, from the BOSS survey (Dawson et al., 2013). We have redshifts for 56 sources (84%), of which 48 are spectroscopic and 8 are photometric. We split these 56 redshifts into

broad line AGN (BLAGN) and narrow line AGN (NLAGN). The category is directly defined in the Akiyama et al., 2015 catalog for spectroscopic redshifts based on a FWHM threshold of 1000 km s^{-1}, while for photometric redshifts only the "QSO" or "GAL" templates are specified. We consider then objects best-fitted by a "QSO" template as BLAGN, and objects best-fitted by a "GAL" template as NLAGN. Out of 56 redshifts, we have 28 BLAGN and 28 NLAGN. The median redshift of our sample is $\langle z \rangle = 1.092$, while $\langle z_{\rm BLAGN} \rangle = 1.272$ and $\langle z_{\rm NLAGN} \rangle = 1.003$. In Figure 4.13a we show the redshift distribution of the sample, while in Figure 4.13b we show how our sources compare with other NuSTAR Extragalactic Surveys like the COSMOS, ECDFS and Serendipitous ones in the $L_{10-40} - z$ plane. This luminosity is computed from the F band flux without correcting for absorption. We notice that, while the NuSTAR Serendipitous survey (Lansbury et al., 2017b) reaches slightly higher redshifts, we detect the highest redshift source among tiered NuSTAR deep surveys (uds67 at $z_{\rm spec} = 3.128$). This may be due to the chosen reliability threshold, which allows fainter sources to be detected.

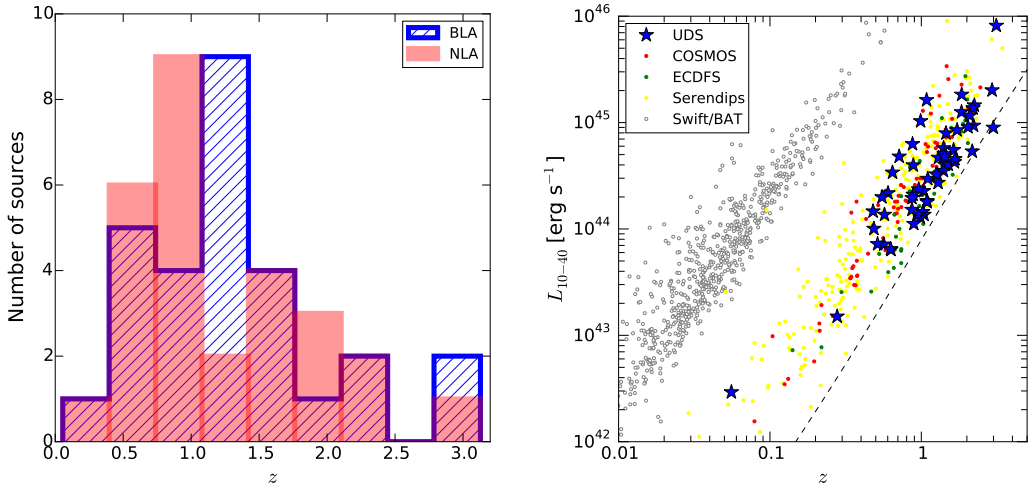

(A) (B)

FIGURE 4.13: **(A).** Redshift distribution for the 56 sources with an optical counterpart, divided into broad line AGN (blue hatched histogram) and narrow line AGN (red histogram). **(B).** 10-40 keV luminosity (not corrected for absorption, although we expect the role of obscuration to be negligible at these energies) as a function of redshift for the NuSTAR surveys. Blue stars are the UDS97 sources. The NuSTAR COSMOS sample (Civano et al., 2015) is indicated by red dots, green dots indicate the NuSTAR ECDFS catalog (Mullaney et al., 2015), yellow dots the 40-month NuSTAR Serendipitous sample (Lansbury et al., 2017b) and gray dots the 70-month *Swift*-BAT catalog (Baumgartner et al., 2013). The dashed line is the flux limit of the UDS survey at 50% of completeness.

4.5 Extraction of X-ray spectra, obscured and CT fraction

We exploit the available redshift information performing a broadband (0.5-24 keV) X-ray spectral analysis of all the 56 sources in our UDS97 catalog with an optical counterpart.

We extract FPMA and FPMB spectra with the NuSTARDAS task `nuproducts`, while NuSTAR background spectra are produced using the `nuskybgd` software. Following the methodology of Zappacosta et al. (submitted), for any source and pointing in which it is found, we extract the number of counts, background counts and average exposure in the F band for a range of extraction radii. This allows us to get a signal-to-noise ratio (SNR) profile as a function of extraction radius for each pointing and each FPM; the single SNR(r) profiles are then averaged together, weighted with the exposure time at the position of the source in every observation. Finally, the extraction radius for FPMA and FPMB is chosen as the one maximizing the average SNR profile and the net counts at the same time. Single data products are summed together using standard tools like `mathpha`, `addarf` and `addrmf`, where the ARFs and RMFs are weighted using the fraction of total counts their respective observation is contributing.

Chandra observations of the UDS field are downloaded from the public archive and reduced through the standard pipeline, using the `chandra_repro`, `specextract` and `combine_spectra` tasks within the CIAO software (version 4.9, CALDB version 4.7.3). Circular extraction regions with a radius of $2''$ are used, while we employ annuli centered on the source position with an internal radius of $3''$ and external radius of $10''$ to extract background spectra.

The XMM-*Newton* observations of the UDS field are downloaded and reduced using the Science Analysis Subsystem (SAS; version 16.0.0) tasks `epproc/emproc` and filtering every event file for high background time intervals. PN data are always preferred to MOS data when available (i.e., when the source is not falling on a PN gap), while MOS1 and MOS2 spectra are summed together. We use the SAS `evselect` task to define optimized extraction radii for sources, while background spectra are extracted from nearby circular regions on the same chips as the sources. Finally, we use the SAS task `epicspeccombine` to produce summed sources and background spectra, ancillary and response files. Final spectral products are grouped to a minimum of 3 counts/bin with the `grppha` tool for each telescope.

We then fit the NuSTAR spectra jointly with the XMM-*Newton* and, when available, *Chandra* ones, adopting the Cash statistic (Cash, 1979). The adopted spectral model is composed of a primary power-law emission with a fixed photon index $\Gamma = 1.9$, taking into account the possible photoelectric absorption and Compton scattering, plus allowing for up to a few percent of the primary power law to be scattered into the line of sight. The whole nuclear emission is then absorbed by a Galactic column density ($N_{\rm H}^{\rm gal} = 2.08 \times 10^{20}$ cm^{-2}, Kalberla et al., 2005), and cross-calibration between instruments is accounted for using a multiplicative factor. In XSPEC notation, our baseline model is given by `const*pha*(plcabs+const*zpow)`. The resulting column density

distribution for UDS97 is shown in Figure 4.14 as the orange, hatched histogram. Considering the UDS99 sample, the shape of the distribution is the same within the uncertainties on each bin. Such uncertainties are computed with a bootstrapping algorithm, resampling 10^4 times our histogram. In particular, for each iteration, a new $N_{\rm H}$ distribution is created from the observed one, randomly picking values from the measured array. A single value can be picked multiple times. We then have 10^4 realizations of our column density distribution, and the 16th and 84th percentiles of the resulting distribution in each bin are used to get the 1σ uncertainty on each bin value. The obscured ($N_{\rm H} > 10^{22}$ cm^{-2}) fraction from this first-order analysis is $63 \pm 7\%$, and the CT ($N_{\rm H} > 10^{24}$ cm^{-2}) fraction is $5 \pm 4\%$ (3/56), where the uncertainties are also computed with the bootstrapping algorithm. In the same way as before, we can compute the obscured and CT fraction for each realization, getting a distribution of 10^4 obscured and CT fractions from which the 16th and 84th percentiles are used to get the 1σ uncertainty.

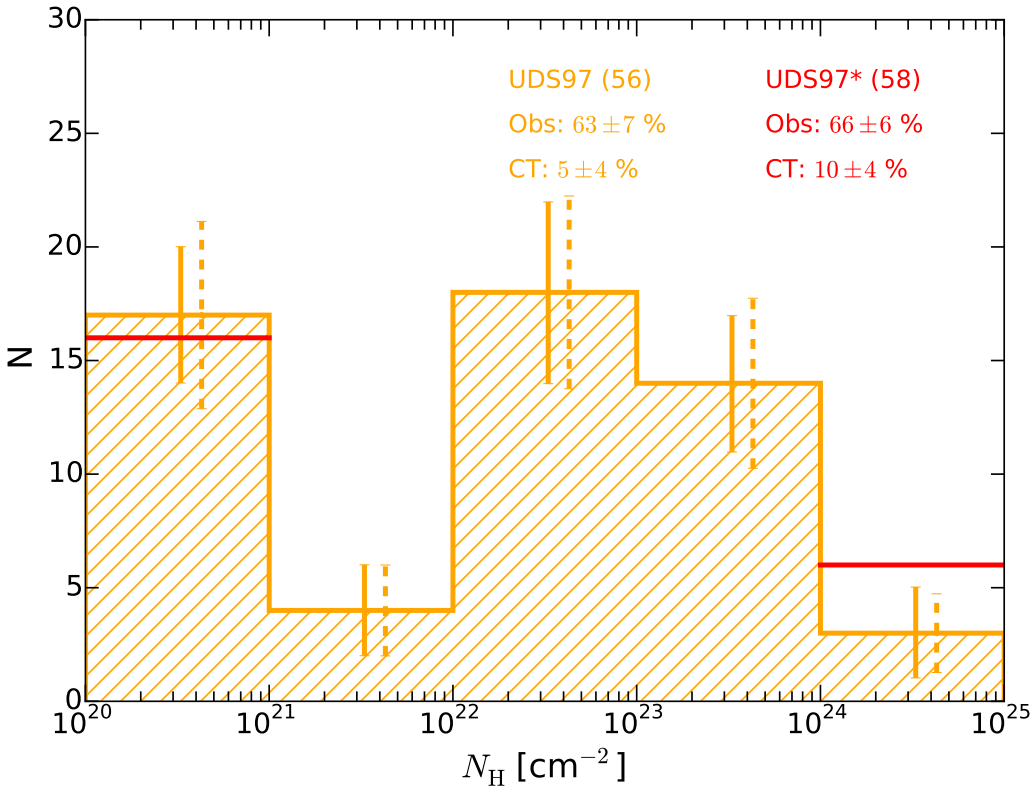

FIGURE 4.14: Column density distribution for the NuSTAR-detected sources in our sample, above the 97% threshold of reliability. The solid errorbars are calculated with a bootstrapping algorithm, while the dashed ones mark the square root of the bin value. The red thick bins mark the resulting distribution when taking into account the refined analysis for the CT candidates (see §4.5.1).

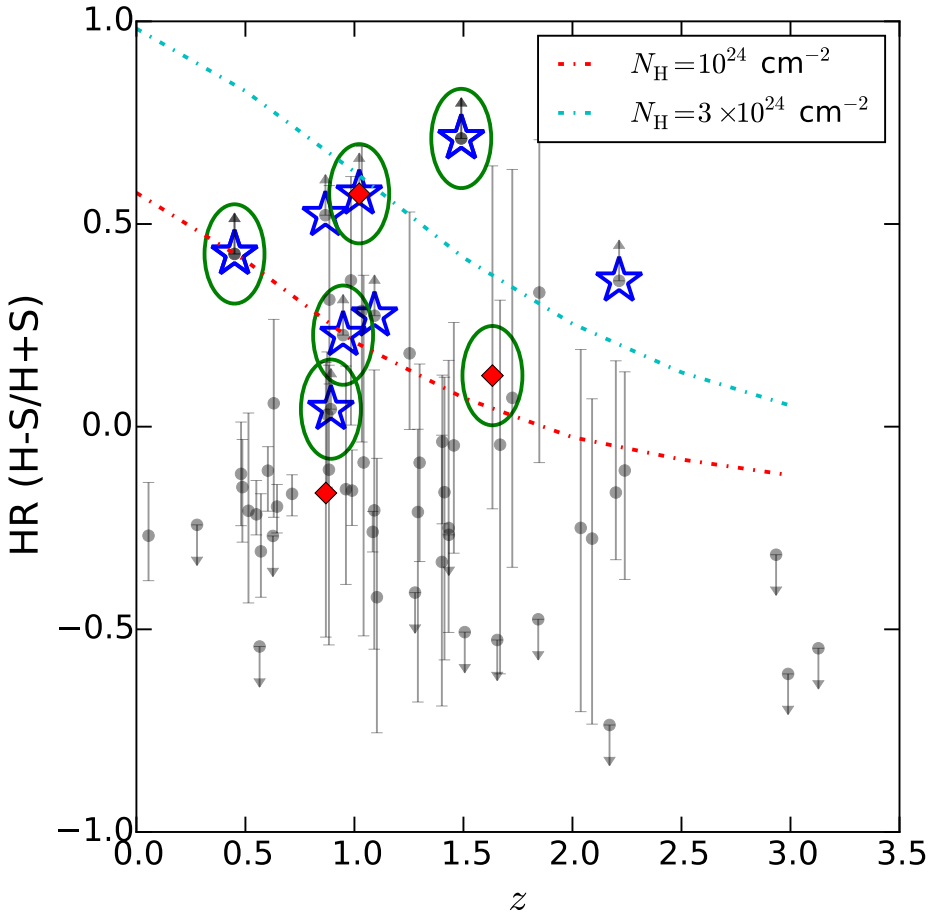

FIGURE 4.15: Distribution of our 58 sources in the hardness ratio (HR)-redshift plane. Lower limits on HR, i.e. heavily obscured candidates, are labeled with blue stars, while sources defined as CT from our broad-band spectral analysis are marked by red filled diamonds. Note that only six out of eight lower limits actually have a secure redshift association; two more sources have been added after the broadband spectral analysis (see Section 4.5.1). The green ellipses mark the seven CT sources resulting from our refined spectral analysis. The red and cyan dotted-dashed curves are the HR(z) curves computed with a marginal and mildly Compton-thick MYTorus model (Murphy and Yaqoob, 2009), respectively. As discussed in the text, out of the combined sample of 10 CT candidates (blue stars and red diamonds), 6 are confirmed to have CT obscuration, 5 of which have $N_{\rm H} > 10^{24}$ cm^{-2} at the 90% confidence interval.

4.5.1 Combining HR and broadband spectral analysis diagnostic: a refined analysis

Additional constraints on the obscuration properties of our sample come from the analysis of the hardness ratio (HR), defined as

$$\mathrm{HR} = \frac{\mathrm{H} - \mathrm{S}}{\mathrm{H} + \mathrm{S}}. \tag{4.4}$$

We then calculate the HR for the whole UDS97 sample using the Bayesian Estimator for Hardness Ratios (BEHR, Park et al., 2006), which uses the total and background counts in the S and H NuSTAR bands, and compare the results with the ones coming from the broadband spectral analysis. At fixed N_{H}, the HR changes with redshift, and as such is not possible to infer a unique estimate on the N_{H} without a redshift. Nonetheless, sources which show a very hard spectrum (HR $\sim$ 1) are good candidates to be highly obscured objects, independently of their redshift (Lansbury et al., 2014; Lansbury et al., 2015).

In Figure 4.15, the HR is plotted against the redshift of our sources, where eight sources have a lower limit on the HR: uds13, uds30, uds42, uds46, uds47, uds48, uds58, and uds63 (blue stars in Figure 4.15). In the same figure, sources found to be CT from the spectral analysis with the baseline model (uds20, uds30, uds66) are indicated by the red filled diamonds. We notice that uds47 and uds63 are lacking a robust redshift association, and as such are not included in the broadband spectral analysis of Section §4.5, but have a best-fit HR = 1, indicating high obscuration. We then adopt a redshift estimate for both of them, using the iron line redshift in one case, and choosing the most probable counterpart in the other (see Appendix B.1), and plot both in Figure 4.15. The two subsets of sources, three selected from our broadband spectral analysis, and eight selected from the HR analysis, have only one source in common.

We first test if the low number of net counts could bias our HR measurements. In Figure 4.16a the HR is plotted against the NuSTAR full band net counts. While a tail of very bright sources seems to show soft HR, there is no clear trend between the number of counts and the spectral shape, indicating that the HR analysis is not biased towards, or against, a particular level of obscuration when dealing with very few ($\sim$ tens) counts. Moreover, only 2 out of the 10 CT candidates have less than 60 net counts in the $3-24$ keV NuSTAR band (red histogram in Figure 4.10a).

Secondly, we test if the HR is effectively tracing the obscuration of our sample, plotting the HR coming from BEHR as a function of the column density N_{H} as measured with `plcabs`. As it can be seen from Figure 4.16b, there is a qualitative concordance between our sample and the trend expected from models, since higher column densities are generally measured for objects with higher HR; moreover, the HR becomes sensitive to a column density change only for $N_{\mathrm{H}} > 10^{23}$ cm^{-2}. Once assessed the complementarity of the two approaches, the two subsamples together represent a set of 10 CT candidates, the properties of which are summarized in Table 4.6. It is interesting

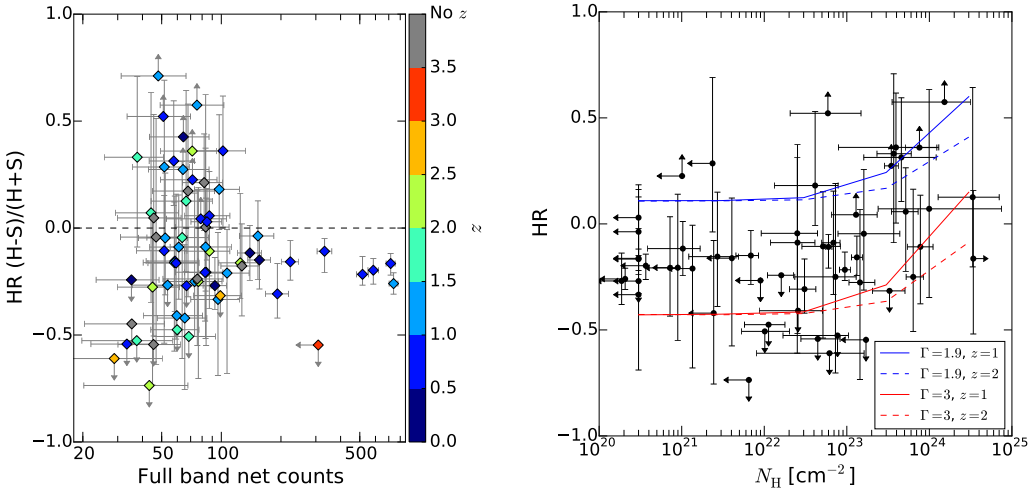

(A) (B)

FIGURE 4.16: **(A).** NuSTAR hardness ratio of the whole UDS97 sample as a function of full band (3 – 24 keV) net counts. Points are color-coded with their redshift, where gray points are those without a secure redshift association. A tail of very bright sources at $z < 1$ is seen with soft HR, while no clear trend is evident at low counts. The dashed horizontal line marks HR= 0. **(B).** Hardness Ratio as a function of obscuring column density, as measured by our baseline model with `plcabs` for the UDS97 sample, compared with the trend expected from a `plcabs` model with $\Gamma = 1.9$ (blue lines) or an unrealistic $\Gamma = 3$ (red lines), at both $z = 1$ (solid) and $z = 2$ (dashed). The models predict, at a fixed Γ, the relation to be flat till $N_{\rm H} \sim 10^{23}$ cm^{-2}, and an increasing HR for increasing $N_{\rm H}$ at higher column densities.

to perform a refined X-ray spectral analysis of them all, using a more appropriate spectral model like MYTorus (Murphy and Yaqoob, 2009). As already extensively discussed (see Section §2.1), this model is more appropriate than `plcabs` when dealing with high column densities ($N_{\rm H} \sim 10^{24}$ cm^{-2}), and self-consistently takes into account Compton scattering and line fluorescence. In this second broadband spectral analysis, we then employ a "default" MYTorus model, with the line of sight angle set to 90 degrees, plus a scattered power-law, similarly to what was done before. In XSPEC notation, the model is `const*pha*(zpow*MYTZ+MYTS+MYTL+const*zpow)`, where the different components of the MYTorus model stand for the absorption, scattering and line fluorescence ones, respectively. Spectra with best-fit models and residuals are shown in Figure 4.17, while best-fit values for some parameters are provided in Table B.1. Details on some sources are discussed in Appendix B.1. After the spectral analysis with the MYTorus model, 5 out of 8 objects having a lower limit on the HR are confirmed to be CT (uds30, uds46, uds47, uds48, uds63). The other three (uds13, uds42, uds58) have $10^{23} < N_{\rm H} < 10^{24}$ cm^{-2}, showing in any case high levels of obscuration and confirming that the HR is a good way to select CT candidates. On the other hand, 2 out of 3 sources selected from the first spectral analysis are confirmed to be CT (uds20 and uds30), while the remaining one (uds66) shows Compton-thin obscuration. Figure 4.18 shows how the column density of the 10 CT candidates changes before and after the refined spectral

analysis.

4.6 Discussion on the CT fraction

Based on the results of the MYTorus spectral fitting, the UDS97 sample presents five sources with a "robust" CT obscuration (i.e., the Compton-thin solution is excluded at a confidence level of 90%), and one marginally CT source (i.e., with the best-fit $N_{\rm H}$ above 10^{24} cm^{-2}, but with uncertainties that allow a less obscured solution at the 90% of confidence level). At face value, we then have 6 CT sources in a sample of 58 sources, implying a CT fraction of (10 ± 4)%, where the uncertainties are computed with the bootstrapping procedure explained in §4.5. The CT subsample is shown in Figure 4.14 as the red thick bin and marked by green ellipses in the left panel of Figure 4.15.
Interestingly, the CT fraction would have been dramatically lower in the more conservative sample, UDS99, since only one of the 6 CT sources would have been reliably detected (uds48). On the other hand, the CT fraction is unlikely to be much higher than ~ 10%, although few sources in Figure 4.15 have an HR consistent with a CT obscuration and have not been selected by our criteria. The whole UDS97 sample is composed of 67 sources, 9 of which are missing in Figure 4.14; none of the 9 sources not considered in our analysis (due to multiple, or no counterparts at all) shows a lower limit on the HR. The CT fraction obtained in the UDS field is in agreement with the tentative estimate of C15 based on the Hardness Ratio (HR) distribution of the NuSTAR COSMOS sample, which is $13\% - 20\%$, with only one source being confirmed CT from the spectral analysis. It is interesting to note that, if focusing on the UDS99 sample with 43 sources (39 with optical counterpart), and exploiting the HR$-z$ plane as a first-order diagnostic tool to get an estimate of the CT fraction, we would get a fraction of ~ 15% (i.e., 6 over 39 sources with an HR consistent with having $N_{\rm H} > 10^{24}$ cm^{-2}), although we showed that, formally, only one of our CT sources would have been detected in the UDS99 sample. This number, even if remarkably consistent with the spectral analysis result, shows how a robust spectral analysis is required to draw firmer conclusions on the CT fraction.
The CT fraction measured by NuSTAR in the UDS field (Figure 4.19) shows a broad consistency of our results with the predictions of different population synthesis models of the CXB (Gilli, Comastri, and Hasinger, 2007; Treister, Urry, and Virani, 2009; Draper and Ballantyne, 2010; Akylas et al., 2012). Together with the results reported in the figure, we notice that the UDS and Serendipitous surveys seem to be probing two different, but complementary, regimes of parameter space with their two different samples. Indeed, Lansbury et al. (2017a) find that the low redshift ($z < 0.07$) CT fraction is unexpectedly high (~ 30%) compared to model predictions, while the UDS sample covers much higher redshifts, since our CT candidates are almost all between $1 < z < 2$, and broadly agrees with model predictions (for $0 < z < 3$). On the other hand, Zappacosta et al. (submitted) present a thorough and homogeneous broadband ($0.5 - 24$ keV) spectral analysis of 63 NuSTAR-detected sources with $S_{8-24} > 7 \times 10^{-14}$ erg cm^{-2} s^{-1}

TABLE 4.5: Summary of detections on simulations and real data. The first (second) row is the average number of sources detected in the 10″ (20″) smoothed maps. The third row is the average number of sources in the merged catalog, cleaned from duplicates. The fourth row is the average number of sources detected and matched (after deblending) to input sources. The fifth and sixth rows display the DET_ML thresholds at the 99% and 97% of reliability. The seventh and eighth rows show the average number of sources expected to be above the 99% and 97% reliability thresholds, from the simulations. The ninth and tenth rows report the effective number of sources detected above the 99% and 97% reliability thresholds, respectively. The last two rows report the conversion factors from count rates to fluxes used in the paper, from WebPIMMS (https://heasarc.gsfc.nasa.gov/cgi-bin/Tools/w3pimms/w3pimms.pl), and flux scaling factors with respect to the F band flux, obtained assuming a power law spectrum with $\Gamma = 1.8$.

Simulations	Bands					
	3 – 24 keV	3 – 8 keV	8 – 24 keV	8 – 16 keV	16 – 24 keV	35 – 55 keV
10” smoothed maps	115	97	68	64	33	29
20” smoothed maps	100	84	57	54	22	15
Combined, no duplicates	115	96	76	70	43	37
Matched to input	90 (78%)	76 (79%)	48 (63%)	45 (64%)	14 (33%)	7 (19%)
DET_ML(99%) Thr.	14.42	14.28	16.69	15.13	17.54	23.55
DET_ML(97%) Thr.	12.39	12.15	14.00	13.23	16.09	23.00
DET_ML > DET_ML(99%)	42	34	13	15	1	0
DET_ML > DET_ML(97%)	55	45	19	19	2	0
Real data						
DET_ML > DET_ML(99%)	40	28	15	16	1	0
DET_ML > DET_ML(97%)	61	44	19	21	1	0
Conversion factors [erg cm^{-2}]	4.86×10^{-11}	3.39×10^{-11}	7.08×10^{-11}	5.17×10^{-11}	1.62×10^{-10}	1.07×10^{-9}
Scale factors	1.	0.42	0.58	0.35	0.23	0.30

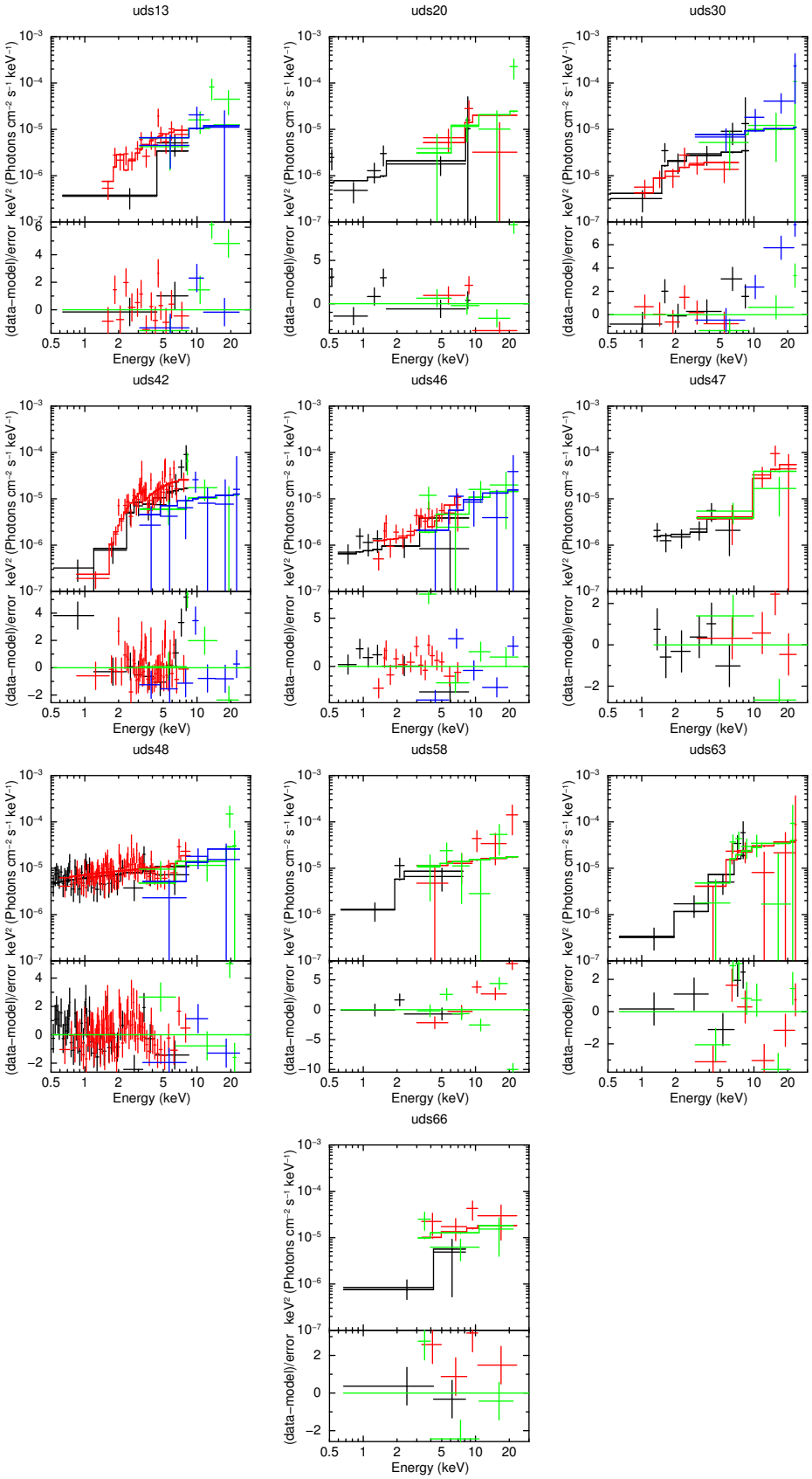

FIGURE 4.17: Broadband *vFv* spectra of the 10 CT candidates selected from the combined spectral analysis and HR diagnostic. The best-fitting MYTorus model is shown for each source, together with the residuals in the bottom panels. Data have been rebinned for plotting purposes. When three colors are present, black refers to either XMM-*Newton* or *Chandra*, red and green to NuSTAR's FPMA and FPMB. When four colors are present, black refers to XMM-*Newton*, red to *Chandra*, green and blue to NuSTAR's FPMA and FPMB.

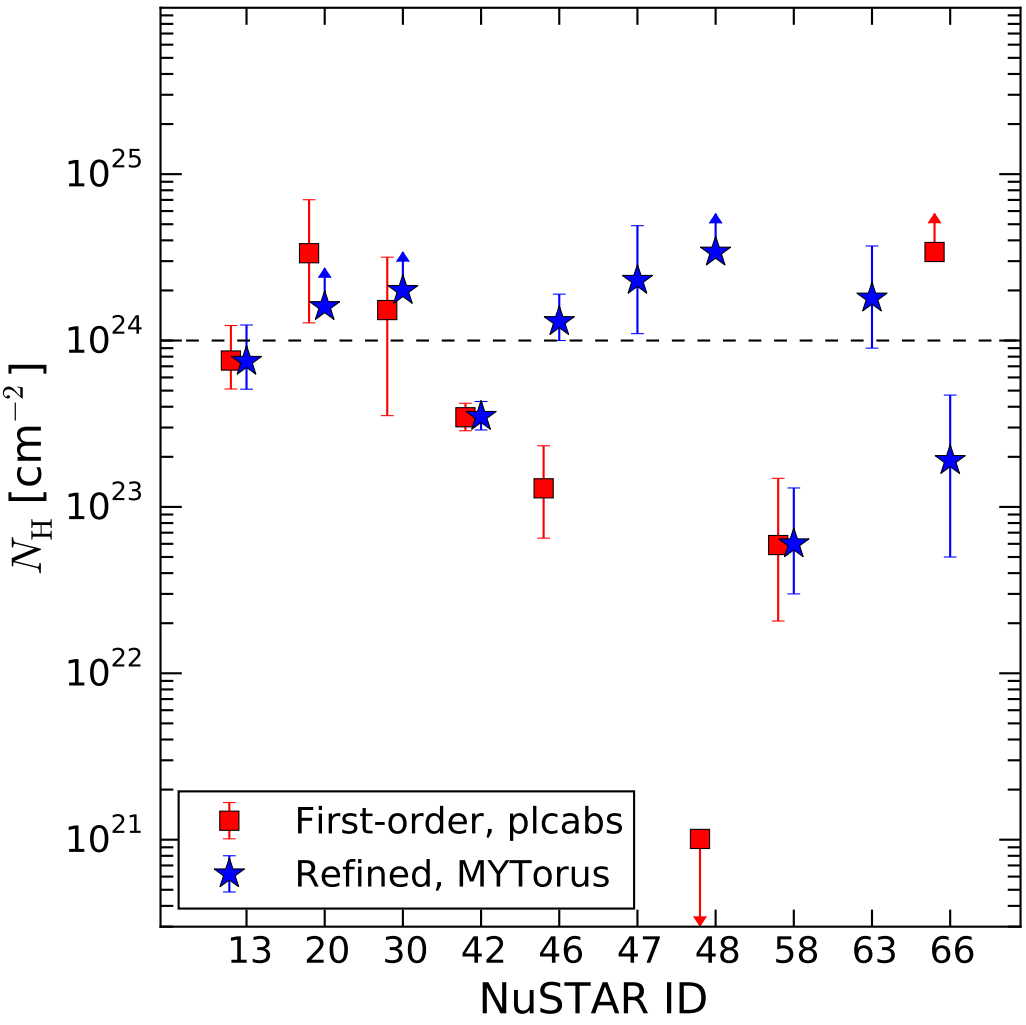

FIGURE 4.18: Distribution of column densities $N_{\rm H}$ before and after the spectral analysis with the MYTorus model. Results from the `plcabs` baseline model fitting and the refined analysis (adopting the MYTorus model) are marked as red squares and blue stars, respectively. The dashed horizontal line marks the CT regime. We note that uds47 and uds63 are not fitted by our first-order analysis with `plcabs`, as lacking a redshift; nonetheless, we are able to fit for the redshift in one case, and use the most likely one in the other. See Appendix B for further details.

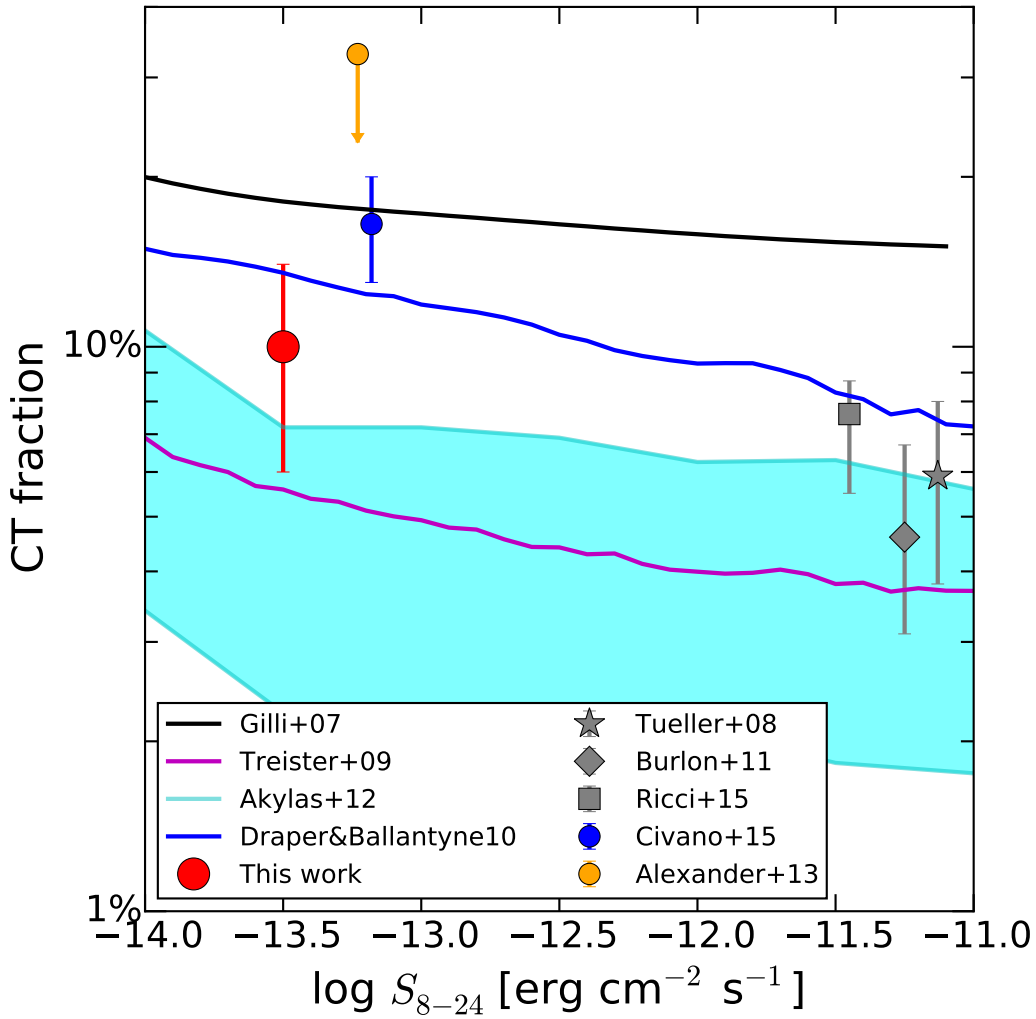

FIGURE 4.19: Compton-thick fraction as a function of 8−24 keV flux as measured by NuSTAR in the UDS field in the redshift range $0 < z < 3$ (red point). The gray star, diamond and square symbols represent the measurements of *Swift*-BAT by Tueller et al. (2008), Burlon et al. (2011) and Ricci et al. (2015), respectively. The orange point refers to results from the NuSTAR Serendipitous survey (Alexander et al., 2013), while the blue point is the measurement from Civano et al. (2015). Black, blue and magenta solid lines refer to the Gilli, Comastri, and Hasinger (2007), Draper and Ballantyne (2010) and Treister, Urry, and Virani (2009) models, respectively, while the cyan area refers to the Akylas et al. (2012) model with a range of intrinsic CT fractions between 15% – 50%.

TABLE 4.6: Summary of properties of the 10 CT candidates. Column (1): name of the source. Column (2): bands in which the source has been detected, either above (capital letter) or below (lowercase) the reliability threshold. Column (3): method of selection of the source, either by having a lower limit on its HR (labeled HR) or having a CT column density with the first-order `plcabs` analysis (labeled PL). Column (4): Source HR. Columns (5)-(6): number of XMM-*Newton* counterparts and separation from the primary one (if any). Columns (7)-(8): number of *Chandra* counterparts and separation from the primary one (if any). Columns (9)-(10): source redshift and redshift type.

Name	Detected in	Selected	HR	N_{XMM}	Sep_{XMM} ["]	N_{Cha}	Sep_{Cha} ["]	z	z Type
(1)	(2)	(3)	(4)	(5)	(6)	(7)	(8)	(9)	(10)
uds13	F+h	HR	$1.00^{+u}_{-0.64}$	1	9.3	1	6.2	2.2	Photo-z
uds20	F	PL	$0.12^{+0.52}_{-0.33}$	1	10.8	0	-	1.633	Spec-z
uds30	F+H	PL,HR	$1.00^{+u}_{-0.42}$	1	19.2	0	-	1.022	Spec-z
uds42	F+h	HR	$1.00^{+u}_{-0.73}$	1	7.3	1	6.9	1.092	Spec-z
uds46	F	HR	$0.21^{+0.79}_{-0.17}$	1	27.6	1	6.2	0.892	Spec-z
uds47	F+h	HR	$1.00^{+u}_{-0.57}$	0	-	1	26.2	~0.45	X-ray[a]
uds48	F+h	HR	$0.38^{+0.62}_{-0.15}$	1	12.0	1	11.5	0.948	Spec-z
uds58	F+h	HR	$1.00^{+u}_{-0.48}$	1	12.4	0	-	0.867	Spec-z
uds63[b]	f+H	HR	$1.00^{+u}_{-0.29}$	3	12.2	0	-	1.5	Photo-z
uds66	F+S+h	PL	$-0.16^{+0.32}_{-0.36}$	1	3.7	0	-	0.869	Spec-z

[a] This source has a prominent iron Kα line in its *Chandra* X$-ray$ spectrum, from which we determined its redshift. See B.1.1 for further details.

[b] This source has three XMM-*Newton* counterparts; here, we chose to show the closest one. See B.1.3 for further details.

and $\langle z \rangle = 0.58$, finding an observed CT fraction between $1\% - 8\%$, which is consistent with our result. However, Table B.1 shows that our sources have full band fluxes lower than their H band cut, implying an even lower H band flux for our CT candidates (a factor of 7-10 with respect to the sources selected in Zappacosta et al., submitted). In this respect, we are probing, also in this case, two different, and possibly complementary, redshift and flux ranges.

4.6.1 Iron Kα

A prominent iron Kα line (with an equivalent width, EW, ~ 1 keV) in the X-ray spectrum of an AGN at 6.4 keV (rest-frame) is usually considered as a strong indicator for CT obscuration. While such a feature is commonly observed in X-ray spectra of local AGN (e.g., Masini et al., 2016; Boorman et al., 2016, but see Gandhi et al., 2017 for a case of an anomalously weak iron Kα line in a local CT AGN, already discussed in this Thesis in Section 3.3.2), the poor statistics afflicting deep surveys ($\sim$ tens of counts) prevents robust emission lines to be firmly detected, and stacking is often required to reveal such features (Falocco et al., 2013; Lanzuisi et al., 2015).
In our sample of 10 CT candidates, an iron Kα line is expected to be detected, provided the spectra have a sufficient SNR. A careful estimation of each line EW requires many assumptions on the exact redshift of the source, its uncertainty, and its type (photometric or spectroscopic), which is beyond the scope of this Chapter. As an example, uds13 shows a clear line feature in its *Chandra* spectrum. The assumed redshift is photometric (~ 2.2), and the line EW is rather small (EW < 0.25 keV); however, shifting the line to a slightly higher redshift ($z \sim 2.4$) the EW increases substantially (EW $= 0.35^{+0.37}_{-0.27}$ keV), despite being statistically consistent with the value found before. From a simple visual inspection of the spectrum, and considering the redshift of each source, a line feature consistent with a redshifted iron Kα can be seen in at least 4 sources (uds13, uds42, uds46, uds47). In general, the median redshift of our sample ($1 < z < 2$) causes the line to shift at the edge of the NuSTAR band ($E < 3-4$ keV), making the soft energy data crucial to detect such a feature. The line is generally better detected by *Chandra* rather than XMM-*Newton*, due to the *Chandra* lower background, which maximizes the net counts for each source. Indeed, those sources where an iron Kα line is not detected, are missing *Chandra* coverage, while XMM-*Newton* collects few tens of net counts in its full band ($\sim 35 - 40$, for uds20, uds30, and uds66).

4.7 Summary of this Chapter

In this Chapter we presented a NuSTAR survey of the UKIDSS-UDS field, showing how NuSTAR can contribute to the search for CT AGN in the relatively distant Universe ($1 < z < 2$). The survey, consisting of 35 observations performed in two separate passes on the field, for a total observing time of 1.75 Ms over an area of 0.58 deg^2, allowed us to measure the CT fraction combining standard diagnostic, such as the hardness ratio evaluation (often adopted where poor SNR spectra are available), and

broadband X-ray spectroscopy.

In particular, we detected 43 sources above the 99% threshold of reliability (i.e., UDS99), and 67 sources above the 97% threshold of reliability (i.e., UDS97). We have explored, for the first time, the feasibility of a detection in three new bands, splitting the hard $8-24$ keV band into two narrower bands (H1, $8-16$ keV; H2, $16-24$ keV), and exploiting the broad-band capabilities of NuSTAR looking for sources in the very-hard (VH, $35-55$ keV) band. Nonetheless, the catalog is restricted to the canonical F, S and H bands for homogeneity with the previous NuSTAR Extragalactic Surveys, and we focused on the UDS97 catalog, where the expected spurious fraction is 3%. In order to have a precise view of the obscuration properties of our sample, we combined all the available information coming from a broadband spectral analysis and hardness ratio diagnostic to include all the possible heavily obscured candidates. We then focused on a subsample of 10 CT ($N_{\rm H} > 10^{24}$ cm^{-2}) candidates using a more appropriate toroidal spectral model, of which 6 are confirmed to be CT.

The NuSTAR UDS sample shows a majority of obscured sources (> 60% with $N_{\rm H} > 10^{22}$ cm^{-2}) and an observed fraction of Compton-thick sources of (10 ± 4)%. This fraction is in agreement with findings from other NuSTAR surveys, and in broad consistency with population synthesis models of the CXB. This value is indeed within $1-2\sigma$ from predictions of a bunch of models, differing substantially in the intrinsic CT fraction and Compton reflection hump parameter adopted, like the Gilli, Comastri, and Hasinger (2007), Treister, Urry, and Virani (2009) and Akylas et al. (2012) models, or considering other parameters like the Eddington ratio distribution of CT AGN (Draper and Ballantyne, 2010). Nonetheless, the current uncertainties do not allow to firmly distinguish between different models.

About half of our CT candidates show an iron Kα line. The absence of such a feature in the other half could be due a combined effect of redshift (line always outside of the NuSTAR energy band) and to the scarce photon statistics, mainly in cases where *Chandra* data are not available. Notably, only one of the 6 CT sources in the UDS field would have been detected if we adopted the more conservative UDS99 sample, dramatically lowering the observed CT fraction. This demonstrates the capability of NuSTAR to unveil the so-far elusive highly obscured AGN population, once the spurious fraction and blended lower-energy counterparts are addressed.

Chapter 5

Conclusions and future perspectives

In this last Chapter, the final remarks of this Thesis are given. First a brief summary of the project, and then the future perspectives, with both the on-going and future planned steps, are described.

5.1 Final summary

This Thesis summarizes three years of PhD project focused on the NuSTAR view of obscured AGN. The first Chapter reviewed why obscured (mainly CT) AGN are important for the basic AGN research, for the study of the Cosmic X-ray Background (CXB), and for the broader picture of galaxy evolution. In particular, since NuSTAR operates in the hard X-ray band ($3-80$ keV), it was discussed what information can be extracted from X-ray spectroscopy of all types of AGN, showing the principal components contributing to, and shaping, the X-ray emission from an accreting supermassive black hole. Then, a local-to-distant approach was adopted, following also the chronological development of the PhD project.

The second and third Chapters presented a study of local ($z < 0.03$), highly obscured AGN as seen through the NuSTAR mirrors. The selection took advantage of a known phenomenological relationship between water maser emission with a particular disk geometry, and CT obscuration. First, the discussion focused on this biased subsample of local AGN to estimate a robust CT fraction, and an analytical model to predict the obscuring column based on the radial extent of the maser disk was developed. Secondly, some useful applications of this sample which comes with exquisite X-ray data thanks to NuSTAR, and black hole masses thanks to VLBI studies of the sub-pc maser clumps dynamics, were shown. A spin-off of this project was focused on a single maser source study, which is variable in the X-ray band. Taking advantage of a NuSTAR snapshot, a discussion on its long-term light curve and the constraints on the scenarios invoked to explain the source variability was presented.

NuSTAR observed also other highly obscured sources, both stable and variable in time. Such variability and complexity of spectral shapes of local obscured AGN makes very challenging to find them during the peak of cosmic accretion ($1 \lesssim z \lesssim 2$). Usually, the

best way to study the Universe at this epoch is by performing deep X-ray surveys, able to detect hundreds and thousands of AGN. Then, in the last Chapter the NuSTAR deep survey of the UKIDSS-UDS field was presented, trying to directly resolve the obscured and CT AGN contributing to the peak of the CXB. An accurate observed CT fraction in the field was measured, and compared to other NuSTAR surveys and theoretical models.

5.2 Future perspectives

The perspectives of this PhD project are multiple, both regarding megamasers and deep X-ray surveys.

5.2.1 Megamasers

I have recently obtained 50 ks of NuSTAR time to observe a newly discovered disk megamaser in NGC5765b. This face-on spiral galaxy is gravitationally interacting with its companion, NGC5765a, and egde-on late-type galaxy. While the megamaser is detected in a short *Chandra* observation, the latter one probably hosts an AGN, but only the megamaser is going to be detected by NuSTAR. The system is very interesting, being also the first case of megamaser disk in a close merger. Mergers are an active topic of research, since they are believed to play a significant role in triggering obscured AGN accretion and shaping galaxy evolution (as extensively discussed in the Chapter 1, and throughout this Thesis). I will also test our analytical model (presented in §2.7) which predicts the $N_{\rm H}$ to be heavily CT, based on the megamaser disk radial extent.
A second project involving disk megamasers is exploring why megamaser disks are so rare, and how improving the target selection can boost their detection efficiency in radio surveys. Reversing the problem, once the intrinsic incidence of megamaser disks in Seyfert 2 AGN is assessed, constraints on the average covering factor of the torus can be drawn (Masini and Comastri, in prep).

5.2.2 X-ray surveys with current and future missions

As explained in Chapter 4, in the NuSTAR survey of the UDS field the hard (8 – 24 keV) band was split in two sub-bands (i.e., 8 – 16 keV and 16 – 24 keV), since sources significantly detected in the 16 – 24 keV band are those directly contributing to the peak of the CXB, and their detection and space density assessment is crucial to understand the implications. Also, the broadband capabilities of NuSTAR were exploited, performing detection in the 35 – 55 keV band. As shown in §4.3.2 and in Table 4.5, results in the UDS field were not promising in such bands, especially in the hardest bands (consistently with the simulations performed). Then, an already started follow-up project is to combine results in different fields, to increase statistics. I have performed data reduction, simulation runs, and source detection in 8 – 16 keV, 16 – 24 keV, and 35 – 55 keV bands, both in the COSMOS and ECDFS fields, in order to aggregate the results

with those coming from the UDS field (Masini et al., in prep).
Finally, I am going to exploit the superior *Chandra* angular resolution to study the bulk of the growth of SMBHs over a wide and contiguous area in the XBoötes field (Murray et al., 2005). The Chandra Deep Wide-Field Survey will be the next generation legacy survey of *Chandra*, with a limiting $0.5-2$ keV flux of $F_{0.5-2} \sim 10^{-15}$ erg cm^{-2} s^{-1} over an area of ~ 6 deg^2, with a few thousands of AGN predicted to be detected. Such a large number of sources on a wide area will allow unprecedented accurate studies of multi-wavelength AGN evolution, of AGN-AGN and AGN-galaxy clustering, and of the relation between the AGN and the dark matter halos in which they reside. These future studies will pave the way for the upcoming new facilities that will start a new era of multi-wavelength AGN research, such as the *extended ROentgen Survey with an Imaging Telescope Array* (eROSITA) and the *Advanced Telescope for High Energy Astrophysics* (Athena).

Appendix A

Mrk1210: analysis of the 2004 *Chandra* observation

A.1 Analysis of the *Chandra* 2004 (C0) observation

We reduced the *Chandra* data and produced a grouped spectrum using the CIAO standard `chandra_repro` and `specextract` tasks. The source counts were extracted from a $3''-$radius circular region, while the background was extracted from four $10''$ circular regions. Soft X-ray emission below 3 keV is clearly present in the total spectrum (Figure A.1), and was fitted, following Risaliti et al. (2010), with an `apec+zpowerlw` model. The hard X-ray part of the spectrum was fitted with our baseline model, Equation (3.1). The fitting parameters are reported in Table A.1. We note that the results are consistent with the NuSTAR observation presented in Chapter 3.

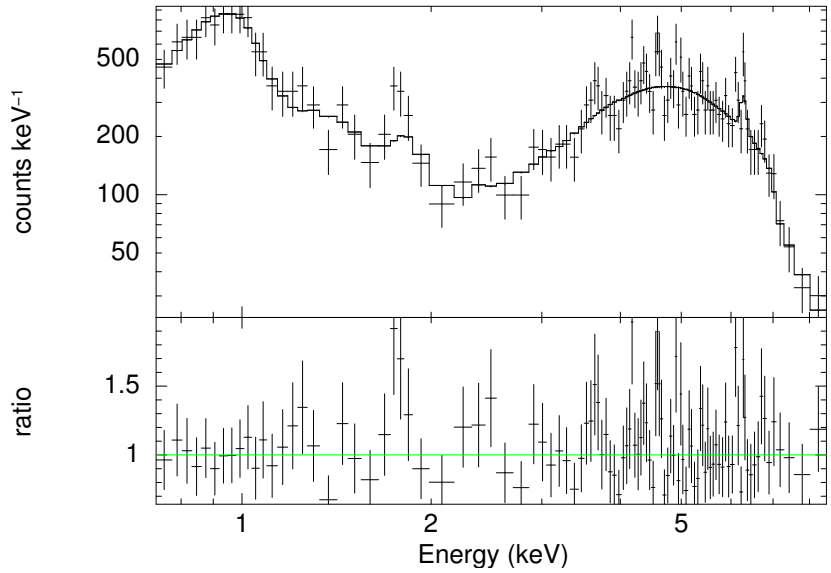

FIGURE A.1: Best fit and data/model ratio to the 2004 *Chandra* spectrum of Mrk 1210.

TABLE A.1: C0 observation; best fitting parameters.

Parameter	Value
χ^2/ν	83/95
Hard component	
Γ	$1.56^{+0.58}_{-0.63}$
$N_{\rm H}$ [cm^{-2}]	$2.7^{+0.8}_{-1.0} \times 10^{23}$
Norm transmitted comp @1 keV [ph cm^{-2} s^{-1} keV^{-1}]	$2.2^{+6.9}_{-1.7} \times 10^{-3}$
Norm reflection comp @1 keV [ph cm^{-2} s^{-1} keV^{-1}]	$1.2^{+1.0}_{-1.0} \times 10^{-2}$
Line Energy [keV]	$6.36^{+0.08}_{-0.21}$
EW Line [eV]	84^{+74}_{-68}
Norm line component (flux) [ph cm^{-2} s^{-1}]	$1.2^{+1.0}_{-1.0} \times 10^{-5}$
Soft component	
kT [keV]	$1.02^{+0.16}_{-0.09}$
Norm apec @1 keV [ph cm^{-2} s^{-1} keV^{-1}]	$4.3^{+1.4}_{-1.3} \times 10^{-5}$
$\Gamma_{\rm s}$	3.0^{+u}_{-l}
Norm zpowerlw @1 keV [ph cm^{-2} s^{-1} keV^{-1}]	$2.9^{+2.9}_{-2.9} \times 10^{-5}$
F_{2-10} [erg cm^{-2} s^{-1}]	7.6×10^{-12}

Appendix B

The NuSTAR UKIDSS-UDS survey; further details

B.1 Details of the refined spectral analysis

B.1.1 uds47

This source has an HR ~ 1, as calculated with BEHR (Park et al., 2006). Since it lacks an XMM-*Newton* counterpart (due to the adopted cut in flux during the matching), but has one *Chandra* counterpart, we fit the joint NuSTAR + *Chandra* spectrum. The latter one shows a prominent line feature, consistent with being Fe Kα redshifted at $z = 0.45^{+0.17}_{-0.11}$ as obtained with the MYTorus model. Applying an *ad hoc* model like `zwabs*zpow+zgauss`, the redshift can be constrained to be $z = 0.47^{+0.06}_{-0.08}$.

B.1.2 uds48

This source is selected to be a CT candidate based on its NuSTAR HR. However, the *Chandra* and XMM-*Newton* data are perfect power laws without any sign of obscuration aside from the Galactic one, along the line of sight. Two formally indistinguishable scenarios are possible: one in which the source is totally unobscured, and one in which NuSTAR captures the Compton reflection hump while XMM-*Newton* and *Chandra* detect only the scattered power law emission. We show, even in this case, how the CSTAT varies as a function of column density parameter in Figure B.1 From the figure, the CT solution seems to be preferred by the data, since the two scenarios have the same number of spectral bins, degrees of freedom and free parameters in the fit. From this, it follows that also the Akaike information criterion (AIC, Akaike, 1974) prefers the CT solution. We note that this plot has been obtained adopting a `plcabs` model, since the MYTorus one prevents $N_{\rm H} < 10^{22}$ cm^{-2}.

TABLE B.1: Results of the refined broadband spectral analysis for the 10 CT candidates.

Name	z	CSTAT/DOF	$N_{\rm H}$ [10^{24} cm^{-2}]	$f_{\rm s}$ [%]	$F^{\rm obs}_{3-24}$ [erg cm^{-2} s^{-1}]	$L^{\rm int}_{2-10}$ [erg s^{-1}]	$L^{\rm int}_{10-40}$ [erg s^{-1}]
uds13	2.214	134/126	$0.75^{+0.49}_{-0.24}$	$1.8^{+6.7}_{-l}$	3.1×10^{-14}	4.4×10^{44}	1.1×10^{45}
uds20	1.633	152/134	>1.6	$3.7^{+u}_{-3.4}$	4.4×10^{-14}	1.0×10^{45}	2.0×10^{45}
uds30	1.022	116/126	>2	3^{+1}_{-1}	4.1×10^{-14}	5.4×10^{44}	5.4×10^{44}
uds42	1.092	267/288	$0.35^{+0.08}_{-0.06}$	$0.8^{+0.9}_{-0.7}$	3.0×10^{-14}	1.1×10^{44}	1.8×10^{44}
uds46	0.892	221/195	$1.3^{+0.6}_{-0.3}$	5*	2.8×10^{-14}	1.3×10^{44}	1.9×10^{44}
uds47	$0.45^{+0.17}_{-0.11}$[a]	95/85	$2.3^{+2.6}_{-1.2}$	$1.4^{+u}_{-1.3}$	6.9×10^{-14}	1.9×10^{44}	2.4×10^{44}
uds48	0.948	278/321	>3.4	5*	4.6×10^{-14}	7.3×10^{44}	1.1×10^{45}
uds58	0.867	195/192	$0.06^{+0.07}_{-0.03}$	5*	4.8×10^{-14}	8.4×10^{43}	1.3×10^{44}
uds63	1.49[b]	192/190	$1.8^{+1.9}_{-0.9}$	$0.9^{3.2}_{-0.7}$	7.0×10^{-14}	1.5×10^{45}	2.0×10^{45}
uds66	0.869	73/67	$0.19^{+0.28}_{-0.14}$	0.6*	5.0×10^{-14}	1.1×10^{44}	1.6×10^{44}

† This column refers to the fraction of primary power law scattered in the soft X−rays. We imposed a maximum value of 5% in our fits, since scattered fractions of few percent are often seen in local Sy2 AGN (Bianchi and Guainazzi, 2007). Numerical values with an asterisk are unconstrained by the fit.
[a] We used the Fe Kα line to fit for the redshift of this source. See §B.1.1.
[b] We chose the redshift of the closest XMM-*Newton* counterpart to the NuSTAR position (See §B.1.3). The source is still CT even fitting the NUSTAR spectrum with the second XMM-*Newton* counterpart at $z_2 = 0.568$.

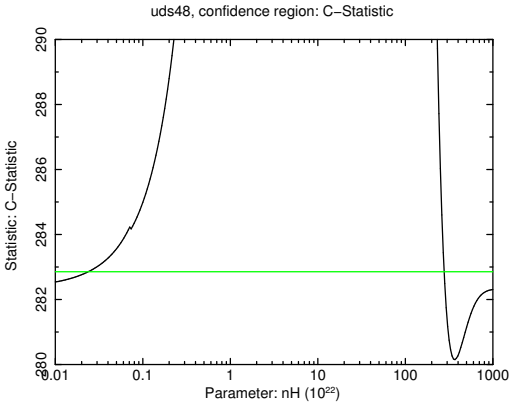

FIGURE B.1: C-Statistic parameter as a function of the column density for uds48, fitting NuSTAR + XMM-*Newton* + *Chandra* data. The green horizontal line is the limiting CSTAT for the 90% confidence level uncertainty. Statistically acceptable solutions are those with a CSTAT parameter below the green line. The model adopted is `plcabs`, because MYTorus does not allow $N_{\rm H} < 10^{22}$ cm^{-2}. An unobscured solution is statistically indistinguishable from a CT one; the best fit, however, is obtained with $N_{\rm H} > 3\times10^{24}$ cm^{-2} and we assume this source to be a CT source.

B.1.3 uds63

Similarly to the case of uds47, uds63 lacks a redshift since it is associated to three XMM-*Newton* sources within 30″. The farthest one is also the faintest at 4.5−10 keV, while the other two are formally a blending, as defined in the text, lying at $z_1 = 1.49$ (photometric) and $z_2 = 0.568$ (spectroscopic). Since we are not able to decide which of the two is contributing most to the NuSTAR flux, we extracted both spectra and fitted them separately with the NuSTAR data. In both cases the fit returned a Compton−thick column density, and in the analysis we chose to show the one with the closest source, which is also the best fit, adopting the redshift $z_1 = 1.49$.

B.1.4 uds66

This source is one of the CT sources identified by our broadband spectral analysis. Nonetheless, the fit returns, together with an extremely high column density, also a suspiciously high cross-calibration constant FPMA/EPIC-PN ∼ 22. When fitted with MYTorus, this solution is disfavored against a Compton-thin solution ($N_{\rm H} \sim 2 \times 10^{23}$ cm^{-2}), with cross-calibration constant of FPMA/EPIC-PN $= 2.2^{+4.5}_{-1.3}$.

B.2 Catalog description

The electronic version of the catalog which is going to be published (Masini et al., submitted), contains the following information. An example of the first two sources is given in Tables B.2 and B.3.

Column 1 NuSTAR source name, following the standard IAU convention, with the prefix “NuSTAR”.

Column 2 Source ID.

Columns 3-4 RA and DEC of the source, in the J2000 coordinate system.

Column 5 3–24 keV band deblended DET_ML (0 if undetected).

Column 6 3–24 keV band vignetting-corrected exposure time at the position of the source.

Column 7 3–24 keV band total counts in a 20″-radius circular aperture.

Column 8 3–24 keV band deblended background counts in a 20″-radius circular aperture.

Column 9 3–24 keV band net counts (3σ upper limit if undetected).

Columns 10-11 3–24 keV band positive and negative count error computed using Gehrels statistic (0 if undetected).

Column 12 3–24 keV band count rate in a 20″-radius circular aperture (3σ upper limit if undetected).

Column 13 3–24 keV band aperture-corrected flux (3σ upper limit if undetected).

Columns 14-15 3–24 keV band positive and negative flux error (-99 if undetected).

Column 16 3–8 keV band deblended DET_ML (0 if undetected).

Column 17 3–8 keV band vignetting-corrected exposure time at the position of the source.

Column 18 3–8 keV band total counts in a 20″-radius circular aperture.

Column 19 3–8 keV band deblended background counts in a 20″-radius circular aperture.

Column 20 3–8 keV band net counts (3σ upper limit if undetected).

Columns 21-22 3–8 keV band positive and negative count error computed using Gehrels statistic (0 if undetected).

Column 23 3–8 keV band count rate in a 20″-radius circular aperture (3σ upper limit if undetected).

Column 24 3–8 keV band aperture-corrected flux (3σ upper limit if undetected).

Columns 25-16 3–8 keV band positive and negative flux error (-99 if undetected).

Column 27 8–24 keV band deblended DET_ML (0 if undetected).

Column 28 8–24 keV band vignetting-corrected exposure time at the position of the source.

Column 29 8–24 keV band total counts in a 20″-radius circular aperture.

Column 30 8–24 keV band deblended background counts in a 20″-radius circular aperture.

Column 31 8–24 keV band net counts (3σ upper limit if undetected).

Columns 32-33 8–24 keV band positive and negative count error computed using Gehrels statistic (0 if undetected).

Column 34 8–24 keV band count rate in a 20″-radius circular aperture (3σ upper limit if undetected).

Column 35 8–24 keV band aperture-corrected flux (3σ upper limit if undetected).

Columns 36-37 8–24 keV band positive and negative flux error (-99 if undetected).

Column 38 Hardness ratio computed with BEHR (Park et al., 2006).

Columns 39-40 Hardness Ratio lower and upper bound.

Column 41 XMM-*Newton* primary counterpart in 30″ from the SXDS catalog (Ueda et al., 2008) (-99 if no counterpart is found).

Columns 42-43 RA and DEC of the counterpart, J2000 coordinate system (-99 if no counterpart is found).

Column 44 XMM-*Newton* ultrasoft band (0.3–0.5 keV) count rate (-99 if no counterpart is found).

Column 45 XMM-*Newton* ultrasoft band (0.3–0.5 keV) count rate uncertainty (1σ) (-99 if no counterpart is found).

Column 46 XMM-*Newton* soft band (0.5–2.0 keV) count rate (-99 if no counterpart is found).

Column 47 XMM-*Newton* soft band (0.5–2.0 keV) count rate uncertainty (1σ) (-99 if no counterpart is found).

Column 48 XMM-*Newton* medium band (2.0–4.5 keV) count rate (-99 if no counterpart is found).

Column 49 XMM-*Newton* medium band (2.0–4.5 keV) count rate uncertainty (1σ) (-99 if no counterpart is found).

Column 50 XMM-*Newton* ultrahard band (4.5–10.0 keV) count rate (-99 if no counterpart is found).

Column 51 XMM-*Newton* ultrahard band (4.5–10.0 keV) count rate uncertainty (1σ) (-99 if no counterpart is found).

Column 52 Distance between the NuSTAR source and XMM-*Newton* primary counterpart (-99 if no counterpart is found).

Column 53 Number of XMM-*Newton* counterparts found within 30″.

Column 54 *Chandra* primary counterpart in 30″ from the XUDS catalog (Kocevski et al. submitted) (-99 if no counterpart is found).

Columns 55-56 RA and DEC of the counterpart, J2000 coordinate system (-99 if no counterpart is found).

Column 57 *Chandra* soft band (0.5–2.0 keV) flux (-99 if no counterpart is found).

Columns 58-59 *Chandra* soft band (0.5–2.0 keV) flux positive and negative errors (-99 if no counterpart is found).

Column 60 *Chandra* hard band (2.0–10.0 keV) flux (-99 if no counterpart is found).

Columns 61-62 *Chandra* hard band (2.0–10.0 keV) flux positive and negative errors (-99 if no counterpart is found).

Column 63 *Chandra* ultrahard band (5.0–10.0 keV) flux (-99 if no counterpart is found).

Columns 64-65 *Chandra* ultrahard band (5.0–10.0 keV) flux positive and negative errors (-99 if no counterpart is found).

Column 66 Distance between the NuSTAR source and *Chandra* primary counterpart (-99 if no counterpart is found).

Column 67 Number of *Chandra* counterparts found within $30''$.

Columns 68-69 RA and DEC of optical counterpart, from Akiyama et al. (2015).

Column 70 Spectroscopic redshift from catalog of optical counterparts of the SXDS catalog (Akiyama et al., 2015) (-99 if no counterpart is found, 9.999 if no spectroscopic redshift is available).

Column 71 Spectroscopic classification of optical counterpart (-99 if no counterpart is found).

Column 72 Photometric redshift from catalog of optical counterparts of the SXDS catalog (Akiyama et al., 2015) (-99 if no counterpart is found).

Column 73 Photometric classification of optical counterpart (-99 if no counterpart is found).

TABLE B.2: UDS catalog, part I.

Name	Number	R.A. [deg]	DEC. [deg]	$\mathrm{DET\_ML_F}$	E_F [ks]	T_F	B_F	N_F	$\sigma_\mathrm{F}^{+,N}$	$\sigma_\mathrm{F}^{-,N}$	$\mathrm{CR_F}$ [$\mathrm{s^{-1}}$]
(1)	(2)	(3)	(4)	(5)	(6)	(7)	(8)	(9)	(10)	(11)	(12)
J340916-050237.5	1	34.1547	−5.0438	8.186	157.5	175.0	137.57	37.43	19.13	17.66	0.000238
J341921-051012.4	2	34.3226	−5.1701	5.720	223.5	216.0	187.18	28.82	21.52	20.06	0.000129

$\mathrm{Flux_F}$ [cgs]	$\sigma_\mathrm{F}^{+,\mathrm{Flux}}$ [cgs]	$\sigma_\mathrm{F}^{-,\mathrm{Flux}}$ [cgs]	$\mathrm{DET\_ML_S}$	E_S [ks]	T_S	B_S	N_S	$\sigma_\mathrm{S}^{+,N}$	$\sigma_\mathrm{S}^{-,N}$	$\mathrm{CR_S}$ [$\mathrm{s^{-1}}$]	$\mathrm{Flux_S}$ [cgs]
(13)	(14)	(15)	(16)	(17)	(18)	(19)	(20)	(21)	(22)	(23)	(24)
3.6×10^{-14}	1.8×10^{-14}	1.7×10^{-14}	12.314	169.5	98.0	61.6	36.4	14.09	12.60	0.000215	2.3×10^{-14}
2.0×10^{-14}	1.5×10^{-14}	1.4×10^{-14}	13.877	237.2	130.0	84.46	45.54	16.09	14.62	0.000192	2.0×10^{-14}

$\sigma_\mathrm{S}^{+,\mathrm{Flux}}$ [cgs]	$\sigma_\mathrm{S}^{-,\mathrm{Flux}}$ [cgs]	$\mathrm{DET\_ML_H}$	E_H [ks]	T_H	B_H	N_H	$\sigma_\mathrm{H}^{+,N}$	$\sigma_\mathrm{H}^{-,N}$	$\mathrm{CR_H}$ [$\mathrm{s^{-1}}$]	$\mathrm{Flux_H}$ [cgs]	$\sigma_\mathrm{H}^{+,\mathrm{Flux}}$ [cgs]
(25)	(26)	(27)	(28)	(29)	(30)	(31)	(32)	(33)	(34)	(35)	(36)
8.8×10^{-15}	7.9×10^{-15}	0	146.4	83.0	76.16	107.85	0	0	0.000737	1.6×10^{-13}	−99
7.2×10^{-15}	6.5×10^{-15}	0	212.8	107.0	103.18	138.18	0	0	0.000649	1.4×10^{-13}	−99

TABLE B.3: UDS catalog, part II.

$\sigma_{H}^{-,Flux}$ [cgs]	HR	HR^{-}	HR^{+}	SXDS_ID	R.A.$_{SXDS}$ [deg]	DEC.$_{SXDS}$ [deg]	$CR_{0.3-0.5}$ [ks^{-1}]	$\sigma_{0.3-0.5}^{CR}$ [ks^{-1}]	$CR_{0.5-2}$ [ks^{-1}]	$\sigma_{0.5-2}^{CR}$ [ks^{-1}]	$CR_{2-4.5}$ [ks^{-1}]	$\sigma_{2-4.5}^{CR}$ [ks^{-1}]
(37)	(38)	(39)	(40)	(41)	(42)	(43)	(44)	(45)	(46)	(47)	(48)	(49)
−99	−0.99	−1.0	−0.53	SXDS0176	34.1597	−5.0422	0.00	0.03	0.97	0.21	0.83	0.16
−99	−0.99	−1.0	−0.61	SXDS0374	34.316	−5.1707	0.00	0.06	0.00	0.11	0.41	0.14

$CR_{4.5-10}$ [ks^{-1}]	$\sigma_{4.5-10}^{CR}$ [ks^{-1}]	D_{SXDS} [″]	N_{SXDS}	xuds_ID	R.A.$_{xuds}$ [deg]	DEC.$_{xuds}$ [deg]	$Flux_{0.5-2}$ [cgs]	$\sigma_{0.5-2}^{+,Flux}$ [cgs]	$\sigma_{0.5-2}^{-,Flux}$ [cgs]	$Flux_{2-10}$ [cgs]	$\sigma_{2-10}^{+,Flux}$ [cgs]	$\sigma_{2-10}^{-,Flux}$ [cgs]
(50)	(51)	(52)	(53)	(54)	(55)	(56)	(57)	(58)	(59)	(60)	(61)	(62)
0.46	0.19	18.8	1	xuds_178	34.1604	−5.0422	4.1×10^{-15}	5.5×10^{-16}	4.9×10^{-16}	1.1×10^{-14}	1.7×10^{-15}	1.5×10^{-15}
0.26	0.18	24.3	2	xuds_098	34.3226	−5.1714	2.9×10^{-15}	2.3×10^{-16}	2.2×10^{-16}	6.5×10^{-15}	6.9×10^{-16}	6.4×10^{-16}

$Flux_{5-10}$ [cgs]	$\sigma_{5-10}^{+,Flux}$ [cgs]	$\sigma_{5-10}^{-,Flux}$ [cgs]	D_{xuds} [″]	N_{xuds}	R.A.$_{opt}$ [deg]	DEC.$_{opt}$ [deg]	z_{spec}	Spec Type	z_{phot}	Phot Type
(63)	(64)	(65)	(66)	(67)	(68)	(69)	(70)	(71)	(72)	(73)
5.7×10^{-15}	1.7×10^{-15}	1.4×10^{-15}	21.3	1	34.1604	−5.0423	1.655	NLA	1.400	GALs
2.7×10^{-15}	6.8×10^{-16}	6.0×10^{-16}	4.7	1	34.3154	−5.1704	2.989	NLA	3.040	GAL

Bibliography

Aird, J. et al. (2015). "The NuSTAR Extragalactic Survey: First Direct Measurements of the $\gtrsim$ 10 KeV X-Ray Luminosity Function for Active Galactic Nuclei at z>0.1". In: *ApJ* 815, 66, p. 66. DOI: 10.1088/0004-637X/815/1/66. arXiv: 1511.04184 [astro-ph.HE].

Ajello, M. et al. (2008). "Cosmic X-Ray Background and Earth Albedo Spectra with Swift BAT". In: *ApJ* 689, 666-677, pp. 666–677. DOI: 10.1086/592595. arXiv: 0808.3377.

Akaike, H. (1974). "A New Look at the Statistical Model Identification". In: *IEEE Transactions on Automatic Control* 19, pp. 716–723.

Akiyama, M. et al. (2015). "The Subaru-XMM-Newton Deep Survey (SXDS). VIII. Multi-wavelength identification, optical/NIR spectroscopic properties, and photometric redshifts of X-ray sources$^{\check{\mathrm{D}}}$". In: *PASJ* 67, 82, p. 82. DOI: 10.1093/pasj/psv050. arXiv: 1505.05487.

Akylas, A. et al. (2012). "Constraining the fraction of Compton-thick AGN in the Universe by modelling the diffuse X-ray background spectrum". In: *A&A* 546, A98, A98. DOI: 10.1051/0004-6361/201219387. arXiv: 1209.5398 [astro-ph.HE].

Akylas, A. et al. (2016). "Compton-thick AGN in the 70-month Swift-BAT All-Sky Hard X-ray Survey: A Bayesian approach". In: *A&A* 594, A73, A73. DOI: 10.1051/0004-6361/201628711. arXiv: 1607.08069.

Alexander, D. M. and R. C. Hickox (2012). "What drives the growth of black holes?" In: *NAR* 56, pp. 93–121. DOI: 10.1016/j.newar.2011.11.003. arXiv: 1112.1949.

Alexander, D. M. et al. (2013). "The NuSTAR Extragalactic Survey: A First Sensitive Look at the High-energy Cosmic X-Ray Background Population". In: *ApJ* 773, 125, p. 125. DOI: 10.1088/0004-637X/773/2/125. arXiv: 1307.1733 [astro-ph.HE].

Almaini, O. et al. (2007). "First Results from the UKIDSS Ultra-Deep Survey". In: *Cosmic Frontiers*. Ed. by N. Metcalfe and T. Shanks. Vol. 379. Astronomical Society of the Pacific Conference Series, p. 163.

Annuar, A. et al. (2017). "A New Compton-thick AGN in our Cosmic Backyard: Unveiling the Buried Nucleus in NGC 1448 with NuSTAR". In: *ApJ* 836, 165, p. 165. DOI: 10.3847/1538-4357/836/2/165. arXiv: 1701.00497 [astro-ph.HE].

Antonucci, R. (1993). "Unified models for active galactic nuclei and quasars". In: *Annu. Rev. Astron. Astrophys.* 31, pp. 473–521. DOI: 10.1146/annurev.aa.31.090193.002353.

Arévalo, P. et al. (2014). "The 2-79 keV X-Ray Spectrum of the Circinus Galaxy with NuSTAR, XMM-Newton, and Chandra: A Fully Compton-thick Active Galactic Nucleus". In: *ApJ* 791, 81, p. 81. DOI: 10.1088/0004-637X/791/2/81. arXiv: 1406.3345 [astro-ph.HE].

Arnaud, K. A. (1996). "XSPEC: The First Ten Years". In: *Astronomical Data Analysis Software and Systems V*. Ed. by G. H. Jacoby and J. Barnes. Vol. 101. Astronomical Society of the Pacific Conference Series, p. 17.

Asmus, D. et al. (2015). "The subarcsecond mid-infrared view of local active galactic nuclei - II. The mid-infrared-X-ray correlation". In: *MNRAS* 454, pp. 766–803. DOI: 10.1093/mnras/stv1950. arXiv: 1508.05065.

Awaki, H. et al. (2000). "X-Ray Emission from Seyfert 2 Galaxies with Optical Polarized Broad Lines". In: *ApJ* 542, pp. 175–185. DOI: 10.1086/309516. eprint: astro-ph/0006054.

Awaki, H. et al. (2009). "Detection of Hard X-Rays from the Compton-Thick Seyfert 2 Galaxy NGC 2273 with Suzaku". In: *PASJ* 61, p. 317. DOI: 10.1093/pasj/61.sp1.S317.

Ballantyne, D. R. et al. (2011). "Lifting the Veil on Obscured Accretion: Active Galactic Nuclei Number Counts and Survey Strategies for Imaging Hard X-Ray Missions". In: *ApJ* 736, 56, p. 56. DOI: 10.1088/0004-637X/736/1/56. arXiv: 1105.0965.

Baloković, M. et al. (2014). "The NuSTAR View of Nearby Compton-thick Active Galactic Nuclei: The Cases of NGC 424, NGC 1320, and IC 2560". In: *ApJ* 794, 111, p. 111. DOI: 10.1088/0004-637X/794/2/111. arXiv: 1408.5414 [astro-ph.HE].

Barvainis, R. (1987). "Hot dust and the near-infrared bump in the continuum spectra of quasars and active galactic nuclei". In: *ApJ* 320, pp. 537–544. DOI: 10.1086/165571.

Bauer, F. E. et al. (2015). "NuSTAR Spectroscopy of Multi-component X-Ray Reflection from NGC 1068". In: *ApJ* 812, 116, p. 116. DOI: 10.1088/0004-637X/812/2/116. arXiv: 1411.0670 [astro-ph.HE].

Baumgartner, W. H. et al. (2013). "The 70 Month Swift-BAT All-sky Hard X-Ray Survey". In: *ApJS* 207, 19, p. 19. DOI: 10.1088/0067-0049/207/2/19. arXiv: 1212.3336 [astro-ph.HE].

Berney, S. et al. (2015). "BAT AGN spectroscopic survey-II. X-ray emission and high-ionization optical emission lines". In: *MNRAS* 454, pp. 3622–3634. DOI: 10.1093/mnras/stv2181. arXiv: 1509.05425.

Bertin, E. and S. Arnouts (1996). "SExtractor: Software for source extraction." In: *A&AS* 117, pp. 393–404. DOI: 10.1051/aas:1996164.

Bianchi, S. and M. Guainazzi (2007). "The nature of the soft X-ray emission in obscured AGN". In: *The Multicolored Landscape of Compact Objects and Their Explosive*

Origins. Ed. by T. di Salvo et al. Vol. 924. American Institute of Physics Conference Series, pp. 822–829. DOI: 10.1063/1.2774948. eprint: astro-ph/0611045.

Bianchi, S. et al. (2005). "A search for changing-look AGN in the Grossan catalog". In: *A&A* 442, pp. 185–194. DOI: 10.1051/0004-6361:20053389. eprint: astro-ph/0507323.

Boldt, E. (1987). "The cosmic X-ray background." In: *Physics Reports* 146, pp. 215–257. DOI: 10.1016/0370-1573(87)90108-6.

Boorman, P. G. et al. (2016). "IC 3639: a New Bona Fide Compton-Thick AGN Unveiled by NuSTAR". In: *ApJ* 833, 245, p. 245. DOI: 10.3847/1538-4357/833/2/245. arXiv: 1610.08997.

Braatz, J. et al. (1997). "A VLBA Map of the H_2O Maser in the Nucleus of Seyfert 2 Galaxy NGC 1386". In: *American Astronomical Society Meeting Abstracts*. Vol. 29. Bulletin of the American Astronomical Society, p. 104.02.

Braatz, J. A., A. S. Wilson, and C. Henkel (1994). "The discovery of five new H2O megamasers in active galaxies". In: *ApJL* 437, pp. L99–L102. DOI: 10.1086/187692.

Brandt, W. N. and D. M. Alexander (2015). "Cosmic X-ray surveys of distant active galaxies. The demographics, physics, and ecology of growing supermassive black holes". In: *A&AR* 23, 1, p. 1. DOI: 10.1007/s00159-014-0081-z. arXiv: 1501.01982 [astro-ph.HE].

Brightman, M. and K. Nandra (2011). "An XMM-Newton spectral survey of 12 μm selected galaxies - I. X-ray data". In: *MNRAS* 413, pp. 1206–1235. DOI: 10.1111/j.1365-2966.2011.18207.x. arXiv: 1012.3345 [astro-ph.HE].

Brightman, M. et al. (2013). "A statistical relation between the X-ray spectral index and Eddington ratio of active galactic nuclei in deep surveys". In: *MNRAS* 433, pp. 2485–2496. DOI: 10.1093/mnras/stt920. arXiv: 1305.3917 [astro-ph.HE].

Brightman, M. et al. (2015). "Determining the Covering Factor of Compton-thick Active Galactic Nuclei with NuSTAR". In: *ApJ* 805, 41, p. 41. DOI: 10.1088/0004-637X/805/1/41. arXiv: 1502.07353 [astro-ph.HE].

Brightman, M. et al. (2016). "A Growth-rate Indicator for Compton-thick Active Galactic Nuclei". In: *ApJ* 826, 93, p. 93. DOI: 10.3847/0004-637X/826/1/93. arXiv: 1606.09265 [astro-ph.HE].

Brightman, M. et al. (2017). "X-Ray Bolometric Corrections for Compton-thick Active Galactic Nuclei". In: *ApJ* 844, 10, p. 10. DOI: 10.3847/1538-4357/aa75c9. arXiv: 1705.10804 [astro-ph.HE].

Burlon, D. et al. (2011). "Three-year Swift-BAT Survey of Active Galactic Nuclei: Reconciling Theory and Observations?" In: *ApJ* 728, 58, p. 58. DOI: 10.1088/0004-637X/728/1/58. arXiv: 1012.0302 [astro-ph.HE].

Burtscher, L. et al. (2013). "A diversity of dusty AGN tori. Data release for the VLTI/MIDI AGN Large Program and first results for 23 galaxies". In: *A&A* 558, A149, A149. DOI: 10.1051/0004-6361/201321890. arXiv: 1307.2068.

Caballero-Garcia, M. D. et al. (2012). "Hard X-ray spectral variability of the brightest Seyfert AGN in the Swift/BAT sample". In: *A&A* 537, A87, A87. DOI: 10.1051/0004-6361/201117974. arXiv: 1108.6017 [astro-ph.HE].

Casali, M. et al. (2007). "The UKIRT wide-field camera". In: *A&A* 467, pp. 777–784. DOI: 10.1051/0004-6361:20066514.

Cash, W. (1979). "Parameter estimation in astronomy through application of the likelihood ratio". In: *ApJ* 228, pp. 939–947. DOI: 10.1086/156922.

Castangia, P. et al. (2013). "New Compton-thick AGN in the circumnuclear H_2O maser hosts UGC 3789 and NGC 6264". In: *MNRAS* 436, pp. 3388–3398. DOI: 10.1093/mnras/stt1824. arXiv: 1309.6515 [astro-ph.CO].

Churazov, E. et al. (2007). "INTEGRAL observations of the cosmic X-ray background in the 5-100 keV range via occultation by the Earth". In: *A&A* 467, pp. 529–540. DOI: 10.1051/0004-6361:20066230. eprint: astro-ph/0608250.

Churchwell, E. et al. (1977). "Detection of H2O maser emission in the Galaxy M 33". In: *A&A* 54, pp. 969–971.

Civano, F. et al. (2015). "The Nustar Extragalactic Surveys: Overview and Catalog from the COSMOS Field". In: *ApJ* 808, 185, p. 185. DOI: 10.1088/0004-637X/808/2/185. arXiv: 1511.04185 [astro-ph.HE].

Comastri, A. (2004). "Compton-Thick AGN: The Dark Side of the X-Ray Background". In: *Supermassive Black Holes in the Distant Universe*. Ed. by A. J. Barger. Vol. 308. Astrophysics and Space Science Library, p. 245. DOI: 10.1007/978-1-4020-2471-9_8. eprint: astro-ph/0403693.

Comastri, A. et al. (1995). "The contribution of AGNs to the X-ray background." In: *A&A* 296, p. 1. eprint: astro-ph/9409067.

Coppin, K. et al. (2006). "The SCUBA Half-Degree Extragalactic Survey - II. Submillimetre maps, catalogue and number counts". In: *MNRAS* 372, pp. 1621–1652. DOI: 10.1111/j.1365-2966.2006.10961.x. eprint: astro-ph/0609039.

Cutri, R. M. et al. (2013). *Explanatory Supplement to the AllWISE Data Release Products*. Tech. rep.

Dawson, K. S. et al. (2013). "The Baryon Oscillation Spectroscopic Survey of SDSS-III". In: *AJ* 145, 10, p. 10. DOI: 10.1088/0004-6256/145/1/10. arXiv: 1208.0022.

Draper, A. R. and D. R. Ballantyne (2010). "The Evolution and Eddington Ratio Distribution of Compton Thick Active Galactic Nuclei". In: *ApJL* 715, pp. L99–L103. DOI: 10.1088/2041-8205/715/2/L99. arXiv: 1004.0690.

Durret, F. et al. (2011). "Galaxy cluster searches based on photometric redshifts in the four CFHTLS Wide fields". In: *A&A* 535, A65, A65. DOI: 10.1051/0004-6361/201116985. arXiv: 1109.0850.

Eddington, A. S. (1913). "On a formula for correcting statistics for the effects of a known error of observation". In: *MNRAS* 73, pp. 359–360. DOI: 10.1093/mnras/73.5.359.

Einstein, A. (1916). "Strahlungs-Emission und Absorption nach der Quantentheorie". In: *Deutsche Physikalische Gesellschaft* 18.

Elitzur, M. and I. Shlosman (2006). "The AGN-obscuring Torus: The End of the "Doughnut" Paradigm?" In: *ApJL* 648, pp. L101–L104. DOI: 10.1086/508158. eprint: astro-ph/0605686.

Fabian, A. C. (2008). "XMM-Newton and broad iron lines". In: *Astronomische Nachrichten* 329, p. 155. DOI: 10.1002/asna.200710902. arXiv: 0711.2976.

Fabian, A. C. et al. (2012). "1H 0707-495 in 2011: an X-ray source within a gravitational radius of the event horizon". In: *MNRAS* 419, pp. 116–123. DOI: 10.1111/j.1365-2966.2011.19676.x. arXiv: 1108.5988 [astro-ph.HE].

Falocco, S. et al. (2013). "The XMM Deep survey in the CDF-S. V. Iron K lines from active galactic nuclei in the distant Universe". In: *A&A* 555, A79, A79. DOI: 10.1051/0004-6361/201321083. arXiv: 1304.7690 [astro-ph.HE].

Fedorova, E. V. et al. (2011). "Studying the long-time variability of the Seyfert 2 galaxy NGC 4388 with INTEGRAL and Swift". In: *MNRAS* 417, pp. 1140–1147. DOI: 10.1111/j.1365-2966.2011.19335.x.

Ferrarese, L. and D. Merritt (2000). "A Fundamental Relation between Supermassive Black Holes and Their Host Galaxies". In: *ApJL* 539, pp. L9–L12. DOI: 10.1086/312838. eprint: astro-ph/0006053.

Fornasini, F. M. et al. (2017). "The NuSTAR Hard X-Ray Survey of the Norma Arm Region". In: *ApJS* 229, 33, p. 33. DOI: 10.3847/1538-4365/aa61fc. arXiv: 1703.00021 [astro-ph.HE].

Furusawa, H. et al. (2008). "The Subaru/XMM-Newton Deep Survey (SXDS). II. Optical Imaging and Photometric Catalogs". In: *ApJS* 176, 1-18, pp. 1–18. DOI: 10.1086/527321. arXiv: 0801.4017.

Galametz, A. et al. (2013). "CANDELS Multiwavelength Catalogs: Source Identification and Photometry in the CANDELS UKIDSS Ultra-deep Survey Field". In: *ApJS* 206, 10, p. 10. DOI: 10.1088/0067-0049/206/2/10. arXiv: 1305.1823 [astro-ph.CO].

Gandhi, P., S. F. Hönig, and M. Kishimoto (2015). "The Dust Sublimation Radius as an Outer Envelope to the Bulk of the Narrow Fe Kalpha Line Emission in Type 1 AGNs". In: *ApJ* 812, 113, p. 113. DOI: 10.1088/0004-637X/812/2/113. arXiv: 1502.02661 [astro-ph.HE].

Gandhi, P. et al. (2009). "Resolving the mid-infrared cores of local Seyferts". In: *A&A* 502, pp. 457–472. DOI: 10.1051/0004-6361/200811368. arXiv: 0902.2777.

Gandhi, P. et al. (2017). "The weak Fe fluorescence line and long-term X-ray evolution of the Compton-thick active galactic nucleus in NGC 7674". In: *MNRAS* 467, pp. 4606–4621. DOI: 10.1093/mnras/stx357. arXiv: 1605.08041 [astro-ph.HE].

Gao, F. et al. (2016). "The Megamaser Cosmology Project. VIII. A Geometric Distance to NGC 5765b". In: *ApJ* 817, 128, p. 128. DOI: 10.3847/0004-637X/817/2/128. arXiv: 1511.08311.

Gehrels, N. (1986). "Confidence limits for small numbers of events in astrophysical data". In: *ApJ* 303, pp. 336–346. DOI: 10.1086/164079.

Giacconi, R. et al. (1962). "Evidence for x Rays From Sources Outside the Solar System". In: *Physical Review Letters* 9, pp. 439–443. DOI: 10.1103/PhysRevLett.9.439.

Gilli, R., A. Comastri, and G. Hasinger (2007). "The synthesis of the cosmic X-ray background in the Chandra and XMM-Newton era". In: *A&A* 463, pp. 79–96. DOI: 10.1051/0004-6361:20066334. eprint: astro-ph/0610939.

Gilli, R. et al. (2000). "The variability of the Seyfert galaxy NGC 2992: the case for a revived AGN". In: *A&A* 355, pp. 485–498. eprint: astro-ph/0001107.

Gilli, R. et al. (2011). "A Compton-thick Active Galactic Nucleus at z ~ 5 in the 4 Ms Chandra Deep Field South". In: *ApJL* 730, L28, p. L28. DOI: 10.1088/2041-8205/730/2/L28. arXiv: 1102.4714.

Greene, J. E. et al. (2016). "Megamaser Disks Reveal a Broad Distribution of Black Hole Mass in Spiral Galaxies". In: *ApJL* 826, L32, p. L32. DOI: 10.3847/2041-8205/826/2/L32. arXiv: 1606.00018.

Greenhill, L. J., J. M. Moran, and J. R. Herrnstein (1997). "The Distribution of H_2O Maser Emission in the Nucleus of NGC 4945". In: *ApJL* 481, pp. L23–L26. DOI: 10.1086/310643. eprint: astro-ph/9702220.

Greenhill, L. J., A. Tilak, and G. Madejski (2008). "Prevalence of High X-Ray Obscuring Columns among AGNs that Host H_2O Masers". In: *ApJL* 686, pp. L13–L16. DOI: 10.1086/592782. arXiv: 0809.1108.

Greenhill, L. J. et al. (2003). "A Warped Accretion Disk and Wide-Angle Outflow in the Inner Parsec of the Circinus Galaxy". In: *ApJ* 590, pp. 162–173. DOI: 10.1086/374862. eprint: astro-ph/0302533.

Gruppioni, C. et al. (2016). "Tracing black hole accretion with SED decomposition and IR lines: from local galaxies to the high-z Universe". In: *MNRAS* 458, pp. 4297–4320. DOI: 10.1093/mnras/stw577. arXiv: 1603.02818.

Guainazzi, M. (2002). "The formerly X-ray reflection-dominated Seyfert 2 galaxy NGC 6300". In: *MNRAS* 329, pp. L13–L17. DOI: 10.1046/j.1365-8711.2002.05132.x. eprint: astro-ph/0111148.

Guainazzi, M. et al. (2002). "The Phoenix galaxy: UGC 4203 re-birth from its ashes?" In: *A&A* 388, pp. 787–792. DOI: 10.1051/0004-6361:20020471. eprint: astro-ph/0204052.

Guainazzi, M. et al. (2005). "On the transmission-dominated to reprocessing-dominated spectral state transitions in Seyfert 2 galaxies". In: *MNRAS* 356, pp. 295–308. DOI: 10.1111/j.1365-2966.2004.08448.x. eprint: astro-ph/0409689.

Harrison, C. (2014). "Observational constraints on the influence of active galactic nuclei on the evolution of galaxies". PhD thesis. Durham University.

Harrison, F. A. et al. (2013). "The Nuclear Spectroscopic Telescope Array (NuSTAR) High-energy X-Ray Mission". In: *ApJ* 770, 103, p. 103. DOI: 10.1088/0004-637X/770/2/103. arXiv: 1301.7307 [astro-ph.IM].

Harrison, F. A. et al. (2016). "The NuSTAR Extragalactic Surveys: The Number Counts of Active Galactic Nuclei and the Resolved Fraction of the Cosmic X-Ray Background". In: *ApJ* 831, 185, p. 185. DOI: 10.3847/0004-637X/831/2/185. arXiv: 1511.04183 [astro-ph.HE].

Henkel, C. et al. (2012). "Cosmology and the Hubble Constant: On the Megamaser Cosmology Project (MCP)". In: *IAU Symposium*. Ed. by R. S. Booth, W. H. T. Vlemmings, and E. M. L. Humphreys. Vol. 287. IAU Symposium, pp. 301–310. DOI: 10.1017/S1743921312007223. arXiv: 1205.0823 [astro-ph.CO].

Herrnstein, J. R. et al. (2005). "The Geometry of and Mass Accretion Rate through the Maser Accretion Disk in NGC 4258". In: *ApJ* 629, pp. 719–738. DOI: 10.1086/431421. eprint: astro-ph/0504405.

Hickox, R. C. and M. Markevitch (2006). "Absolute Measurement of the Unresolved Cosmic X-Ray Background in the 0.5-8 keV Band with Chandra". In: *ApJ* 645, pp. 95–114. DOI: 10.1086/504070. eprint: astro-ph/0512542.

Hickox, R. C. et al. (2014). "Black Hole Variability and the Star Formation-Active Galactic Nucleus Connection: Do All Star-forming Galaxies Host an Active Galactic Nucleus?" In: *ApJ* 782, 9, p. 9. DOI: 10.1088/0004-637X/782/1/9. arXiv: 1306.3218.

Hopkins, P. F. et al. (2006). "A Unified, Merger-driven Model of the Origin of Starbursts, Quasars, the Cosmic X-Ray Background, Supermassive Black Holes, and Galaxy Spheroids". In: *ApJS* 163, pp. 1–49. DOI: 10.1086/499298. eprint: astro-ph/0506398.

Jansen, F. et al. (2001). "XMM-Newton observatory. I. The spacecraft and operations". In: *A&A* 365, pp. L1–L6. DOI: 10.1051/0004-6361:20000036.

Jarvis, M. J. et al. (2013). "The VISTA Deep Extragalactic Observations (VIDEO) survey". In: *MNRAS* 428, pp. 1281–1295. DOI: 10.1093/mnras/sts118. arXiv: 1206.4263.

Kalberla, P. M. W. et al. (2005). "The Leiden/Argentine/Bonn (LAB) Survey of Galactic HI. Final data release of the combined LDS and IAR surveys with improved stray-radiation corrections". In: *A&A* 440, pp. 775–782. DOI: 10.1051/0004-6361:20041864. eprint: astro-ph/0504140.

Kishimoto, M. et al. (2007). "The innermost region of AGN tori: implications from the HST/NICMOS type 1 point sources and near-IR reverberation". In: *A&A* 476, pp. 713–721. DOI: 10.1051/0004-6361:20077911. arXiv: 0709.0431.

Kondratko, P. T., L. J. Greenhill, and J. M. Moran (2005). "Evidence for a Geometrically Thick Self-Gravitating Accretion Disk in NGC 3079". In: *ApJ* 618, pp. 618–634. DOI: 10.1086/426101. eprint: astro-ph/0408549.

— (2008). "The Parsec-Scale Accretion Disk in NGC 3393". In: *ApJ* 678, pp. 87–95. DOI: 10.1086/586879. arXiv: 0801.4755.

Koss, M. et al. (2017). "BAT AGN Spectroscopic Survey I: Spectral Measurements, Derived Quantities, and AGN Demographics". In: *ArXiv e-prints*. arXiv: 1707.08123 [astro-ph.HE].

Koss, M. J. et al. (2015). "Broadband Observations of the Compton-thick Nucleus of NGC 3393". In: *ApJ* 807, 149, p. 149. DOI: 10.1088/0004-637X/807/2/149. arXiv: 1505.03524.

Koss, M. J. et al. (2016). "A New Population of Compton-thick AGNs Identified Using the Spectral Curvature above 10 keV". In: *ApJ* 825, 85, p. 85. DOI: 10.3847/0004-637X/825/2/85. arXiv: 1604.07825 [astro-ph.HE].

Krivonos, R. et al. (2007). "INTEGRAL/IBIS all-sky survey in hard X-rays". In: *A&A* 475, pp. 775–784. DOI: 10.1051/0004-6361:20077191. eprint: astro-ph/0701836.

Kuo, C. Y. et al. (2011). "The Megamaser Cosmology Project. III. Accurate Masses of Seven Supermassive Black Holes in Active Galaxies with Circumnuclear Megamaser Disks". In: *ApJ* 727, 20, p. 20. DOI: 10.1088/0004-637X/727/1/20. arXiv: 1008.2146 [astro-ph.CO].

La Franca, F. et al. (2005). "The HELLAS2XMM Survey. VII. The Hard X-Ray Luminosity Function of AGNs up to z = 4: More Absorbed AGNs at Low Luminosities and High Redshifts". In: *ApJ* 635, pp. 864–879. DOI: 10.1086/497586. eprint: astro-ph/0509081.

LaMassa, S. M. et al. (2014). "Delving Into X-ray Obscuration of Type 2 AGN, Near and Far". In: *ApJ* 787, 61, p. 61. DOI: 10.1088/0004-637X/787/1/61. arXiv: 1404.0012 [astro-ph.HE].

Lansbury, G. B. et al. (2014). "NuSTAR Observations of Heavily Obscured Quasars at z ~ 0.5". In: *ApJ* 785, 17, p. 17. DOI: 10.1088/0004-637X/785/1/17. arXiv: 1402.2666 [astro-ph.HE].

Lansbury, G. B. et al. (2015). "NuSTAR Reveals Extreme Absorption in z < 0.5 Type 2 Quasars". In: *ApJ* 809, 115, p. 115. DOI: 10.1088/0004-637X/809/2/115. arXiv: 1506.05120 [astro-ph.HE].

Lansbury, G. B. et al. (2017a). "The NuSTAR Serendipitous Survey: Hunting for The Most Extreme Obscured AGN at > 10 keV". In: *ArXiv e-prints*. arXiv: 1707.06651 [astro-ph.HE].

Lansbury, G. B. et al. (2017b). "The NuSTAR Serendipitous Survey: The 40-month Catalog and the Properties of the Distant High-energy X-Ray Source Population". In: *ApJ* 836, 99, p. 99. DOI: 10.3847/1538-4357/836/1/99. arXiv: 1612.06389 [astro-ph.HE].

Lanzuisi, G. et al. (2015). "Compton thick AGN in the XMM-COSMOS survey". In: *A&A* 573, A137, A137. DOI: 10.1051/0004-6361/201424924. arXiv: 1409.1867.

Lawrence, A. et al. (2007). "The UKIRT Infrared Deep Sky Survey (UKIDSS)". In: *MNRAS* 379, pp. 1599–1617. DOI: 10.1111/j.1365-2966.2007.12040.x. eprint: astro-ph/0604426.

Litvak, M. M. (1969). "Hydroxyl and Water Masers in Protostars". In: *Science* 165, pp. 855–861. DOI: 10.1126/science.165.3896.855.

Liu, Y. and X. Li (2015). "A direct comparison of X-ray spectral models for tori in active galactic nuclei". In: *MNRAS* 448, pp. L53–L57. DOI: 10.1093/mnrasl/slu198. arXiv: 1501.00557 [astro-ph.HE].

Lo, K. Y. (2005). "Mega-Masers and Galaxies". In: *Annu. Rev. Astron. Astrophys.* 43, pp. 625–676. DOI: 10.1146/annurev.astro.41.011802.094927.

Lodato, G. and G. Bertin (2003). "Non-Keplerian rotation in the nucleus of <ASTROBJ>NGC 1068</ASTROBJ>: Evidence for a massive accretion disk?" In: *A&A* 398, pp. 517–524. DOI: 10.1051/0004-6361:20021672. eprint: astro-ph/0211113.

Lonsdale, C. J. et al. (2003). "SWIRE: The SIRTF Wide-Area Infrared Extragalactic Survey". In: *PASP* 115, pp. 897–927. DOI: 10.1086/376850. eprint: astro-ph/0305375.

López-Gonzaga, N. et al. (2014). "Revealing the large nuclear dust structures in NGC 1068 with MIDI/VLTI". In: *A&A* 565, A71, A71. DOI: 10.1051/0004-6361/201323002. arXiv: 1401.3248.

Lusso, E. et al. (2012). "Bolometric luminosities and Eddington ratios of X-ray selected active galactic nuclei in the XMM-COSMOS survey". In: *MNRAS* 425, pp. 623–640. DOI: 10.1111/j.1365-2966.2012.21513.x. arXiv: 1206.2642 [astro-ph.CO].

Madejski, G. et al. (2000). "Structure of the Circumnuclear Region of Seyfert 2 Galaxies Revealed by Rossi X-Ray Timing Explorer Hard X-Ray Observations of NGC 4945". In: *ApJL* 535, pp. L87–L90. DOI: 10.1086/312703. eprint: astro-ph/0002063.

Magdziarz, P. and A. A. Zdziarski (1995). "Angle-dependent Compton reflection of X-rays and gamma-rays". In: *MNRAS* 273, pp. 837–848.

Magorrian, J. et al. (1998). "The Demography of Massive Dark Objects in Galaxy Centers". In: *AJ* 115, pp. 2285–2305. DOI: 10.1086/300353. eprint: astro-ph/9708072.

Maiolino, R. et al. (1998). "Heavy obscuration in X-ray weak AGNs". In: *A&A* 338, pp. 781–794. eprint: astro-ph/9806055.

Malaguti, G. et al. (1998). "BeppoSAX observation of NGC 7674: a new reflection-dominated Seyfert 2 galaxy". In: *A&A* 331, pp. 519–523. eprint: astro-ph/9711145.

Marchesi, S. et al. (2016). "The Chandra COSMOS-Legacy Survey: The z > 3 Sample". In: *ApJ* 827, 150, p. 150. DOI: 10.3847/0004-637X/827/2/150. arXiv: 1606.06813.

Marinucci, A. et al. (2016). "NuSTAR catches the unveiling nucleus of NGC 1068". In: *MNRAS* 456, pp. L94–L98. DOI: 10.1093/mnrasl/slv178. arXiv: 1511.03503 [astro-ph.HE].

Markowitz, A. G., M. Krumpe, and R. Nikutta (2014). "First X-ray-based statistical tests for clumpy-torus models: eclipse events from 230 years of monitoring of Seyfert AGN". In: *MNRAS* 439, pp. 1403–1458. DOI: 10.1093/mnras/stt2492. arXiv: 1402.2779 [astro-ph.GA].

Masini, A. et al. (2016). "NuSTAR observations of water megamaser AGN". In: *A&A* 589, A59, A59. DOI: 10.1051/0004-6361/201527689. arXiv: 1602.03185 [astro-ph.HE].

Matt, G. et al. (2009). "Suzaku observation of the Phoenix galaxy". In: *A&A* 496, pp. 653–658. DOI: 10.1051/0004-6361/200811049. arXiv: 0902.0930 [astro-ph.HE].

Mazzalay, X. and A. Rodríguez-Ardila (2007). "Optical and NIR spectroscopy of Mrk 1210: constraints and physical conditions of the active nucleus". In: *A&A* 463, pp. 445–454. DOI: 10.1051/0004-6361:20054194. eprint: astro-ph/0608534.

McConnell, N. J. and C.-P. Ma (2013). "Revisiting the Scaling Relations of Black Hole Masses and Host Galaxy Properties". In: *ApJ* 764, 184, p. 184. DOI: 10.1088/0004-637X/764/2/184. arXiv: 1211.2816 [astro-ph.CO].

Mori, K. et al. (2015). "NuSTAR Hard X-Ray Survey of the Galactic Center Region I: Hard X-Ray Morphology and Spectroscopy of the Diffuse Emission". In: *ApJ* 814, 94, p. 94. DOI: 10.1088/0004-637X/814/2/94. arXiv: 1510.04631 [astro-ph.HE].

Mullaney, J. R. et al. (2015). "The NuSTAR Extragalactic Surveys: Initial Results and Catalog from the Extended Chandra Deep Field South". In: *ApJ* 808, 184, p. 184. DOI: 10.1088/0004-637X/808/2/184. arXiv: 1511.04186 [astro-ph.HE].

Murphy, K. D. and T. Yaqoob (2009). "An X-ray spectral model for Compton-thick toroidal reprocessors". In: *MNRAS* 397, pp. 1549–1562. DOI: 10.1111/j.1365-2966.2009.15025.x. arXiv: 0905.3188 [astro-ph.HE].

Murray, S. S. et al. (2005). "XBootes: An X-Ray Survey of the NDWFS Bootes Field. I. Overview and Initial Results". In: *ApJS* 161, pp. 1–8. DOI: 10.1086/444378. eprint: astro-ph/0504084.

Nenkova, M. et al. (2008a). "AGN Dusty Tori. I. Handling of Clumpy Media". In: *ApJ* 685, pp. 147–159. DOI: 10.1086/590482. arXiv: 0806.0511.

Nenkova, M. et al. (2008b). "AGN Dusty Tori. II. Observational Implications of Clumpiness". In: *ApJ* 685, pp. 160–180. DOI: 10.1086/590483. arXiv: 0806.0512.

Netzer, H. (2013). *The Physics and Evolution of Active Galactic Nuclei*.

— (2015). "Revisiting the Unified Model of Active Galactic Nuclei". In: *Annu. Rev. Astron. Astrophys.* 53, pp. 365–408. DOI: 10.1146/annurev-astro-082214-122302. arXiv: 1505.00811.

Neufeld, D. A., P. R. Maloney, and S. Conger (1994). "Water maser emission from X-ray-heated circumnuclear gas in active galaxies". In: *ApJL* 436, p. L127. DOI: 10.1086/187649.

Ohno, M., Y. Fukazawa, and N. Iyomoto (2004). "Reflection Component in the Hard X-Ray Emission from the Seyfert 2 Galaxy Mrk 1210". In: *PASJ* 56, pp. 425–429. DOI: 10.1093/pasj/56.3.425. eprint: astro-ph/0405172.

Oliver, S. J. et al. (2012). "The Herschel Multi-tiered Extragalactic Survey: HerMES". In: *MNRAS* 424, pp. 1614–1635. DOI: 10.1111/j.1365-2966.2012.20912.x. arXiv: 1203.2562.

Padovani, P. (2017). "On the two main classes of active galactic nuclei". In: *Nature Astronomy* 1, 0194, p. 0194. DOI: 10.1038/s41550-017-0194. arXiv: 1707.08069.

Park, T. et al. (2006). "Bayesian Estimation of Hardness Ratios: Modeling and Computations". In: *ApJ* 652, pp. 610–628. DOI: 10.1086/507406. eprint: astro-ph/0606247.

Penzias, A. A. and R. W. Wilson (1965). "A Measurement of Excess Antenna Temperature at 4080 Mc/s." In: *ApJ* 142, pp. 419–421. DOI: 10.1086/148307.

Perkins, F., T. Gold, and E. E. Salpeter (1966). "Maser Action in Interstellar OH". In: *ApJ* 145, p. 361. DOI: 10.1086/148775.

Pesce, D. W. et al. (2015). "The Megamaser Cosmology Project. VII. Investigating Disk Physics Using Spectral Monitoring Observations". In: *ApJ* 810, 65, p. 65. DOI: 10.1088/0004-637X/810/1/65. arXiv: 1507.07904.

Piconcelli, E. et al. (2007). "XMM-Newton broad-band observations of NGC 7582: N{H} variations and fading out of the active nucleus". In: *A&A* 466, pp. 855–863. DOI: 10.1051/0004-6361:20066439. eprint: astro-ph/0702564.

Polletta, M. d. C. et al. (2006). "Chandra and Spitzer Unveil Heavily Obscured Quasars in the Chandra/SWIRE Survey". In: *ApJ* 642, pp. 673–693. DOI: 10.1086/500821. eprint: astro-ph/0602228.

Puccetti, S. et al. (2014). "The Variable Hard X-Ray Emission of NGC 4945 as Observed by NuSTAR". In: *ApJ* 793, 26, p. 26. DOI: 10.1088/0004-637X/793/1/26. arXiv: 1407.3974 [astro-ph.HE].

Raban, D. et al. (2009). "Resolving the obscuring torus in NGC 1068 with the power of infrared interferometry: revealing the inner funnel of dust". In: *MNRAS* 394, pp. 1325–1337. DOI: 10.1111/j.1365-2966.2009.14439.x. arXiv: 0901.1306 [astro-ph.GA].

Reid, M. J. et al. (2013). "The Megamaser Cosmology Project. IV. A Direct Measurement of the Hubble Constant from UGC 3789". In: *ApJ* 767, 154, p. 154. DOI: 10.1088/0004-637X/767/2/154. arXiv: 1207.7292.

Ricci, C. et al. (2015). "Compton-thick Accretion in the Local Universe". In: *ApJL* 815, L13, p. L13. DOI: 10.1088/2041-8205/815/1/L13. arXiv: 1603.04852 [astro-ph.HE].

Ricci, C. et al. (2017). "Growing supermassive black holes in the late stages of galaxy mergers are heavily obscured". In: *MNRAS* 468, pp. 1273–1299. DOI: 10.1093/mnras/stx173. arXiv: 1701.04825 [astro-ph.HE].

Risaliti, G., R. Maiolino, and M. Salvati (1999). "The Distribution of Absorbing Column Densities among Seyfert 2 Galaxies". In: *ApJ* 522, pp. 157–164. DOI: 10.1086/307623. eprint: astro-ph/9902377.

Risaliti, G. et al. (1999). "X-ray observations of Seyfert 2 galaxies: N_H distribution and the X ray background." In: *Mem. della Soc. Astron. Ita.* 70, pp. 73–76.

Risaliti, G. et al. (2005). "Rapid Compton-thick/Compton-thin Transitions in the Seyfert 2 Galaxy NGC 1365". In: *ApJL* 623, pp. L93–L96. DOI: 10.1086/430252.

Risaliti, G. et al. (2010). "Chandra monitoring of UGC 4203: the structure of the X-ray absorber". In: *MNRAS* 406, pp. L20–L24. DOI: 10.1111/j.1745-3933.2010.00873.x. arXiv: 1005.3052.

Rivers, E. et al. (2015a). "The Multi-layer Variable Absorbers in NGC 1365 Revealed by XMM-Newton and NuSTAR". In: *ApJ* 804, 107, p. 107. DOI: 10.1088/0004-637X/804/2/107. arXiv: 1503.03109 [astro-ph.HE].

Rivers, E. et al. (2015b). "The NuSTAR View of Reflection and Absorption in NGC 7582". In: *ApJ* 815, 55, p. 55. DOI: 10.1088/0004-637X/815/1/55. arXiv: 1511.01951 [astro-ph.HE].

Rosen, S. R. et al. (2016). "The XMM-Newton serendipitous survey. VII. The third XMM-Newton serendipitous source catalogue". In: *A&A* 590, A1, A1. DOI: 10.1051/0004-6361/201526416. arXiv: 1504.07051 [astro-ph.HE].

Sanders, D. B. et al. (1988). "Warm ultraluminous galaxies in the IRAS survey - The transition from galaxy to quasar?" In: *ApJL* 328, pp. L35–L39. DOI: 10.1086/185155.

Schmidt, M. (1963). "3C 273 : A Star-Like Object with Large Red-Shift". In: *Nature* 197, p. 1040. DOI: 10.1038/1971040a0.

Simpson, C. et al. (2006). "Radio imaging of the Subaru/XMM-Newton Deep Field - I. The 100-μJy catalogue, optical identifications, and the nature of the faint radio source population". In: *MNRAS* 372, pp. 741–757. DOI: 10.1111/j.1365-2966.2006.10907.x. eprint: astro-ph/0609529.

Steffen, A. T. et al. (2006). "The X-Ray-to-Optical Properties of Optically Selected Active Galaxies over Wide Luminosity and Redshift Ranges". In: *AJ* 131, pp. 2826–2842. DOI: 10.1086/503627. eprint: astro-ph/0602407.

Stern, D. et al. (2012). "Mid-infrared Selection of Active Galactic Nuclei with the Wide-Field Infrared Survey Explorer. I. Characterizing WISE-selected Active Galactic Nuclei in COSMOS". In: *ApJ* 753, 30, p. 30. DOI: 10.1088/0004-637X/753/1/30. arXiv: 1205.0811.

Storchi-Bergmann, T., R. C. Fernandes, and H. R. Schmitt (1998). "The Nature of the Optical Light in Seyfert 2 Galaxies with Polarized Continua". In: *ApJ* 501, pp. 94–102. DOI: 10.1086/305803. eprint: astro-ph/9801310.

Tarchi, A. (2012). "AGN and Megamasers". In: *Cosmic Masers - from OH to H0*. Ed. by R. S. Booth, W. H. T. Vlemmings, and E. M. L. Humphreys. Vol. 287. IAU Symposium, pp. 323–332. DOI: 10.1017/S1743921312007259. arXiv: 1205.3623.

Tilak, A. et al. (2008). "A Deep 0.3-10 keV Spectrum of the H_2O Maser Galaxy IC 2560". In: *ApJ* 678, pp. 701–711. DOI: 10.1086/529537. arXiv: 0801.2382.

Tomsick, J. A. et al. (2017). "Galactic Sources Detected in the NuSTAR Serendipitous Survey". In: *ApJS* 230, 25, p. 25. DOI: 10.3847/1538-4365/aa7517. arXiv: 1705.08476 [astro-ph.HE].

Trakhtenbrot, B. et al. (2017). "BAT AGN Spectroscopic Survey (BASS) - VI. The Γ_X-L/L_{Edd} relation". In: *MNRAS* 470, pp. 800–814. DOI: 10.1093/mnras/stx1117. arXiv: 1705.01550.

Treister, E., C. M. Urry, and S. Virani (2009). "The Space Density of Compton-Thick Active Galactic Nucleus and the X-Ray Background". In: *ApJ* 696, pp. 110–120. DOI: 10.1088/0004-637X/696/1/110. arXiv: 0902.0608.

Tristram, K. R. W. et al. (2007). "Resolving the complex structure of the dust torus in the active nucleus of the Circinus galaxy". In: *A&A* 474, pp. 837–850. DOI: 10.1051/0004-6361:20078369. arXiv: 0709.0209.

Tristram, K. R. W. et al. (2014). "The dusty torus in the Circinus galaxy: a dense disk and the torus funnel". In: *A&A* 563, A82, A82. DOI: 10.1051/0004-6361/201322698. arXiv: 1312.4534 [astro-ph.GA].

Tueller, J. et al. (2008). "Swift BAT Survey of AGNs". In: *ApJ* 681, 113-127, pp. 113–127. DOI: 10.1086/588458. arXiv: 0711.4130.

Ueda, Y. et al. (2003). "Cosmological Evolution of the Hard X-Ray Active Galactic Nucleus Luminosity Function and the Origin of the Hard X-Ray Background". In: *ApJ* 598, pp. 886–908. DOI: 10.1086/378940. eprint: astro-ph/0308140.

Ueda, Y. et al. (2008). "The Subaru/XMM-Newton Deep Survey (SXDS). III. X-Ray Data". In: *ApJS* 179, 124-141, pp. 124–141. DOI: 10.1086/591083. arXiv: 0806.2846.

Urry, C. M. and P. Padovani (1995). "Unified Schemes for Radio-Loud Active Galactic Nuclei". In: *PASP* 107, p. 803. DOI: 10.1086/133630. eprint: astro-ph/9506063.

van den Bosch, R. C. E. et al. (2016). "Toward Precision Supermassive Black Hole Masses Using Megamaser Disks". In: *ApJ* 819, 11, p. 11. DOI: 10.3847/0004-637X/819/1/11. arXiv: 1601.00645.

Vasudevan, R. V., R. F. Mushotzky, and P. Gandhi (2013). "Can We Reproduce the X-Ray Background Spectral Shape Using Local Active Galactic Nuclei?" In: *ApJL* 770, L37, p. L37. DOI: 10.1088/2041-8205/770/2/L37. arXiv: 1305.6611 [astro-ph.HE].

Vasudevan, R. V. et al. (2016). "A selection effect boosting the contribution from rapidly spinning black holes to the cosmic X-ray background". In: *MNRAS* 458, pp. 2012–2023. DOI: 10.1093/mnras/stw363. arXiv: 1506.01027 [astro-ph.HE].

Vasylenko, A. A. et al. (2015). "Evidence for a binary black hole in active nucleus of NGC 1194 galaxy?" In: *Kinematics and Physics of Celestial Bodies* 31, pp. 13–18. DOI: 10.3103/S0884591315010079.

Vito, F. et al. (2014). "The hard X-ray luminosity function of high-redshift (3 < z < 5) active galactic nuclei". In: *MNRAS* 445, pp. 3557–3574. DOI: 10.1093/mnras/stu2004. arXiv: 1409.6918.

Wada, K. (2012). "Radiation-driven Fountain and Origin of Torus around Active Galactic Nuclei". In: *ApJ* 758, 66, p. 66. DOI: 10.1088/0004-637X/758/1/66. arXiv: 1208.5272.

Walton, D. J. et al. (2014). "NuSTAR and XMM-NEWTON Observations of NGC 1365: Extreme Absorption Variability and a Constant Inner Accretion Disk". In: *ApJ* 788, 76, p. 76. DOI: 10.1088/0004-637X/788/1/76.

Wang, Q. D. (2004). "Correction for the Flux Measurement Bias in X-Ray Source Detection". In: *ApJ* 612, pp. 159–167. DOI: 10.1086/422553. eprint: astro-ph/0405272.

Weisskopf, M. C. et al. (2000). "Chandra X-ray Observatory (CXO): overview". In: *X-Ray Optics, Instruments, and Missions III*. Ed. by J. E. Truemper and B. Aschenbach. Vol. 4012. Proceedings of SPIE, pp. 2–16. DOI: 10.1117/12.391545. eprint: astro-ph/0004127.

Wik, D. R. et al. (2014). "NuSTAR Observations of the Bullet Cluster: Constraints on Inverse Compton Emission". In: *ApJ* 792, 48, p. 48. DOI: 10.1088/0004-637X/792/1/48. arXiv: 1403.2722 [astro-ph.HE].

Worsley, M. A. et al. (2005). "The unresolved hard X-ray background: the missing source population implied by the Chandra and XMM-Newton deep fields". In: *MNRAS* 357, pp. 1281–1287. DOI: 10.1111/j.1365-2966.2005.08731.x. eprint: astro-ph/0412266.

Wright, E. L. et al. (2010). "The Wide-field Infrared Survey Explorer (WISE): Mission Description and Initial On-orbit Performance". In: *AJ* 140, 1868-1881, pp. 1868–1881. DOI: 10.1088/0004-6256/140/6/1868. arXiv: 1008.0031 [astro-ph.IM].

Wu, Q., H. Yan, and Z. Yi (2013). "Warping of an accretion disc and launching of a jet by a spinning black hole in NGC 4258". In: *MNRAS* 436, pp. 1278–1285. DOI: 10.1093/mnras/stt1655. arXiv: 1305.0072 [astro-ph.HE].

Xue, Y. Q. (2017). "The Chandra Deep Fields: Lifting the Veil on Distant Active Galactic Nuclei and X-Ray Emitting Galaxies". In: *ArXiv e-prints*. arXiv: 1709.04601.

Xue, Y. Q. et al. (2011). "The Chandra Deep Field-South Survey: 4 Ms Source Catalogs". In: *ApJS* 195, 10, p. 10. DOI: 10.1088/0067-0049/195/1/10. arXiv: 1105.5643.

Yamauchi, A. et al. (2012). "Water-Vapor Maser Disk at the Nucleus of the Seyfert 2 Galaxy IC 2560 and its Distance". In: *PASJ* 64, p. 103. DOI: 10.1093/pasj/64.5.103. arXiv: 1207.6820 [astro-ph.GA].

Yaqoob, T. (1997). "X-Ray Transmission in Cold Matter: Nonrelativistic Corrections for Compton Scattering". In: *ApJ* 479, pp. 184–189.

— (2012). "The nature of the Compton-thick X-ray reprocessor in NGC 4945". In: *MNRAS* 423, pp. 3360–3396. DOI: 10.1111/j.1365-2966.2012.21129.x. arXiv: 1204.4196 [astro-ph.HE].

Zhu, G. et al. (2011). "Optical Properties of Host Galaxies of Extragalactic Nuclear Water Masers". In: *ApJ* 742, 73, p. 73. DOI: 10.1088/0004-637X/742/2/73. arXiv: 1108.3348.

Acknowledgements

Three years oh PhD flew away, and (as usual) I realize how much time has passed, and how many experiences I lived, when everything is over - or, better saying, when a cycle ends and another one begins.
Bologna, with its vitality, and its Astronomical Observatory and Department of Physics and Astronomy, two scientifically stimulating environments, allowed me to incredibly grow as a man, as a student, and as a (hopefully future) scientist. I met people who tirelessly helped me, and their names list would be almost endless.
First of all, I would like to thank my PhD supervisor, Andrea Comastri, who trusted me since the first day we met, and guided me through an exciting topic such as observational high energy astrophysics, completely new to me. Despite being often busy with many other activities and duties, he always found the right moments for me, showing great expertise, humanness, dedication and passion.
I owe so much of what I learned in these three years of PhD to the five months abroad I spent in Boston during 2016, at the Harvard-Smithsonian Center for Astrophysics. In such a competitive environment, where you can daily touch with your hand high-quality science, I had the luck to be be assisted and supervised by a person who taught a lot to me, Francesca Civano. The Boston experience has been one of the most prolific of my life so far, and thanks to the experience gained between those months and the years in Bologna, I will soon start an early career in astrophysical research in the USA. Being part of the NuSTAR collaboration, I had the privilege to meet and collaborate with some of the brightest scientists of modern high-energy astrophysics, such as Fiona Harrison, Daniel Stern, Poshak Gandhi, Niel Brandt, and many others.
A solid career path needs some solid leading figures. I also had the luck to meet many of them, like Marcella Brusa, Nico Cappelluti, Roberto Gilli, Giorgio Lanzuisi, Simonetta Puccetti, Cristian Vignali; people always ready to give advices, explain technicalities, read drafts. Also my colleagues taught me many things, in particular those I had the pleasure and privilege to share the office with: Enrico Di Teodoro, Gabriele Pezzulli, Lorenzo Posti. They showed me the importance of human relations beyond the working relationships, together with the importance and beauty of enriching the free time with good company. Obviously, to be added to this names are my present officemates, Riccardo and Vittorio, and all my colleagues, always ready to gift you a smile also in the worst days.
Last but not least, I would like to thank the Italian National Institute of Astrophysics (INAF), the NuSTAR collaboration, the Smithsonian Astrophysical Observatory (SAO), and the University of Bologna for financial support during my PhD.